UNIVERSIDADE DE SÃO PAULO

INSTITUTO DE ASTRONOMIA GEOFÍSICA E CIÊNCIAS ATMOSFÉRICAS

DEPARTAMENTO DE GEOFÍSICA

Magnetism of Cambrian plutons of the Araçuaí belt, orogenic collapse and paleogeography of West Gondwana

Filipe Altoé Temporim

Advisor: Prof. Dr. Ricardo Ivan Ferreira Da Trindade

São Paulo

2021

Filipe Altoé Temporim

Magnetism of Cambrian plutons of the Araçuaí belt, orogenic collapse and paleogeography of West Gondwana

Doctoral thesis presented to the Instituto de Astronomia Geofísica e Ciências Atmosféricas da Universidade of São Paulo (IAG-USP), to obtain the title of Doctor of Geophysics.

Advisor: Prof. Dr. Ricardo I. F. Da Trindade

Versão Corrigida. O original encontra-se disponível na Unidade.

São Paulo

2021

Dedicated to my parents,
Renildes and Edemilson.

Acknowledgements

For the sake of convenience, both English and Portuguese were used here.

First and foremost, I would like to thank my parents, **Renildes** and **Edemilson**, for always encouraging me to study and move forward even in times of discouragement. To my brother **Vinicius** and my sister **Marcelle**, for always being present. Also, thanks to my girlfriend **Késia**, for all her understanding and affection during all moments.

I would like to acknowledgement my advisor **Ricardo Trindade** for guiding me through this project. I am very grateful for all his support and for being an excellent mentor. Also, thanks to my informal supervisor **Eric Tohver**, I am very grateful for supporting and facilitating research.

Thanks to all great friends at USPmag who were great partners and made these four years pass as smoothly as possible. In particular, **Janine**, **Plínio**, **Jhon**, **Karine**, **Wilbor**, **Graziane**, **Danielle**, **Giovanne**, **Kamilla**, **Gelson**, **Ualisson**, **Thiago**, **Caio**, **Lívia**, **Raphael** and all the others.

Thanks to my supervisor at CEED, **Mathew Domeier**, for your guidance and providing me an excellent working and social environment. Also, thanks to all friends at CEED, who made this experience go far beyond the academy, especially **Lea**, **Bjorn**, **Pratick** and **Florence**.

Also, I would like to acknowledgement my friends from other institutes who collaborated with this work and who were particularly important in the field campaigns, **Caroline**, **Lucas** and **Tiago**.

To the Foundation for Research Support of the State of São Paulo (FAPESP) for financial support in the form of a PhD's Scholarship under process n° 2017/11672-0 and 2019/18892-1 (the opinions, hypotheses and conclusions or recommendations expressed in this material are the authors' responsibility and do not necessarily reflect FAPESP's vision).

Agradecimentos

Primeiramente e acima de tudo, agradeço aos meu pais, **Renildes** e **Edemilson**, por sempre me incentivarem a estudar e seguir em frente mesmo nos momentos de desânimo. Aos meus irmãos **Vinicius** e **Marcelle**, por sempre estarem presentes em todos os momentos. À minha namorada **Késia**, por toda compreensão e carinho durante todos os momentos da vida acadêmica.

Ao meu orientador **Ricardo Trindade**, por além de cumprir muito bem seu papel de orientar, foi um grande parceiro nesses quatro anos, sempre me incentivando e passando para frente toda sua paixão pela ciência. Ao **Eric Tohver**, que mesmo informalmente, me coorientou neste trabalho, sendo de fundamental importância para o resultado final.

Aos grandes amigos do Laboratório de Paleomagnetismo (USPmag) que desde o meu início no laboratório, foram grandes parceiros e fizeram esses quatro anos passarem da forma mais leve possível. Destaco aqui, **Janine, Plínio, Jhon, Karine, Wilbor, Graziane, Danielle, Giovanne, Kamilla, Gelson, Ualisson, Thiago, Caio, Lívia, Rafael** e todos os outros.

Ao meu orientador durante meu estágio BEPE, **Mathew Domeier**, do CEED, que me acolheu muito bem e me deu toda assistência e orientação necessária para que o trabalho fosse realizado com sucesso, mesmo durante a pandemia. Aos amigos do CEED, que fizeram essa experiência ir muito além da academia, destaco aqui **Lea, Bjorn, Pratick** e **Florence**.

Aos amigos de outros institutos que colaboraram com este trabalho e que foram muito importantes nas etapas de campo, **Caroline, Lucas** e **Tiago**.

À Fundação de Amparo à Pesquisa do Estado de São Paulo (FAPESP) pelo apoio financeiro na forma de Bolsa de Doutorado pelo processo n° 2017/11672-0 e 2019/18892-1 (as opiniões, hipóteses e conclusões ou recomendações expressas neste material são de responsabilidade dos autores e não refletem necessariamente a visão da FAPESP).

Resumo

A distribuição latitudinal de massas continentais e cadeias de montanhas é um elemento chave na reconstrução paleoambiental durante o Ediacarano-Cambriano. Além da latitude imprecisa dos blocos para este intervalo de tempo, a idade e a evolução das cadeias de montanhas também não são bem determinadas ao longo da maior parte dos cinturões Brasiliano-Panafricanos. A Província da Mantiqueira, com aproximadamente 3.000 km de extensão, oferece uma rara oportunidade para estudar a fase de colapso gravitacional de um orógeno quente em diferentes níveis crustais. Esta tese começa a estabelecer uma estrutura para estudos do comportamento reológico em diferentes níveis crustais do orógeno Araçuaí (OA, porção norte da Província Mantiqueira), e reconstruções paleogeográficas do Gondwana utilizando paleomagnetismo e outras técnicas combinadas em plutons pós-orogênicos no OA. Primeiramente, um estudo detalhado de anisotropia de susceptibilidade magnética (ASM) revelou uma trama magnética de rochas contemporâneas (~ 500 Ma), em intrusões pós-colisionais, registrando diferentes padrões de fluxo interno. Na porção sul, intrusões profundas com forma elipsoidal mostram padrões concêntricos de tramas magnéticas que cortam a foliação regional de tendência NE-SW. Em contraste, as intrusões da porção norte, expostas como seções superiores de forma alongada a irregular de corpos de tamanho de batólito, colocadas na crosta rasa a média, mostram tramas magnéticas de tendência NS, aproximadamente paralelas ao *strike* do orógeno e da foliação regional. Este padrão contrastante reflete o comportamento reológico diferente ao longo de um perfil de escala crustal desde as raízes da intrusão no sul, cuja deformação é desacoplada da crosta circundante, até sua cúpula que surge no norte, que é co-estruturada com as rochas encaixantes na crosta média a rasa. Por fim, foi realizada uma análise paleomagnética dos plútons pós-colisionais Santa Angélica (SA) e Venda Nova (VN) (~ 500 Ma) da porção sul do OA. O pólo combinado SAVN (4,7 ° N, 332,2 ° E, N = 35, A95 = 4,06 e K = 68,82) corresponde ao setor Furongiano do final do Cambriano do APWP do Gondwana, que é quase totalmente dominado pelos resultados do Gondwana Oriental, portanto fornecendo uma nova restrição crítica para o bloco Congo-São Francisco no núcleo do Gondwana Ocidental. O corpo de pesquisa apresentado nesta tese oferece muitos desafios para futuros pesquisadores, ao mesmo tempo em que destaca que o magnetismo de rochas deve ser uma ferramenta útil para pesquisadores interessados na colocação de magma e reconstruções paleogeográficas.

Abstract

The latitudinal distribution of continental masses and mountain chains is a key element in the paleoenvironmental reconstruction of the Ediacaran-Cambrian times. Besides the unconstrained latitude of the blocks for this time interval, the age and evolution of the mountain chains is also undetermined along most of the Brasiliano-Panafrican belts. Featuring a 3000 km-long orogen, the Mantiqueira Province provides a rare opportunity to study collapsing orogens into their mid to deeper crustal sections. The following thesis begins to establish a framework for studies of the rheological behavior at different crustal levels of the collapsing Araçuaí orogen (AO, northern portion of the Mantiqueira Province), and paleogeographic reconstructions of the Gondwana using paleomagnetism and other combined techniques in post-collisional plutons of the belt. First, an in-depth study of magnetic anisotropy revealed contemporary (~500 Ma) but distinct magnetic fabric in post-collisional intrusions, recording different internal flow patterns. In the southern AO deep-seated intrusions with ellipsoidal-shape show concentric patterns of magnetic fabrics which cut across the NE-trending regional foliation. In contrast, the northern intrusions, exposed as elongate-to-irregular-shaped upper sections of batholith-size bodies, emplaced at the shallow to mid-crust, show general NS-trending magnetic fabrics roughly parallel to the strike of the orogen and the regional foliation of host rocks. This contrasting behavior reflects the different rheological behavior across a crustal-scale profile from the intrusion's roots in the south, whose deformation is decoupled from the surrounding crust, to their cupola that crop out in the north which is co-structured with the host rocks at the mid to shallow crust. Lastly, a paleomagnetic analysis was conducted on the post-collisional Santa Angélica (SA) and Venda Nova (VN) plutons (~500 Ma) from the southern portion of the AO. A combined SA plus VN pole computed from the magnetic results of both plutons (4.7° N, 332.2° E, N=35, A95=4.06 and K=68.82) does not resemble other poles from Gondwana or from the independent South American plate after the demise of Pangea. The SAVN pole closely matches the late Cambrian Furongian sector of the Gondwana path, which is near-entirely dominated by results from Eastern Gondwana, therefore providing a critical new constraint to the Congo-São Francisco block in the core of Western Gondwana. The body of research presented in this thesis provides many challenges to future workers, while at the same time highlighting that rock magnetism should be a useful tool for researchers interested in magma emplacement and paleogeographic reconstructions.

Table of contents

Chapter I

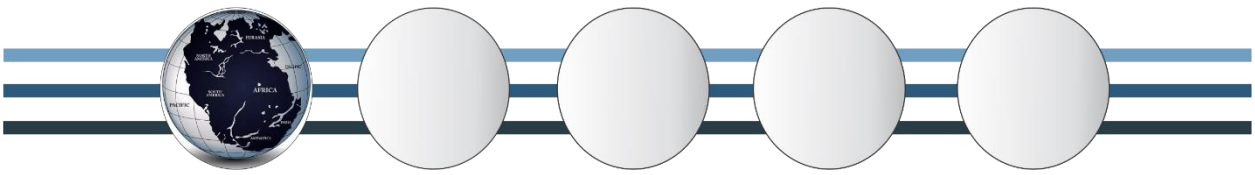

1. Introduction

1.1.Aim of study

This thesis is dedicated to the study of the late orogenic evolution of the Araçuaí fold belt. Its aim is twofold: (i) to constrain the rheological behavior at different levels of the crust as marked by the structures of magmatic rocks (magnetic anisotropy and microstructural analysis) from the core to the flanks of the collapsing Araçuaí orogen, whose age was provided by zircon U–Pb geochronology; (ii) to reassess the Cambrian drift of Gondwana through the paleogeographic reconstruction from the Ediacaran to the Cambrian, based on the paleomagnetic study of intrusive inversely zoned granitic-dioritic bodies of the Araçuaí orogen.

1.2.Project context

This thesis is part of a larger research effort that seeks to reconstruct the paleogeography, paleoclimate and paleobiological conditions of the planet during the Neoproterozoic. It is part of a thematic project funded by FAPESP entitled “The Neoproterozoic Earth System and the rise of biological complexity” (2016/06114-6), coordinated by Professor Ricardo Trindade. It comprises four subprojects (or work-packages): (1) Sedimentology, stratigraphy, and chronology of sedimentary successions, which provide the basis for a global perspective on the Neoproterozoic sedimentary record; (2) Evolution of the Biosphere, aiming at a better understanding of the possible interactions of life and the environment, particularly focused on the ocean oxygenation and nutrient availability in the oceans and their role in evolutionary innovations; (3) Ocean Chemistry, which is devoted to the study of biogeochemical cycles, ocean redox state and nutrients present in Ediacaran to Cambrian oceans; (4) Paleogeography, tectonics and numerical modeling of the Earth System at the end of the Neoproterozoic. Paleogeography and tectonics are key elements for understanding the evolution of the Earth System, particularly how the different proxies for oxygenation and nutrient availability, and the different organisms are distributed in time and space and their relation to the evolution of ancient mountain belts. The present thesis is included in subproject 4.

1.3. Problems related to the magma emplacement in orogens

Melt-bearing rocks are present in a variety of tectonic settings in the Earth's crust and mantle (Brown, 2007). They occur under orogenic plateaus associated to continental arcs (e.g. the Andes) and subduction-to-collision orogens (e.g. the Himalayas). At oceanic and continental arcs they represent the principal way to transfer mass from the mantle into the continental crust. In the terminal stage of subduction-to-collision orogenesis, melt extraction and magma ascent and emplacement also constitute a significant process of heat and mass transferring from lower to the upper continental crust.

In orogenic systems with sufficient increase in temperature, the core of the orogenic belt is significantly affected by partial melting (Vanderhaeghe, 2009; Jamieson and Beaumont, 2013). Tectonic processes in these large-hot orogens are dominated by the effects of the ductile flow of a weak infrastructure in response to differential pressure. The expression of this ductile flow depends on several factors, including: (i) source, rate, and duration of heating; (ii) the rheological structure of the crust and upper mantle and the corresponding flow modes within the orogen; and (iii) the source of the differential pressure, and the path of least resistance for lateral or vertical flow (Jamieson and Beaumont, 2013). The flow direction is determined by the path of least resistance, which may change as the system evolves (Unsworth et al., 2005). Ductile flow will continue after convergence stops as long as the crust remains weak and a differential pressure gradient is maintained. Therefore, in many cases, magmatic rocks are generated even when the collision ends (e.g. Guillot et al., 1993; Rey et al., 2009; Jamieson and Beaumont, 2011).

Granitic melt injection in the axial zone of relatively narrow orogenic belts are characterized regionally by a steep foliation developed under greenschist to amphibolite facies metamorphism in the surounding host rocks (Schulmann et al., 1994, Solar and Brown, 2001). Melt migration at depth within the partially-molten layer is likely to occur by melt percolation aided by heterogeneous rock deformation, whereas at higher structural level, in the intrusion zone, fracturing is the most probable mechanism (Vanderhaeghe, 2009). Crustal-scale vertical shear zones control the development of a network of granitic dikes feeding laccoliths of leucogranites emplaced within mylonitic zones at the amphibolite/greenschist facies transition that could represent a fossil brittle/ductile transition (Vigneresse, 1995, Zak et al., 2005). Both convergence-related forces and buoyancy of the melt act in concert to favor melt segregation within the steeply-dipping synmigmatitic foliation planes and upward melt migration along

these structural pathways. In contrast, sub-horizontal foliations associated with flattening and horizontal mass flow is expected at the core of the orogen.

Shear zones that extend from the core towards the flanks of the orogen, play the role of channelling the lateral and vertical magma flow (if shear zones are deep enough, e.g., Rey et al., 2009, Jamieson and Beaumont, 2013). The channel orientation and the degree of symmetry of the rock fabric are indicative of the forces and of the relative motion on the channel walls. The forces applied to the boundaries of the deforming zone encompass tectonic forces (basal traction and horizontal compression) and the gravity force associated with lateral variations of gravitational potential energy. Alternatively, considering a kinematic approach, this structural analysis leads to the identification of the relative motion along the sides of the deforming zone. The relative efficiency of the various mechanisms of melt segregation and magma mobility is a function of the rock rheology and of the regional strain rate (Rubin, 1993, Weinberg and Podladchikov, 1994). The rheology of the crust and the strain rate at which it deforms is, in turn, essentially controlled by its thermal evolution.

Such deep shear zones are important channels for ascent and emplacement of magma. To better understand magma ascent and emplacement processes it is important to simultaneously consider both the plutons and the crustal discontinuities that surround them. In the last decades many structural, petrological, and geochemical studies have been carried out to characterize the rheology and contextualize the tectonic environment of magma migration in orogenic belts. Hence, it is also extremely important to constrain their emplacement dynamics particularly at the late stages of the orogenic evolution when magma body forces may play an important role in magma transfer and emplacement.

1.4.Collapse mechanisms of orogens

The final stage of large, hot orogenic systems is commonly referred to as gravitational (or extensional) “collapse” (Dewey, 1988; Platt and Vissers, 1989; Rey et al., 2001). This leads to extension and ductile thinning of the orogenic core and contraction and thrusting on its flanks (Rey et al., 2001; Jamieson and Beaumont, 2011; Vanderhaeghe, 2012), which may accrete more material along the margins of the orogen. The knowledge of the temperature gradient from the core to the toes of the orogen in this last stage is therefore important for understanding the final deformation partitioning across the orogen and the emplacement of the last magmatic phases. When sigma 1 does not favor the gravitational collapse of a large and hot orogen, long

term landscape maintenance exists. This process leads to the absence of post-orogenic magmatism and to a slow and reasonably homogeneous denudational process.

The mechanism associated with the flow of material during the gravitational collapse may be related to the difference in potential energy between adjacent portions of the orogen (Rey et al., 2001). The excess of potential energy drives flow of material from the thickened crust to the immediately adjacent regions. Consequently, thinning affects elevated regions, whereas thickening affects the surrounding crust, contributing to the lateral growth of the orogenic domain (Jamieson and Beaumont, 2013). Three types of large-scale mass flow can be recognized depending on the partitioning of deformation accommodating gravitational collapse within the crust (Rey et al., 2001).

The first type of gravitational collapse is described in terms of gravity sliding of the upper crustal units away from the thick crust zone (Fig. 1.1a). In the second type, during collapse mass flow is restricted to the ductile lower crust, leaving the upper crust largely unaffected (Fig. 1.1b). Because this process does not leave any structural expression in the upper crust, it has been called ‘‘blind collapse’’. It leads to the thinning of the orogenic crust and thickening of the crust surrounding the plateau region. Blind collapse may explain the eastward displacement of the eastern topographic front of the Tibetan plateau, which is apparently not accommodated by active structures in the upper crust (Royden, 1996). The third type combines the previous two (Fig. 1.1c). Material from the upper crust is transferred towards the foreland and the ductile lower crust flows upward to fill the space beneath the detachment faults and towards the foreland regions which, therefore, undergo thickening. This type can be achieved when gravitational forces overcome the contractional strength of the surrounding lithosphere, thus triggering its bulk shortening.

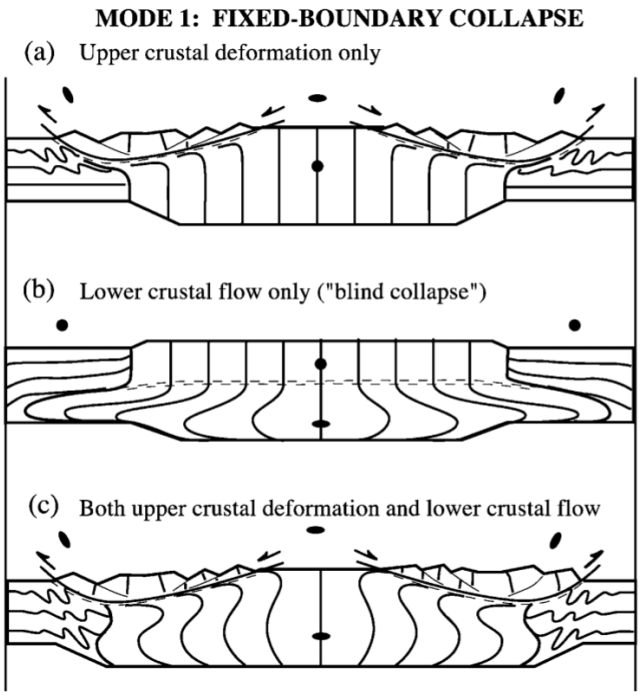

Figure 1.1 Models of the various types of divergent gravitational collapse affecting a thick continental crust. (a) Upper crustal deformation only; (b) lower crustal flow only 'blind collapse'; (c) both upper crustal deformation and lower crustal flow. Font: Rey et al. (2001).

According to Jaimieson and Beaumont (2013), no material would be added to the orogenic system after convergence ends. In this final stage, orogens will decay by the effects of erosion and gravitational collapse, whereby extension and crustal thinning reduces lithospheric overburden through lateral flow of the hot orogenic interior. Large-hot orogenic systems are dominated by lateral flow of hot orogenic infrastructure (e.g., Dewey, 1988; Platt and Vissers, 1989; Rey et al., 2001). This leads to extension and ductile thinning of the orogenic core and contraction and thrusting on its flanks (e.g., Rey et al., 2001; Jamieson and Beaumont, 2011; Vanderhaeghe, 2012), which may accrete more material to the toes of the orogen, although temperatures in the orogenic core may remain high for tens of millions of years (Jamieson et al., 2002; Jamieson and Beaumont, 2011). Postconvergent exhumation of deepseated metamorphic rocks accompanies erosion at the orogenic flanks and extension and ductile thinning in the orogenic core.

Many theoretical models and natural examples of gravitational collapse were proposed in the last decades in the Tibetan Plateau (Royden et al., 2008; Jessup et al., 2008), the Eastern Alps (Frisch and Kuhlemann, 2000) and the Canadian Cordillera (Vanderhaeghe and Teyssier, 2001). An interesting issue is the contrasting rheological behavior of the crust at different levels marked by the structures in magmatic rocks from the core to the flanks of the orogen. Such

specific relationships between the steep orogenic structures at the orogenic flanks and the late, pervasive subhorizontal structures in the orogenic core, were also observed in other natural large, hot orogens (e.g. Grenville orogen, Jamieson et al., 2010).

1.5. Ediacaran-Cambrian Paleogeography of Gondwana

Plate reconstructions at successive intervals in geological time are the result of a reiterative process using a wealth of methods (Torsvik and Cocks, 2017). Continents and terranes are reconstructed to their ancient positions on the globe using hotspot trails (Garnero et al., 2007) or paleomagnetic data (McCausland et al., 2011; Torsvik et al., 2012), and by identifying and discriminating between the distributions of various fauna and flora in their various provinces at different times (Scholle et al., 1995).

The latitudinal position of continental masses can be traditionally reconstructed using the fossil magnetic record present in rocks (Butler, 1992). Available paleomagnetic data provide good evidence regarding the formation of the Rodinia supercontinent, between 900 and 750 Ma (D'Agrella-Filho et al., 1998; Cordani et al., 2003; Tohver et al, 2006; Li et al., 2008, 2013). However, the range between 800 and 480 Ma (Tonian until the end of the Cambrian) has been particularly contentious (e.g. Abrajevitch and van der Voo, 2010; McCausland et al., 2011) and has little available high-quality data (Torsvik et al., 2012; Li et al., 2013). The Ediacaran and Cambrian periods are the more problematic because they show results that are mostly ambiguous, with completely different directions obtained in rocks of similar ages even after rigorous quality tests (McCausland et al., 2011; Bono and Tarduno, 2015). This uncertainty led to different paleogeographic and geodynamic models, with the continents distributed along the poles or close to the equator, depending on the arbitrary choice of the poles (McCausland et al., 2007, 2011; Abrajevitch and van der Voo, 2010; Torsvik et al., 2012).

During the time interval between Ediacaran and Cambrian, there were drastic changes on planet Earth, including a series of important changes in the configuration of continental masses and perhaps rotations involving the entire upper mantle (true polar wander events) (Mitchell et al., 2007; Schmidt et al., 2009; Robert et al., 2018). It was during this interval that the disruption and dispersion of the supercontinent Rodínia occurred followed by the formation of a new group of continents, Gondwana. In addition, the Neoproterozoic era is marked by periods of intense glaciation (Hoffman et al., 1998), with at least two events on a global scale. Also in that time interval, the biosphere has gone through one of its most fundamental evolutionary processes, over the interval between 800 Ma and 500 Ma life on Earth changed from

dominantly microscopic, unicellular organisms living in anoxic conditions to the emergence of complex life forms and the first multicellular forms under dominantly oxic conditions (Erwin et al., 2011; Knoll, 2011; Xiao, 2014).

Gondwana was the largest continental crustal unit on Earth for over 200 million years (Meert and Van der Voo, 1997). This supercontinent comprised the current African continent, Madagascar, India, Arabia, and much of southwestern Europe, South America, Antarctica, Australia (Torsvik & Cocks, 2011), and South China (Xian et al., 2019). Following the breakup of preceding supercontinental assemblies (Meert and Van der Voo, 1997), Gondwana was generated through a series of major orogenic events, including the East African and Brasiliano-Pan-African events, which marked the closure of several Neoproterozoic oceans (Kröner & Stern, 2005). The East African orogeny started the process between 800 and 650 Ma (Wilson et al., 1997), but the subsequent evolution of Gondwana remains somewhat unclear. Although the bulk of the supercontinent is generally considered to have been assembled by ca. 550 Ma (Meert and Van der Voo, 1997), some important cratonic elements (e.g. Amazonia, West Africa) may not have fully amalgamated with central Gondwana until the mid- to Late Cambrian (Trindade et al., 2006; Tohver et al., 2012; Wen et al., 2020), although an early amalgamation, at 650-600 Ma, has also been advocated (e.g., Cordani et al., 2013; Ganade de Araújo et al., 2014).

To reach a full understanding of this key terminal phase of Gondwana's assembly requires additional paleogeographic constraints. In addition, little is known about the topographic configuration of the great Ediacaran and Cambrian mountains, which may have been as important as the Alpes-Himalaya system today, with important consequences for atmospheric circulation and the planet's climate.

The early Cambrian poles (~520 Ma) from Western Gondwana (Trindade et al., 2006; Antonio et al., 2021) appear to diverge from the trend of the Gondwana APWP of Torsvik et al. (2012), implying that Western and Eastern Gondwana may have still been moving relative to one another immediately prior to the mid-Cambrian (Robert et al. 2018). In contrast, the APWP of the Gondwana supercontinent in the Late Cambrian is near-entirely dominated by results from the Eastern Gondwana. Therefore, the generation of new key poles for the western Gondwana is essential to assay if Eastern and Western Gondwana were approximately coherent at least by this time.

2. Organization of this thesis

This article-based thesis contains three first-authored papers published or submitted to international scientific journals. The following papers make up Chapters II-IV of the thesis:

Paper I was published in the journal Tectonics. This paper explores the magnetic fabric and geochronology of the Santa Angélica (SA) post-collisional pluton. It provides three new U-Pb ages on zircon grains from different facies of the SA pluton showing they are coeval and cristalized in the Cambrian. The SA pluton corresponds to two inversely-zoned partly overlapping plutons emplaced along pre-existing high angle ductile shear zones. Anisotropy of magnetic susceptibility (AMS) and of anhysteretic remanence (AAR) combined with microstructural data suggest that magma emplacement was controlled by magma buoyancy forces, (almost) free of stress tectonic. Such pattern is also presented in others Cambrian post-collsional plutons from the southern portion of the orogen.

Paper II was submitted to the journal Geology and reports a detailed mapping of magnetic fabrics (AMS) of coeval plutons at different sectors of the belt, north and south, also corresponding to different crustal levels. This allowed us to assess a crustal scale section of the Araçuai belt, from its roots in the south to the upper crust in the north. The contrasted fabric patterns observed in plutons from these different areas highlight the different rheological conditions across the crust during the late orogenic gravitational collapse stage.

Paper III was published in the journal Precambrian Research. In this paper we report a paleomagnetic study of the ~500 Ma post-collisional plutons of Santa Angelica (SA) and Venda Nova (VN), located in the southern portion of the Araçuaí belt. Together, paleomagnetic results from 35 sites distributed between the two plutons allows the computation of a new reference paleopole (labeled SAVN) located at: 4.7° N, 332.2° E, A95=4.0° and K=68.8. Our new result is a reference pole for Western Gondwana for the Furongian Epoch (Cambrian Period). Considerations of the Cambrian paleomagnetic data from Eastern and Western Gondwana suggest that while the supercontinent was undoubtedly amalgamated by ~500 Ma, there was likely significant motion between Eastern and Western Gondwana in the early Cambrian.

3. References

Abrajevitch, A. and Van der Voo, R., (2010). Incompatible Ediacaran paleomagnetic directions suggest an equatorial geomagnetic dipole hypothesis. *Earth and Planetary Science Letters*, 293(1-2), 164-170.

Antonio, P.Y.J., Trindade, R.I.F., Giacomini, B., Brandt, D. and Tohver, E., (2021). New high-quality paleomagnetic data from the Borborema Province (NE Brazil): Refinement of the APW path of Gondwana in the Early Cambrian. *Precambrian Research*, 360, 06243.

Bono, R.K. and Tarduno, J.A., (2015). A stable Ediacaran Earth recorded by single silicate crystals of the ca. 565 Ma Sept-Îles intrusion. *Geology*, 43(2), 131-134.

Brown, M. (2007). Crustal melting and melt extraction, ascent and emplacement in orogens: mechanisms and consequences. *Journal of the Geological Society*, 164, 709-730. https://doi.org/10.1144/0016-76492006-171.

Butler, R.F., (1992). Paleomagnetism: magnetic domains to geologic terranes, Blackwell Pub., 223 pp.

Dewey, J.F., (1988). Extensional collapse of orogens: *Tectonics*, v. 7, p. 1123–1139, doi:10.1029/TC007i006p01123.

Cordani, U.G., D'Agrella-Filho, M.S., Neves, B.B.B., Trindade, R.I.F. (2003). Tearing up Rodinia: the Neoproterozoic palaeogeography of South American cratonic fragments. *Terra Nova*, 15, 350-359

D'Agrella Filho, M.S. et al., (2000). Simultaneous remagnetization and U–Pb isotope resetting in Neoproterozoic carbonates of the São Francisco craton, Brazil. *Precambrian Research*, 99(3-4), pp.179– 196.

Erwin, D.H. et al., (2011). The Cambrian Conundrum: Early Divergence and Later Ecological Success in the Early History of Animals. *Science*, 334(6059), pp.1091–1097.

Frisch W., Dunkl, I., Kuhlemann, J., (2000). Post-collisional orogen-parallel large-scale extension in the Eastern Alps: *Tectonophysics*, v. 327, p. 239-265. DOI:10.1016/S0040-1951(00)00204-3.

Ganade de Araujo, C.E., Weinberg, R.F., Cordani, U.G., (2014). Extruding the Borborema Province (NE-Brazil): a two-stage Neoproterozoic collision process. *Terra Nova*, 26, 157-168. https://doi.org/10.1111/ter.12084

Garnero, E.J., Lay, T, Mcnamara, A.K., (2007). Implications of lower mantle structural heterogeneity for existence and nature of whole mantle plumes. In G.R. Foulger & D.M. Jurdy (eds.), Plates, Plumes and Planetary Processes. Geological Society of America Special Paper, 430, 79-101.

Guillot S., Pêcher, A., Rochette, P., Le Fort, P. (1993). The emplacement of the Manaslu granite of Central Nepal: field and magnetic susceptibility constraints. *Geological Society*, 74, 413-428. 10.1144/GSL.SP.1993.074.01.28.

Hoffman, P.F. et al., (1998). A Neoproterozoic snowball earth. *Science*, 281(5381), pp.1342–1346. DOI: 10.1126/science.281.5381.1342

Jamieson, R.A., Beaumont, C., Nguyen, M.H., and Lee, B., (2002). Interaction of metamorphism, deformation, and exhumation in large convergent orogens. *Journal of Metamorphic Geology*, v. 20, p. 9–24, doi:10.1046/j.0263-4929.2001.00357.x

Jamieson, R.A., Beaumont, C., Warren, C.J., Nguyen, M.H., (2010). The Grenville Orogen explained? Applications and limitations of integrating numerical models with geological and geophysical data. *Can. J. Earth Sci*. 47: 517–539.

Jamieson, R.A., and Beaumont, C., (2011). Coeval thrusting and extension during post-convergent ductile flow— Implications for exhumation of high-grade metamorphic rocks. *Journal of Metamorphic Geology*, 29, 33–51. doi:10.1111/j.1525-1314.2010.00908.x

Jamieson, R. A., and Beaumont, C., (2013). On the origin of orogens. *GSA Bulletin*, v. 125, p. 1671-1702, https://doi.org/10.1130/B30855.1.

Jessup, M.J., Newell, D.L., Cottle, J.M., Berger, A.L., Spotila, J.A., (2008). Orogen-parallel extension and exhumation enhanced by denudation in the trans-Himalayan Arun River gorge, Ama Drime Massif, Tibet-Nepal. *Geology*, v. 36; p. 587-590. doi:10.1130/G24722A.1.

Knoll, A.H., (2011). The Multiple Origins of Complex Multicellularity. dx.doi.org, 39(1), pp.217–239. Knoll, A.H. & Sperling, E.A., 2014. Oxygen and animals in Earth history. Proceedings of the National Academy of Sciences, 111(11), pp.3907–3908.

Kröner, A., Stern, R.J., (2005). Africa: Pan-African Orogeny. Encyclopedia of Geology, vol. 1, Elsevier, Oxford (2005), pp. 1-13.

Li, Z.-X., Evans, D.A.D. & Halverson, G.P., (2013). Neoproterozoic glaciations in a revised global palaeogeography from the breakup of Rodinia to the assembly of Gondwanaland. *Sedimentary Geology*, 294, pp.219–232.

Li, Z.X., Bogdanova, S., Collins, A.S., Davidson, A., De Waele, B., Ernst, R.E., Fitzsimons, I.C.W., Fuck, R.A., Gladkochub, D.P., Jacobs, J. and Karlstrom, K.E., (2008). Assembly, configuration, and break-up history of Rodinia: a synthesis. *Precambrian research*, 160(1-2), pp.179-210.

McCausland, P.J.A., Van der Voo, R., Hall, C.M., (2007). Circum-Iapetus paleogeography of the Precambrian–Cambrian transition with a new paleomagnetic constraint from Laurentia. *Precambrian Research*, 156, 125-152. https://doi.org/10.1016/j.precamres.2007.03.004

McCausland, P.J.A. et al., (2011). Ediacaran paleogeography of Laurentia: Paleomagnetism and Ar–Ar geochronology of the 583 Ma Baie des Moutons syenite, Quebec. *Precambrian Research*, 187(1-2), pp.58–78. Meert, J. G., & Voo, R. V. D.

Meert, J.G., Van der Voo, R., (1997). The assembly of Gondwana 800–550 Ma. *Journal of Geodynamics*, 23, 223–235. https://doi.org/10.1016/S0264-3707(96)00046-4.

Mitchell, R. N., Kilian, T. M., & Evans, D. A., (2012). Supercontinent cycles and the calculation of absolute palaeolongitude in deep time. *Nature*, 482(7384), 208-211.

Platt, J.P., and Vissers, R.L.M., (1989), Extensional collapse of thickened continental lithosphere: A working hypothesis for the Alboran Sea and Gibraltar arc. *Geology*, v. 17, p. 540–543, doi:10.1130/0091-7613(1989)017<0540:ECOTCL>2.3.CO;2.

Rey, P., Vanderhaeghe, O., and Teyssier, C., (2001). Gravitational collapse of the continental crust: Defi nition, regimes and modes. *Tectonophysics*, 342, 435–449. doi:10.1016/S0040-1951(01)00174-3.

Robert, B., Greff-Lefftz, M., Besse, J., (2018). True Polar Wander: A Key Indicator for Plate Configuration and Mantle Convection During the Late Neoproterozoic. *Geochemistry, Geophysics, Geosystems*. 19, 3478–3495. DOI: 10.1029/2018GC007490.

Royden, L.H., (1996). Coupling and decoupling of crust and mantle in convergent orogens: Implications for strain partitioning in the crust. *Journal of Geophysical Research*, v. 101, p. 17,679–17,705, doi:10.1029/96JB00951.

Royden, L.H., Burchfi el, B.C., and van der Hilst, R.D., (2008). The geological evolution of the Tibetan Plateau. *Science*, v. 321, p. 1054–1058, doi:10.1126/science.1155371.

Rubin, A.M., (1993). On the thermal viability of dikes leaving magma chambers. *Geophysical Research Letters*, 20:4, 257-260.

Schmidt, P.W., Williams, G.E. & McWilliams, M.O., (2009). Palaeomagnetism and magnetic anisotropy of late Neoproterozoic strata, South Australia: Implications for the palaeolatitude of late Cryogenian glaciation, cap carbonate and the Ediacaran System. *Precambrian Research*, 174(1-2), pp.35–52.

Schulmann., K. Melkan, R., Lobkowicz, M.Z., Ledru, P., Lardeaux, J.P., Autran, A., (1994). Contrasting styles of deformation during progressive nappe stacking at the southeastern

margin of the Bohemian Massif (Thaya Dome). *Journal of Structural Geology*, 16:3, 355-370. https://doi.org/10.1016/0191-8141(94)90040-X.

Scholle P.A. (1995). Carbon and Sulfur Isotope Stratigraphy of the Permian and Adjacent Intervals. In: Scholle P.A., Peryt T.M., Ulmer-Scholle D.S. (eds) The Permian of Northern Pangea. Springer, Berlin, Heidelberg. https://doi.org/10.1007/978-3-642-78593-1_9

Solar, G. and Brown, M., (2001). Deformation partitioning during transpression in response to Early Devonian oblique convergence, northern Appalachian orogen, USA. *Journal of Structural Geology*, 23: 6–7, 1043-1065. https://doi.org/10.1016/S0191-8141(00)00175-9

Tohver, E.; D'agrella Filho, M.S.; Trindade, R.I.F. (2006). Paleomagnetic record of Africa and South America for the 1200-500 Ma interval, and evaluation of Rodinia and Gondwana assemblies. *Precambrian Research*, 147, 193-222.

Tohver, E., Cawood, P.A., Rossello, E.A., Jourdan, F., (2012). Closure of the Clymene Ocean and formation of West Gondwana in the Cambrian: Evidence from the Sierras Australes of the southernmost Rio de la Plata craton, Argentina. *Gondwana Research*. 21, 394–405. 10.1016/j.gr.2011.04.001.

Torsvik, T.H., Cocks, R.M., (2011). The Palaeozoic palaeogeography of central Gondwana. *Geological Society*, London, Special Publications, 357, 137-166. https://doi.org/10.1144/SP357.8.

Torsvik, T., & Cocks, L. (2017). Earth History and Palaeogeography. Cambridge: Cambridge University Press. doi:10.1017/9781316225523.

Torsvik, T.H., Van der Voo, R., Preeden, U., Niocaill, C.M., Steinberger, B., Doubrovin, P.V., van Hinsbergen, D.J.J., Domeier, M., Gaina, C., Tohver, E., Meert, J.G., McCausland, J.A., Cocks, R.L.M., (2012). Phanerozoic polar wander, palaeogeography and dynamics. *Earth-Science Reviews*. 114: 325–368. doi: 10.1016/j.earscirev.2012.06.007.

Trindade, R.I.F., D'Agrella-Filho, M.S., Epof, I., Brito Neves, B.B., (2006). Paleomagnetism of Early Cambrian Itabaiana mafic dikes (NE Brazil) and the final assembly of Gondwana. *Earth and Planetary Science Letters*. 244, 361–377. https://doi.org/10.1016/j.epsl.2005.12.039

Unsworth, M., Jones, A., Wei, W. et al., (2005). Crustal rheology of the Himalaya and Southern Tibet inferred from magnetotelluric data. *Nature* 438, 78–81. https://doi.org/10.1038/nature04154.

Vanderhaeghe, O., Teyssier, C., (2001). Crustal-scale rheological transitions during late-orogenic collapse. *Tectonophysics*, v. 335, p. 211-228. DOI:10.1016/S0040-1951(01)00053-1.

Vanderhaeghe, O. (2009). Migmatites, granites and orogeny: Flow modes of partially-molten rocks and magmas associated with melt/solid segregation in orogenic belts. *Tectonophysics*, 477:3-4, 119-134. https://doi.org/10.1016/j.tecto.2009.06.021.

Vanderhaeghe, O., (2012). The thermal-mechanical evolution of crustal orogenic belts at convergent plate boundaries: A reappraisal of the orogenic cycle: *Journal of Geodynamics*, v. 56–57, p. 124–145, doi:10.1016/j.jog.2011.10.004.

Vigneresse, J.L., (1995). Control of granite emplacement by regional deformation. *Tectonophysics*, 249, 173-186. https://doi.org/10.1016/0040-1951(95)00004-7

Weinberg, R.F., Podladchikov, Y., (1994). Diapiric ascent of magmas through power law crust and mantle. *Journal of Geophysical Research*, 99, 9543-9559.

Wen, B., Evans, D.A., Anderson, R.P. and McCausland, P.J., (2020). Late Ediacaran paleogeography of Avalonia and the Cambrian assembly of West Gondwana. *Earth and Planetary Science Letter*s, 552, p.116591.

Wilson, T.J., Grunow, A.M., Hanson, R.E., (1997). Gondwana assembly: The view from Southern Africa and East Gondwana. *Journal of Geodynamics*. 23, 263-286. https://doi.org/10.1016/S0264-3707(96)00048-8.

Xian, H., Zhang, S., Li, H., Xiao, O., Chang, L., Yang, T., Wu, H., (2019). How Did South China Connect to and Separate from Gondwana? New Paleomagnetic Constraints From the Middle Devonian Red Beds in South China. *Geophysical Research Letters*. 46, 7371-7378. https://doi.org/10.1029/2019GL083123.

Xiao, S. et al., (2014). The Weng'an biota and the Ediacaran radiation of multicellular eukaryotes. *National Science Review*, 1(4), pp.498–520.

Zak, J., Schulmann, K., Hrouda, F., (2005). Multiple magmatic fabrics in the Sazava pluton (Bohemian Massif, Czech Republic): a result of superposition of wrench-dominated regional transpression on final emplacement. *Journal of Structural Geology*, 27:5, 805-822. https://doi.org/10.1016/j.jsg.2005.01.012.

Chapter II

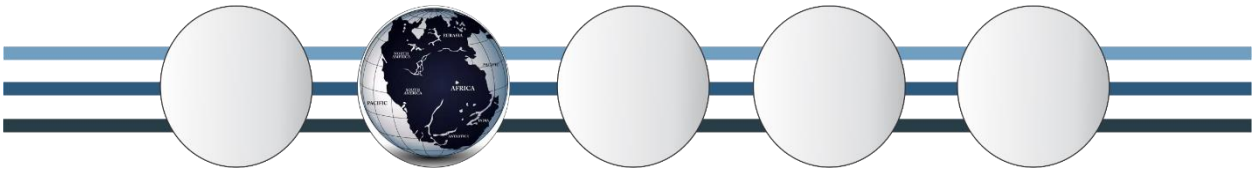

Magnetic fabric and geochronology of a Cambrian “isotropic” pluton in the Neoproterozoic Araçuaí orogen

F. A. Temporim, R. I. F. Trindade, E. Tohver, C. C. Soares, L. P. Gouvêa, M. Egydio-Silva, C. A. D. Amaral, G. F. Souza Jr.

Published in *Tectonics* in May 2020, https://doi.org/10.1029/2019TC005877

For supporting material see Appendix A

Abstract: The Araçuaí Orogen (AO) has been interpreted as a Neoproterozoic example of a large, “hot” orogen, based on a broad zone (250 km) of midcrustal metamorphic assemblages with a long, 70-Myr history of crustal melting and episodic magmatism throughout the late Neoproterozoic and earliest Paleozoic. Here, we present results of U-Pb sensitive high-resoution ion microprobe (SHRIMP) zircon dating and detailed anisotropy of magnetic susceptibility (AMS) study on a late Cambrian, bimodal pluton related to final period of collapse of the AO. New U-Pb zircon ages constrain the crystallization age of different suites within the Santa Angélica Pluton, 506 ± 3 Ma for the early felsic phase and 498 ± 5 Ma for the mafic core. New AMS data indicate that the emplacement of the Santa Angélica Pluton corresponds to two coupled plutons with concentric structures arrayed about a twin, bull's eye pattern. During the final stages of intrusion, upward relative movement of the northeastern lobe exposed the deeper levels of the intrusion, relative to the more shallowly eroded southwestern lobe. These observations suggest that magma emplacement was controlled by magma buoyancy forces, with little influence of regional tectonic stress. This behavior contrasts with the well-defined, tectonic-controlled fabrics of coeval plutons occurring to the north which was still hot, therefore highlighting the contrasting thermal evolution between different sectors of the orogen during its final stages.

1 Introduction

Large, hot orogens were defined by Beaumont et al. (2006) as the product of long-standing convergence and burial of heat-producing, radioactive elements in mountain belts. In this scenario, crustal rheology is dominated by widespread melting of the middle crust, and the orogenic architecture is symmetric, with deformation homogeneously distributed throughout a wide and thick, plateau-like structure (Jamieson & Beaumont, 2013). Such a style of tectonic deformation has been ascribed to the Himalayan-Tibetan Orogen (Jamieson & Beaumont, 2013), as well as the Grenville Orogen of North America (Davidson, 1995). The final stage of large, hot orogenic systems evolution is commonly referred to as gravitational (or extensional) "collapse" (Dewey, 1988; Platt & Vissers, 1989; Rey et al., 2001). This leads to extension and ductile thinning of the orogenic core and contraction and thrusting on its flanks (Jamieson & Beaumont, 2011; Rey et al., 2001; Vanderhaeghe, 2012), which may accrete more material along the margins of the orogen. The knowledge of the distribution of the temperature gradient from the core to the toes of the orogen in this last stage is therefore important for understanding the final deformation partitioning across the orogen and the emplacement of the last magmatic phases.

The amalgamation of Gondwana has created the large, Araçuaí Orogen (AO) in southeast Brazil, (Cavalcante et al., 2019; De Campos et al., 2004, 2016; Fossen et al., 2017; Pedrosa-Soares et al., 1999, 2006; Vauchez et al., 2007; Wiedeman et al., 2002). The AO records a long period of crustal melting, with over 70 Myr of episodic magmatism, terminating in the Cambro-Ordovician period and characterized by intense magmatism during the waning to post-collisional stages of convergence following the formation of Gondwana (Pedrosa-Soares & Wiedemann-Leonardos, 2000). Post-collisional plutons from the Araçuaí Belt are reported with ages ranging from 535 to 480 Ma (De Campos et al., 2004, 2016). According to Söllner et al. (2000), these bodies arose from the gravitational collapse marking the end of the western Aracuaí-Congo Orogen construction. Preliminary aeromagnetic studies (Bosum, 1973) and remote sensing data sets (Meneses & Paradella, 1978) have delineated some of these plutons, and detailed geological work revealed their complex internal facies distributions (Bayer et al., 1987; Medeiros et al., 2001; Wiedeman et al., 2002; Wiedemann et al., 1986). The Santa Angélica Pluton, the subject of the current study, exhibits an inverse composite zonation formed by the interdigitation of basic to intermediate composition magmas at the core and syenomonzonites to granites along the border, with widespread magma mingling and mixing zones (Bayer et al., 1987; Wiedemann et al., 1986). Few structural studies have been carried

out within the Santa Angélica Pluton, which appears to be isotropic except for a strong foliation developed along the pluton's margins (Bayer et al., 1987).

A magma's ascent and final emplacement is a dynamic physical and chemical process, one where conductive heat loss at cooler, shallower depths is countered by the latent heat of crystallization released by the nucleation and growth of phenocrysts. In basaltic magmas, a phenocryst population that reaches the limit of 55% crystallinity effectively freezes the magma in place, with the viscosity of the crystal mush now dominated by a “load-bearing” framework of touching grains with interstitial liquid (Marsh, 1981). For more silica-rich magmas, the basic thermodynamics of this process does not change, but the lower liquidus temperatures, higher buoyancy, and higher viscosity of a polymerized, silica-rich magma alter the boundary conditions of the system, for example, reducing the crystallinity limit for eruption of liquid magma. Instead, the continued, buoyancy-driven, upward ascent of felsic magmas progresses under a solid-state regime, and rock fabrics dominated by magmatic shape-preferred orientations (SPOs) evolve to the lattice-preferred orientation (LPO) developed by high temperature, intracrystalline deformation processes. The knowledge of the fabric pattern and the microstructural state of a pluton is essential for interpreting the pluton emplacement model in terms of magmatic versus tectonic processes (Bouchez, 1997; Cruden & Launeau, 1994; Sant'Ovaia et al., 2000). Therefore, to study the fabric patterns of plutons allows the explanation of the tectonic scenario that prevailed at the moment of their emplacement.

The presence, or absence, of a macroscopically visible planar structure in a granitic rock is the source of the old distinction between oriented or structured and equant or massive rock types (Bouchez, 1997). The syn- or post-tectonic character of a pluton is often deduced from considerations of regional structures and geochemical and chronological data (Almeida et al., 2002; Chung et al., 2005; Medeiros et al., 2000; Perpétuo et al., 2016). The problem is that even apparently isotropic granites generally contain some internal fabric, however cryptic (Bouchez, 1997). A study of anisotropy of magnetic susceptibility (AMS) in several apparently isotropic plutons (Archanjo & Bouchez, 1997; Gleizes et al., 2006; Oliveira et al., 2010; Raposo & Gastal, 2009; Salazar et al., 2008; Sant'Ovaia et al., 2000) indicates patterns of magnetic foliation and lineation that reflect magmatic processes and are coherent across all the magmatic facies of a single, plutonic body. In this paper, we present results of an integration of U-Pb sensitive high-resoution ion microprobe (SHRIMP) and a detailed AMS study to determine the emplacement mechanisms of the Santa Angélica. This pluton was emplaced at the midcrustal section of the Araçuaí orogenic system and is located along its southern toe. Its

internal fabric pattern will provide information on the final deformation partitioning at the waning stages of mountain building across this crustal level that is presently inaccessible in modern orogens.

2 Geological setting

2.1 Regional context

The AO represents the Brazilian counterpart of the Araçuaí West Congo orogenic system (Pedrosa-Soares et al., 2001, 2008). This Neoproterozoic-Cambrian Orogen is contained in the great recess delineated on three sides by ancient, crystalline basement rocks of the São Francisco and Congo cratons (Pedrosa-Soares & Wiedemann-Leonardos, 2000). The Araçuaí Belt merges to the south with the coastal Ribeira Belt, forming the Araçuaí-Ribeira orogenic system (AROS) (Egydio-Silva et al., 2018) (Figure 2.1a). These two belts form part of a collage of eastern South American and western African mobile belts of late Neoproterozoic to early Paleozoic age that marks the assembly of western Gondwana (Alkmim et al., 2006; Vauchez et al., 2007).

The AO has been interpreted in two ways: as a confined orogen, where magmatism and deformation are related to oceanic lithosphere subduction and arc-continent collision (Amaral et al., 2020; Pedrosa-Soares et al., 2001, 2008), or as a hot orogen in which the long-lived partial melting and magmatism of its internal domain would be developed in an intracontinental setting (Cavalcante et al., 2018, 2019; Fossen et al., 2017; Vauchez et al., 2007). Both models accommodate the fact that a volumetrically extensive magmatism was active in the orogen over a long period of time (cooling at <3°/Myr until 500 Ma) sustaining high geothermal gradients (Cavalcante et al., 2018; Munhá et al., 2005; Petitgirard et al., 2009; Richter et al., 2016). The magmatic suites within the AO have been interpreted as broadly episodic by Pedrosa-Soares and Wiedemann-Leonardos (2000) based on the structural relationship between plutonic suites and regional geology (Figure 2.1b), geochemical and isotopic signatures, and U-Pb geochronology. These authors grouped the different plutonic rocks from the AO into five supersuites that follow the typical geochemical and structural evolution of collisional settings and range in age from the early Ediacaran to the Cambrian-Ordovician times (630–480 Ma): pre-collisional G1 (630–580 Ma), syn-collisional G2 (585–545 Ma), late collisional G3 (545–530 Ma), post-collisional G4 (530–500 Ma), and G5 (530–480 Ma) (Figure 2.1a).

The G1 supersuite mainly consists of pre-collisional batholiths and stocks of tonalite to granodiorite. Geochemical data from several G1 plutons point toward calc-alkaline, metaluminous to fairly peraluminous magmas (Campos-Neto & Figueiredo, 1995; Pedrosa-Soares et al., 1999). Mafic facies and enclaves are common in these bodies that were deformed during the Brasiliano orogeny albeit with magmatic features well preserved locally (Narduzzi et al., 2017; Pedrosa-Soares & Wiedemann-Leonardos, 2000; Petitgirard et al., 2009; Vieira, 2007). The G2 supersuite is interpreted as syn-collisional intrusions, mostly of peraluminous granites (Gradim et al., 2014; Heilbron & Machado, 2003; Noce et al., 2000; Silva et al., 2002). In map view, this supersuite forms a continuous NS-trending belt, extending for over 350 km along AROS northeastern sector (Cavalcante et al., 2013; Mondou et al., 2012). The G3 supersuite are late collisional leucogranites, also of peraluminous composition. According Pedrosa-Soares et al. (2000), the rocks of the G3 supersuite are much less voluminous than the G2 granites with which they are spatially associated.

The G4 and G5 supersuites represent a post-collisional granite population and correspond to the youngest plutonic rocks of the AROS (Pedrosa-Soares & Wiedemann-Leonardos, 2000). Typical rocks of the G4 and G5 suites are charnockite and biotite-granites with ages from ~ 540 to 480 Ma (Noce et al., 2000; Petitgirard et al., 2009; Söllner et al., 1991). These plutons of "I-type" granitoid are larger and more common in the northern portion of the Araçuaí Belt (Pedrosa-Soares et al., 2001), defined as the hot internal zone by Vauchez et al. (2007). The Santa Angélica Pluton forms part of G5 supersuite and is located in the southern portion of the Araçuaí Belt, more distal to the hot interior (Figure 2.1b). In this part of the orogen, some I-type plutons (including Santa Angélica) were emplaced along high-angle, ductile shear zones and in the core of preexisting antiform structures (Pedrosa-Soares & Wiedemann-Leonardos, 2000; Schmidt-Thomé & Weber-Diefenbach, 1987). Recently, Santiago et al. (2020) identified the last magmatic events in the Araçuaí Belt, comprising two generations of mafic dike swarms, which are associated to the collapsing orogen (500 Ma) and to the breakdown of western Gondwana (140 Ma).

vi

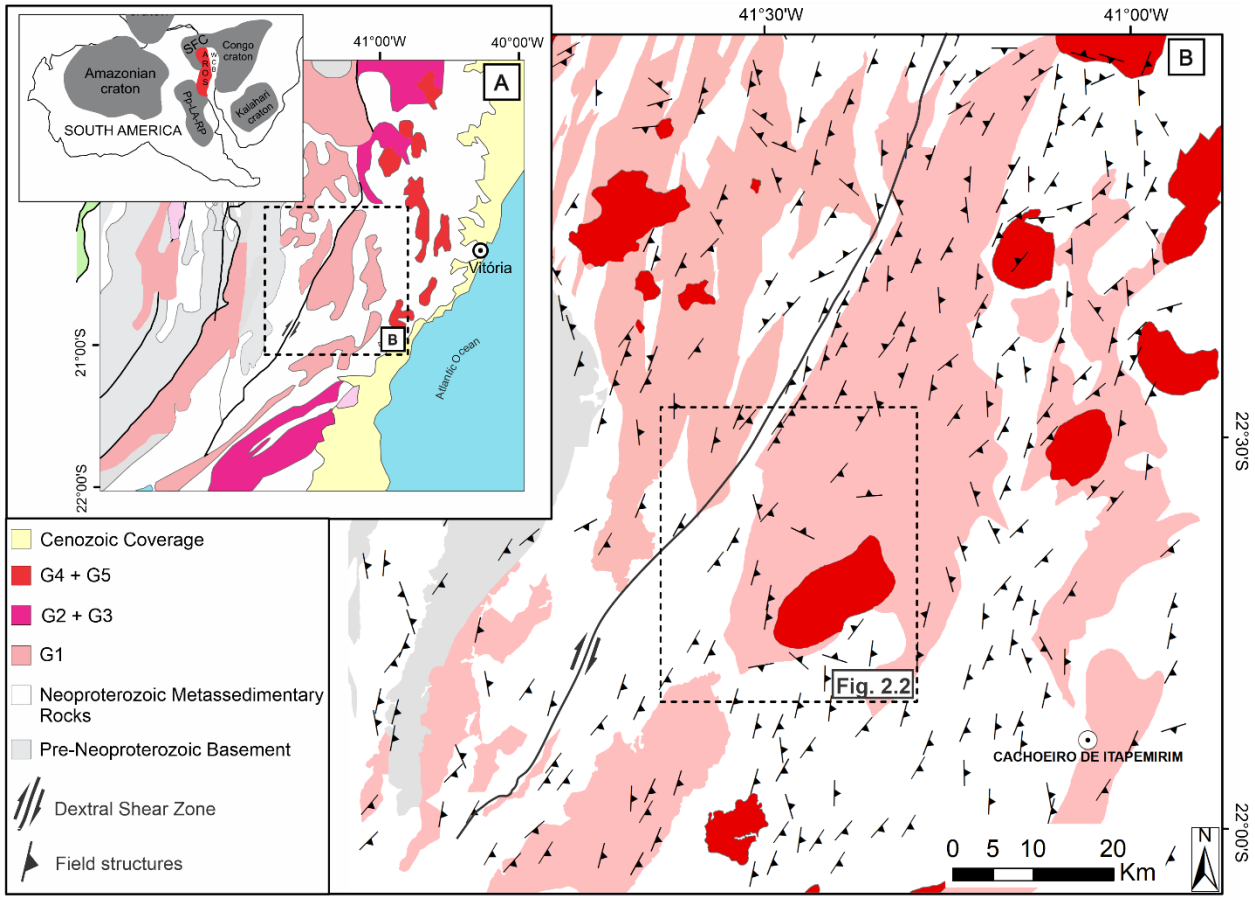

Figure 2.1. (A) Simplified geological map of the Araçuaí-Ribeira orogenic system (AROS) and its location in Western Gondwana with emphasis on the Neoproterozoic magmatic supersuites (modified from Silva et al., 2005; Pedrosa Soares and Wiedmann-Leonardos, 2000). (B) Geological map and field structures (modified from Silva et al., 2005). The dotted square delimits the study area of the Santa Angélica pluton represented in Figure 2.2. Pp-La-Rp: Paranapanema, Luíz Alves and Rio de la Plata cratons.

2.2. Shape and facies distribution of the Santa Angelica pluton

The Santa Angélica Pluton (Figure 2.2) covers about 200 km^2 and is an elliptical-shaped intrusion elongated along a NE-SW axis and with concentric structures arrayed about a twin, bull's eye pattern. The rocks are high K, calc-alkaline, and highly enriched in light rare earth elements (Horn & Weber-Diefenbach, 1987). The country rocks are biotite-garnet-sillimanite gneisses and biotite-hornblende granodioritic to tonalitic gneisses (G1 supersuite) that are locally migmatized. Contacts between the intrusion and the country rock are subvertical, and the foliation at the border of the pluton is parallel to the contact with the country rocks. This foliation dips toward the interior of the intrusion (Figures 2.1b and 2.2). At distances greater than 1–2 km from the contact with the country rock, the foliation is concordant with the

regional NE-SW trend. This regional foliation is marked by the trend of the Guaçuí shear zone (Figure 2.1b), which is defined by vertical to subvertical mylonites that formed under transpressive, dextral deformation (Figures 2.3a and 2.3b) (Horn, 2006).

The Santa Angélica Pluton is inversely zoned with felsic rocks at the margins and more intermediate-mafic rocks toward the cores of the intrusion. This compositional variation defines a twin “bull's eye” pattern with two adjacent nodes. The intermediate-mafic rocks are described by Schmidt-Thomé and Weber-Diefenbach (1987) as gabbro-diorite and are more abundant in the two cores of the pluton. The mineralogical assemblage of these rocks are dominantly plagioclase, clinopyroxene, biotite, and opaque minerals (mostly oxides) and subordinate amounts of quartz, with zircon and apatite as common accessory phases. The felsic rocks are informally divided by Schmidt-Thomé and Weber-Diefenbach (1987) into two types, an earlier “Type I” suite of coarse-grained, porphyritic rocks with abundant allanite as a characteristic accessory phase, and a younger “Type II” granitoid that is finer grained and contains titanite as a prominent accessory phase. The contacts between both types are sharp, indicating that Type II rocks were emplaced under brittle conditions (Schmidt-Thomé & Weber-Diefenbach, 1987). The commingling and mixing zone are defined through field and geochemical data by Bayer et al. (1987). Hybrid rocks, resulting from commingling of basic and acidic magmas, are widespread in the intrusion. Mingling of two magmas with contrasting physical properties resulted in typical structures, such as schlieren, forming large mingled zones of enclave swarms in different degrees of hybridization with the granite (Figures 2.3c and 2.3d). Mixing of magmas with less contrasting physical properties resulted in more homogeneous hybrid rocks, exhibiting xenocrysts with disequilibrium features like mantling and corona structures, forming large mingled zones of enclave swarms in different degrees of hybridization with the granite (Figures 2.3c and 2.3d). Type I granite is strongly foliated parallel to the country rock contact on practically all borders of the pluton (Figures 2.3e and 2.3f).

A main NNW-SSE internal shear zone separates the two gabbroic cores (Schmidt-Thomé & Weber-Diefenbach, 1987). The shear zone appears to form part of the regional Alegre Lineament studied by Calegari et al. (2016). This ~250-km lineament functioned as a fault that was active both onshore and offshore. There is a set of NNW-SSE-oriented fractures formed by extensional activities in the early Cambrian, and this zone was reactivated as normal faults during the Cenozoic (Calegari et al., 2016).

Few geochronological data from the Santa Angélica Pluton have been reported, and the interpreted ages are imprecise and at odds with field relations. U-Pb zircon ages were obtained by Söllner et al. (1991) for granite Type I (492 ± 15 Ma) and for granite Type II (513 ± 8 Ma) by ID-TIMS. Both mafic cores of the pluton still have no geochronology data reported in the literature. There is an undeformed dioritic dike ~700 m from the western border of the pluton, which intrudes pre-collisional plutonic rocks of the G1 supersuite, as seen in Figure 2.2. The mineralogy of the dike includes mainly biotite, quartz, plagioclase, and opaque minerals as well as accessory minerals zircon, apatite and sericite. This dike was recently studied by Santiago et al. (2020), who performed U-Pb Laser ablation inductively coupled plasma mass spectrometry (LA-ICP-MS) analysis on zircon and obtained a 504.4 ± 5.7-Ma age (MSWD 1.02). This age suggests a cogenetic origin for the dike and the Santa Angélica Pluton itself.

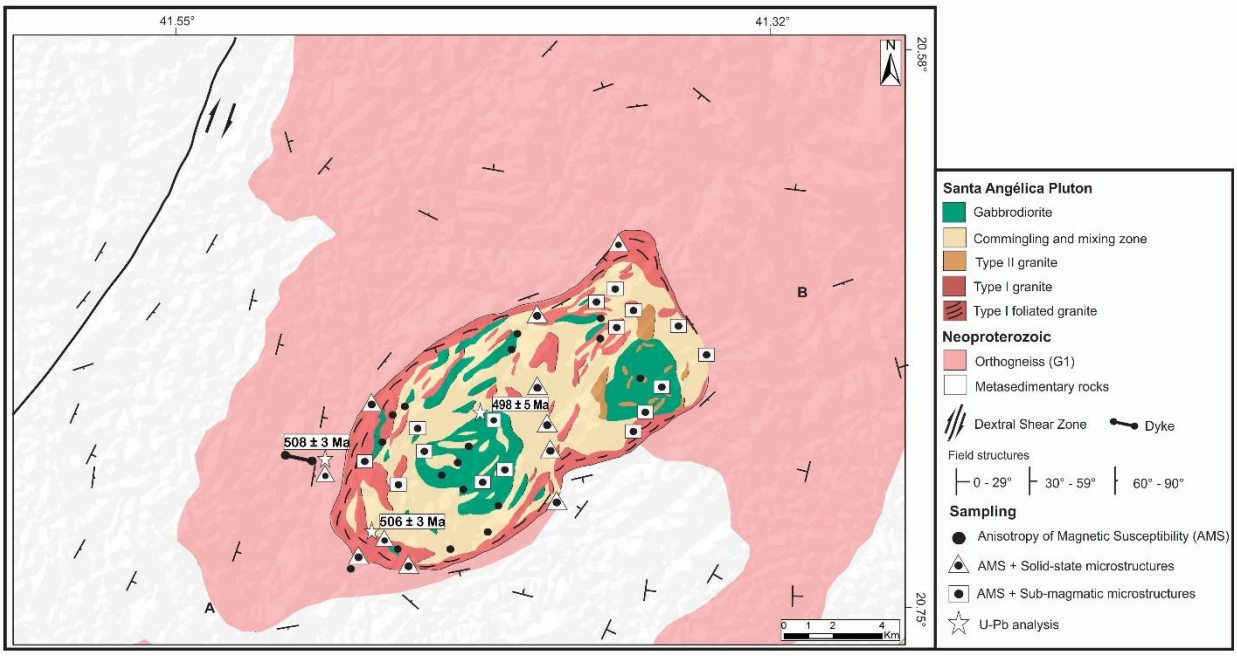

Figure 2.2. Geological map with the shape and facies distribution from Santa Angélica pluton and the country rocks (modified from Schmidt-Thomi and Weber-Diefenbach 1987). Field structures and AMS sampling sites with the type of microstructure and U-Pb analysis are also represented.

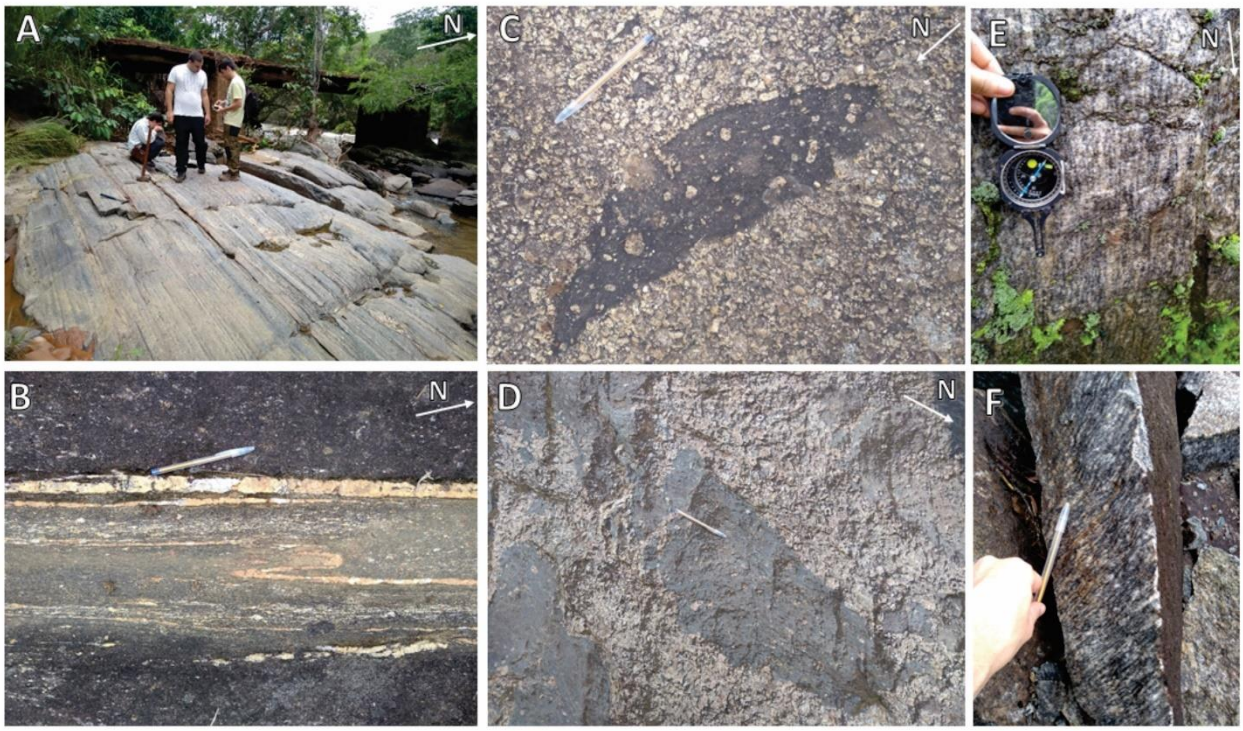

Figure 2.3. Pictures of the Guaçuí Shear Zone and Santa Angélica pluton. (A) and (B) show the vertical foliation from Guaçuí Shear Zone and a dextral shear fold both structures have approximate orientation N30E; (C) and (D) show the mingling texture from the Santa Angélica pluton; (E) and (F) show the well-developed mylonitic foliation well marked in all the border of the Santa Angélica pluton.

2.3 Microstructures

Deformation microstructures were combined with observations of outcrop and hand samples to infer the deformation mechanisms at each studied site. Microscopic features allow us to distinguish magmatic, submagmatic, and solid-state deformation microstructures using widely used criteria (Bouchez et al., 1981; Leblanc et al., 1994; Paterson et al., 1989, among others). This distinction was made throughout the pluton and allowed to distinguish that the solid-state deformation features that are predominant on the pluton edges and on the NW-SE shear zone that divides the lobes, while submagmatic deformation features are scattered throughout the interior of the bodies (Figure 2.2).

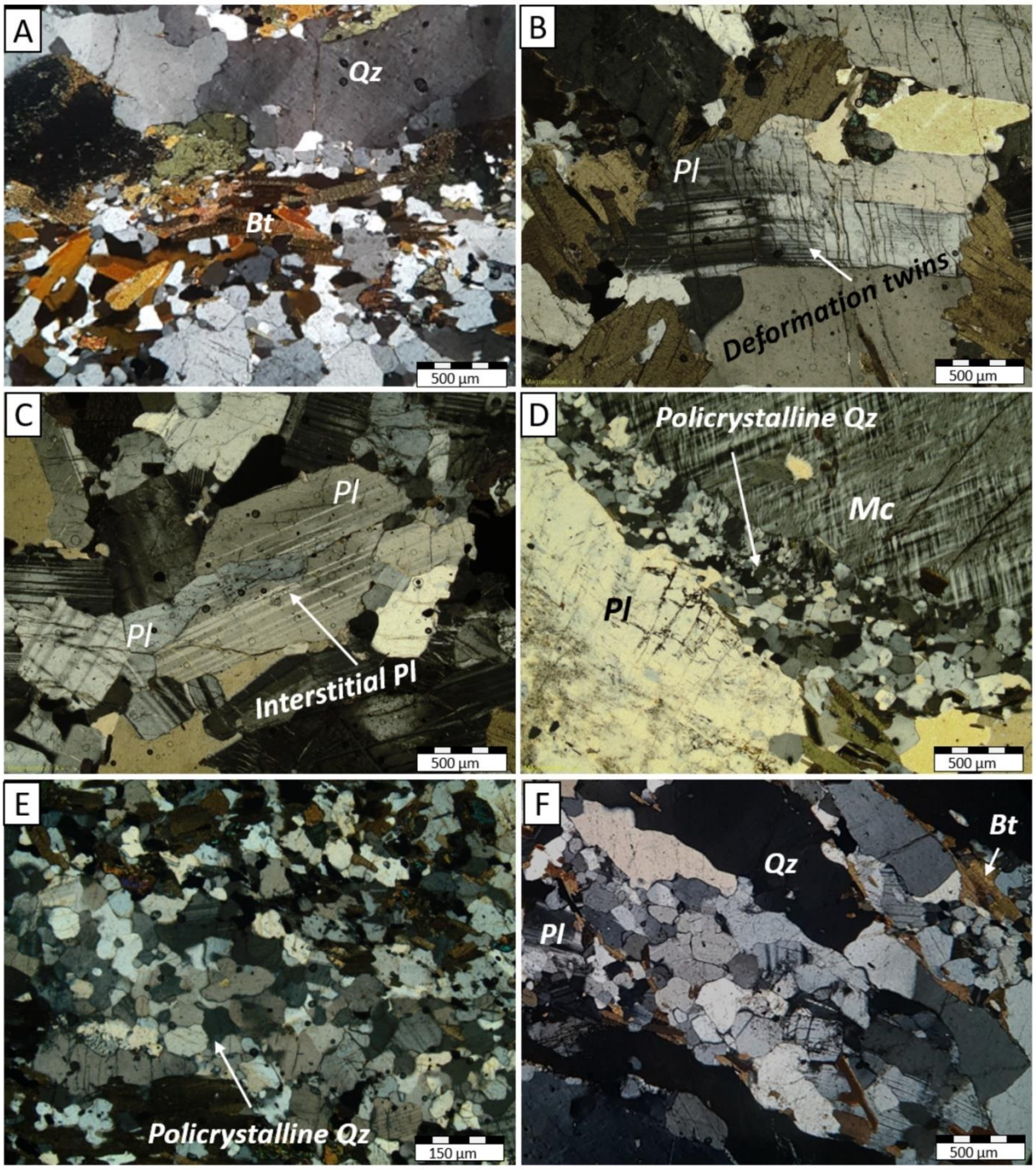

Figure 2.4. Images of microstructures of the Santa Angélica pluton: (a) undulose extinction in quartz (b) deformed twins in plagioclase (c) micro-fractures and embayments in deformed feldspars filled by a fine-grained mosaic of quartz and/or plagioclase (d) Quartz recrystallized with aggregates of relatively small new grains between large old grains with undulose extinction (e) polycrystalline quartz with irregular grain boundaries formed in response to grain boundary migration recrystallization (f)lattice-preferred orientation by the predominance of biotite grains and quartz aggregates elongated like ribbon-shaped, both with the same orientation.

The submagmatic deformation features are mainly observed within the central portions of the lobes (Figure 2.2), where igneous features such as euhedral crystals and magmatic zoning are well preserved. Limited intracrystalline plasticity is suggested by undulose extinction in quartz (Figure 2.4a) and deformed twins in some plagioclase (Figure 2.4b), but relatively small amounts of solid-state strain is recorded by such features. Other submagmatic features include microfractures and embayments in deformed feldspars, which are filled by a fine-grained mosaic of quartz and/or plagioclase (Figure 2.4c), evidence of quartz-feldspathic residual melt. The intracrystalline deformation and presence of melt in the matrix is diagnostic of a solidifying crystal mush undergoing deformation.

Solid-state deformation features are mostly observed along pluton borders and in the internal shear zone that separates the two lobes of the pluton. Solid-state deformation is inferred from different observations: (i) quartz in the matrix is recrystallized with aggregates of small neoblasts at the contact between large, relict quartz grains with undulose extinction (Figure 2.4d). (ii) Polycrystalline quartz with irregular grain boundaries formed in response to grain boundary migration recrystallization (Figure 2.4e). (iii) LPO by the predominance of biotite grains and quartz aggregates elongated like ribbon-shaped, both with the same orientation (Figure 2.4f).

3 Magnetic anisotropy

3.1 Sampling and measurements

Oriented samples were extracted from 43 sites spaced at 1-2 km, evenly distributed across the pluton (Fig. 2.2) excepting some smaller areas of difficult access. Between five and seven cores of approximately 8 cm in length and 2.5 cm in diameter were collected at each site using a portable gasoline powered drill. The cores were oriented in situ with both magnetic and solar compasses. In the laboratory each core was cut into standard specimens that were 2.2 cm in length providing a total of 759 specimens. All measurements were carried out in the Laboratório de Paleomagnetismo at the Universidade de São Paulo (USPmag).

The anisotropy of magnetic susceptibility (AMS) of individual samples was measured using an Agico Kappabridge MFK 1A. The AMS is second-rank symmetrical tensor, but it is commonly represented as an ellipsoid with three orthogonal axes (k1>k2>k3). P is defined as the degree of anisotropy, P=k1/k3 with P = 1 corresponding to a fully isotropic sample (0% anisotropy). T is defined as the shape factor, T=2ln(k2/k3)/ln (k1/k3)−1, reflecting the shape

of the AMS ellipsoid and varying from −1 for prolate, purely linear magnetic fabric (i.e. k1>>k2=k3) through 0 (neutral) to +1 for oblate, purely planar magnetic fabric (i.e. k1=k2>>k3). Statistical evaluation of the magnetic anisotropy in individual sites was obtained using the methods of Jelínek (1978), implemented in the ANISOFT program package (Hrouda et al., 1990). Each station is characterized by the mean anisotropy parameters of a minimum of five specimens (Table 2.1). The AMS directional data from individual sites were filtered to eliminate sites with high internal dispersion (ε12, ε 23), removing sites with uncertainty estimates >26.5° (Jelínek, 1978). Very few data were excluded by this filtering process, with 98% and 95% magnetic lineations and foliations, respectively, showing low dispersion at the site level.

Site (n)	N	Location		Scalar data			Direction of principal axes					
		Geographical coordinates		K_m (10^{-3}SI)	P	T	k_1	ε_{12} (k_1)	k_2	ε_{23} (k_2)	k_3	ε_{31} (k_3)
Gabrodiorite												
SA23	20	41° 26’ 54.866’’	20° 41’ 57.902’’	98.2	1.355	0.210	67/ 27	8/2.8	158/2	8/3.9	252/63	4.1/2.8
SA40	25	41° 25’ 59.143’’	20° 42’ 6.591’’	28.9	1.102	0.172	31/9	12.1/3.1	293/39	11.6/3.6	132/49	6.4/3.9
SA41	12	41° 25’ 47.821’’	20° 42’ 7.206’’	89.1	1.175	0.490	327/30	15.1/2.8	230/12	15.2/3.1	121/57	5.2/2.0
SA42	18	41° 26’ 32.991’’	20° 41’ 40.204’’	112.5	1.230	0.666	173/3	13.3/2.7	82/6	13.2/2.1	292/83	3.3/2.1
SA43	21	41° 25’ 47.953’’	20° 40’ 37.939’’	61.4	1.266	0.252	17/6	9.4/1.7	107/3	9.7/2.5	221/83	3.6/1.8
SA44	16	20° 40’ 22.646’’	20° 40’ 22.646’’	42.1	1.261	0.426	48/8	7.1/4.6	146/45	6.9/3.3	310/43	5.2/2.8
SA45	15	41° 27’ 28.499’’	20° 40’ 52.669’’	102.7	1.464	0.774	144/16	2.1/5.2	236/5	20.6/3.1	341/73	7.5/2.2
SA49	16	41° 21’ 52.343’’	20° 39’ 55.802’’	82.0	1.277	0.866	309/44	18.4/7.5	211/8	18/7.1	113/44	10.4/4.2
SA61	14	41° 25’ 18.916’’	20° 39’ 5.051’’	36.9	1.201	0.047	66/55	8.3/7.6	171/10	10.0/5.6	268/33	9.3/6.8
Mingling zone												
SA26	19	41° 26’ 17.640’	20° 41’ 17.796’’	52.3	1.419	0.721	50/6	16.6/2.4	319/3	16.5/5.8	204/83	6.0/3.5
SA28	16	41° 24’ 30.068’’	20° 40’ 44.949’’	56.1	1.340	0.399	68/41	19/7	159/1	20/85	250/49	14.5/10.4
SA29	12	41° 24’ 25.520’’	20° 41’ 18.496’’	47.2	1.759	0.111	7/40	14.6/2.6	100/3	14.7/1.9	195/50	7.5/2.1
SA31	21	41° 28’ 14.073’’	20° 43’ 24.733’’	68.3	2.049	-0.427	51/85	2.6/2	315/1	7.5/2.6	225/5	7.5/2.1
SA36	18	41° 25’ 51.291’’	20° 43’ 15.260’’	46.0	1.245	0.384	315/46	9.9/5	222/3	11.3/2.8	130/44	6.7/5.4
SA37	10	41° 25’ 37.141’’	20° 42’ 39.409’’	30.7	1.263	0.102	187/60	4.3/4	334/25	4.3/3.3	71/14	4.4/2.7

SA54	18	41° 22’ 31.193’’	20° 38’ 10.851’’	42.5	1.553	-0.213	94/77	1.9/0.9	299/12	3.7/1.8	208/5	3.7/1.1
SA55	12	41° 23’ 8.249’’	20° 38’ 19.800’’	39.1	1.274	-0.282	91/79	4.1/2.0	248/10	13.4/2.7	339/4	13.1/2.0
SA56	9	41° 23’ 2.494’’	20° 38’ 38.344’’	42.6	1.260	-0.149	111/67	15.4/6.8	205/1	13.9/9.4	295/23	14.4/9.2
SA57	16	41° 22’ 54.691’’	20° 38’ 33.998’’	37.3	1.291	0.044	133/65	9.0/6.4	230/3	11.1/8.0	321/25	10.5/6.7
SA58	13	41° 23’ 22.968’’	20° 38’ 0.384’’	76.6	1.746	-0.243	135/57	7.9/2.6	274/26	9.0/4.0	14/18	9.2/2.6
SA59	15	41° 24’ 43.889’’	20° 38’ 18.665’’	2.2	1.249	-0.008	54/34	5.2/1.8	169/32	3.2/2.1	290/39	5.0/2.4
SA66	16	41° 22’ 53.633’’	20° 37’ 39.366’’	3.1	1.306	-0.711	123/61	13.7/3.4	228/8	42.0/5.8	322/27	42.4/5.2
Granite												
SA24	20	41° 27’ 54.268’’	20° 42’ 9.602’’	25.8	1.568	-0.701	103/46	6.1/4.1	256/41	18.4/4.1	358/14	18.4/6.0
SA25	25	41° 27’ 19.640’’	20° 41’ 23.839’’	7.1	1.189	0.753	90/47	29.9/5.0	191/11	29.7/6.3	291/41	8.3/4.6
SA27	22	41° 24’ 21.061’’	20° 42’ 32.806’’	21.2	1.581	0.114	170/79	9.7/3.7	32/8	15.2/6.3	300/7	14.4/5.3
SA32	17	41° 27’ 55.747’’	20° 43’ 38.877’’	47.9	1.794	-0.322	113/72	6.8/4.8	273/17	9.4/6.7	4/6	9.4/4.9
SA33	15	41° 26’ 54.195’’	19° 55’ 15.506’’	56.3	1.414	-0.158	15/68	8.3/4.1	273/5	9.3/4.3	181/21	10/7.3
SA34	9	41° 26’ 42.743’’	20° 43’ 39.204’’	21.0	1.170	0.166	51/22	25/3.3	320/3	24.9/3.3	223/68	5.6/2.4
SA47	17	41° 24’ 43.815’’	20° 39’ 56.775’’	66.3	1.581	-0.049	65/39	10.6/6.5	164/11	6.9/5.6	267/49	10.6/5.3
SA50	9	41° 22’ 22.077’’	20° 39’ 44.341’’	52.5	1.041	0.453	20/82	26.0/9.0	200/7	26.0/8.5	110/0	10.7/7.1
SA51	14	41° 22’ 14.207’’	20° 40’ 31.424’’	16.8	1.040	-0.267	241/11	29.8/22.7	142/40	62.8/27.0	343/48	62.8/21.9
SA52	18	41° 20’ 50.907’’	20° 39’ 11.617’’	12.8	1.650	-0.145	196/90	7.2/4.5	322/0	12.9/4.4	52/0	13.6/5.0
SA53	18	41° 21’ 29.632’’	20° 38’ 31.818’’	12.9	1.466	0.302	203/46	14.3/8.4	313/18	16.3/6.4	59/38	14.2/6.6
SA60	21	41° 25’ 10.870’’	20° 38’ 43.286’’	60.0	1.802	0.104	54/35	7.9/3.0	197/49	7.8/3.0	310/19	9.1/3.0

SA62	9	41° 28′ 31.721′′	20° 40′ 19.192′′	10.4	1.858	0.394	125/69	5.0/4.2	27/3	9.4/4.5	295/21	9.7/2.5
SA64	10	41° 28′ 2.715′′	20° 40′ 34.626′′	11.6	1.636	0.197	123/43	5.5/4.7	22/11	5.5/3.5	281/44	6.4/2.6
SA65	10	41° 28′ 16.629′′	20° 41′ 12.622′′	36.7	1.602	-0.498	159/59	4.6/3.2	395/30	10.1/3.2	257/5	9.5/3.2
Foliated granite												
SA22	10	41° 28′ 59.671′′	20° 44′ 6.497′′	106.1	1.076	0.756	160/74	40.3/7.0	307/13	40.1/6.5	39/8	9.9/4.2
SA30	13	41° 28′ 49.131′′	20° 43′ 51.599′′	4.6	1.214	-0.289	140/83	6.5/3.8	335/6	8.3/4.8	245/2	7.9/5.1
SA38	10	41° 26′ 25.051′′	20° 42′ 17.245′′	77.0	1.155	-0.364	43/43	12/4.0	258/41	17/5.0	151/18	14.1/5
SA46	10	41° 28′ 41.535′′	20° 41′ 38.140′′	9.3	1.347	0.169	53/61	3.2/2.3	173/15	3.4/1.5	270/24	2.4/1.6
SA48	13	41° 22′ 31.978′′	20° 40′ 56.861′′	41.0	1.296	-0.058	82/75	7/5.0	273/15	11.7/6.3	182/3	11.7/4.8
SA67	6	41° 22′ 51.762′′	20° 36′ 39.056′′	16.9	1.716	-0.332	160/77	10.7/2.6	289/8	9.7/5.1	20.0/10	8.3/4.3
Dike												
SA68	6	41° 29′ 35.71′′	20° 41′ 36,48′′	0.0697	1.170	0,675	64/69	13.6/3.5	165/4.3	4.7/3.0	257/20	5.5/1.4

Table 2.1. Anisotropy of magnetic susceptibility parameters of the Santa Angélica pluton. Site number; number of specimens measured (N); longitude, latitude – geographical coordinates; Km = mean magnetic susceptibility (10^{-3}SI); P = degree of anisotropy of the magnetic susceptibility ($P=k_1/k_3$);T= AMS ellipsoid shape parameter [$T=2\ln(k_2/k_3) / \ln(k_1/k_3)-1$]; K_1=trend and plunge of magnetic lineation (in degrees); K_2=trend and plunge of the intermediate anisotropy axis; K_3=trend and plunge of the pole of the magnetic foliation; ε_{12}, ε_{23}, ε_{31} are the semi-angle (measured in degrees) of confidence ellipses of AMS axes from Jelínek's (1978) statistics.

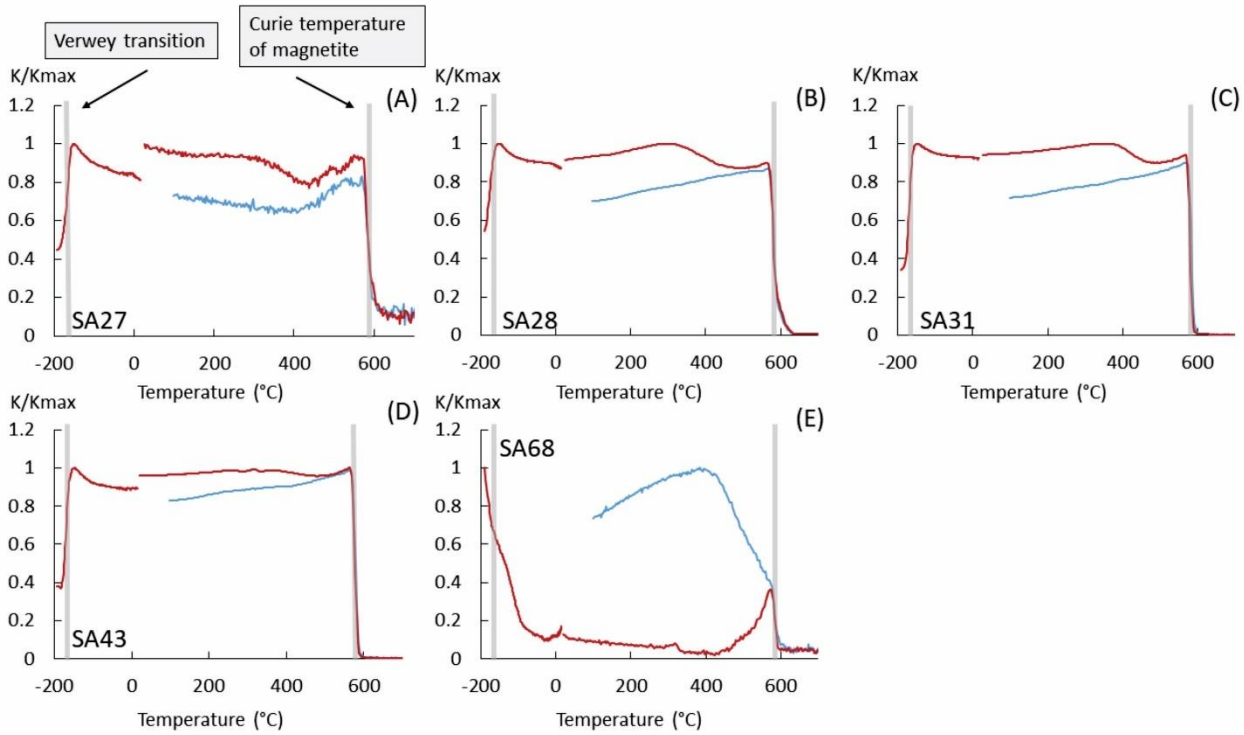

Figure 2.5. Representative thermomagnetic curves for five samples of the Santa Angélica pluton. The y-axis is the bulk of magnetic susceptibility and the x-axis is the temperature in degrees Celsius. The red lines represent the heating and blue lines represent the cooling.

We investigated the contribution of specific minerals to the bulk rock magnetic susceptibility in order to better understand the results of the AMS measurements. Thermomagnetic experiments were acquired under argon flux to prevent excessive oxidation during heating using a CS-2 furnace attached to an Agico Kappabridge KLY 4 CS (Figure 2.5). All thermomagnetic K-T curves (susceptibility K as function of temperature T) were performed at a temperature interval from -200 to 700°C. Isothermal remanent magnetisation (IRM) curves, hysteresis curves and first order reversal curves (FORC) were obtained with a vibrating sample magnetometer (VSM) MicroMag 3900 (Princeton Measurements Corp) (Figure 2.6).

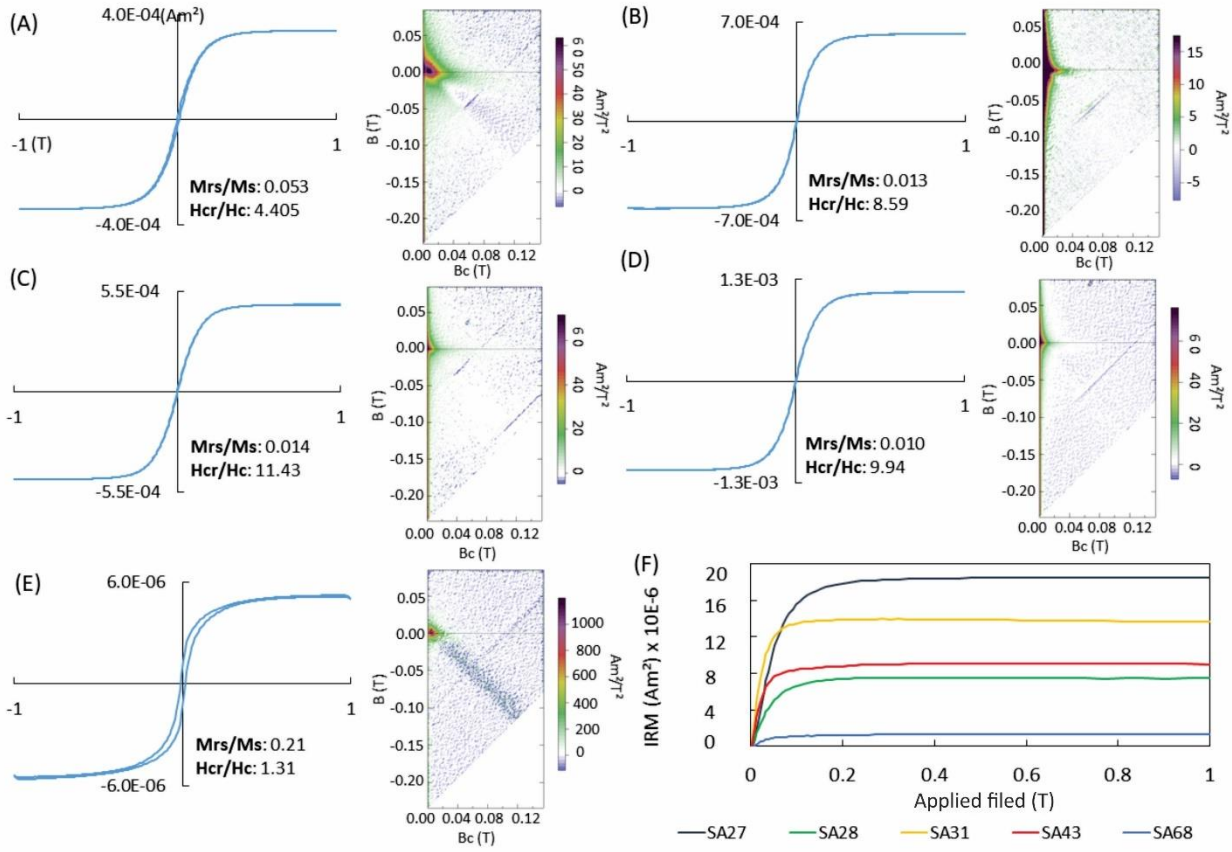

Figure 2.6. Hysteresis and FORC diagram for five samples which represents all the lithotypes present in the Santa Angélica pluton (A) SA27 (B) SA28; (C) SA31; (D)SA43; (E) SA68; (F) IRM acquisition curves for these five samples.

Measurement of the anisotropy of anhysteretic remanence magnetization (AARM) was carried out on samples from five sites, selected to represent all rock types and structural domains within the Santa Angelica pluton. The measured AARM fabric reflects the pure contribution of ferromagnetic phases to the magnetic fabric of the rock (Jackson, 1991), in contrast with the more commonly measured AMS, which reflects the summed contributions of diamagnetic, paramagnetic, and ferromagnetic mineral phases. AF demagnetization and anhysteretic remanence acquisition were achieved with a LDA-3 (AGICO) demagnetizer/magnetizer, and remanence was measured with a JR6-A magnetometer (AGICO), both kept in the magnetic field-free room of USPmag. Before AARM measurements samples were AF demagnetized at a peak AF field of 100 mT. The magnitude and orientation of the principal axes of the AARM ellipsoid were determined for each specimen after anhysteretic remanence acquisition along fifteen different orientations with a peak field of 50 mT and a biasing field of 100 μT following the procedure described in Trindade et al. (2001).

3.2 Anisotropy of magnetic susceptibility (AMS)

Both degree of anisotropy (P) and the shape of the ellipsoid (T) vary according to rock lithology (Table 2.1). For gabbroic to dioritic compositions, P ranges from 1.102 to 1.464, and all ellipsoids are oblate in shape. The mixing zone has the highest values of P, ranging from 1.245 to 2.049, with prolate ellipsoids slightly more abundant than the oblates. For more felsic compositions, P values range from 1.040 to 1.885, and the oblate rock fabrics are slightly more abundant than the prolate variety. Foliated granites from near the country rock contact have P values ranging from 1.076 to 1.716, with mostly prolate magnetic fabrics. Finally, the dike has a P value of 1.170 and essentially oblate fabrics.

We plot all magnetic foliation and lineation data that remain after eliminating sites with low internal coherence (Fig. 2.7). Magnetic foliations and lineations of all lithotypes show a clear concentric pattern around each of the two mafic nodes. The macroscopic foliation recognized closer to the contact boundaries is observed as a magnetic foliation that contours the pluton boundaries. This foliation dips steeply (Figure 2.7 C), and magnetic lineations are also steeply plunging. There is an internal shear zone separating the two mafic cores, dividing the pluton into a northeastern and southwestern lobe (Fig. 2.7). This shear zone geometry is well-resolved by parallel AMS fabrics at all sites along the NNW-SSE oriented structure. Magnetic foliation strikes NNW-SSE with steep dips, and magnetic lineations have high rakes, consistent with the NE vergence. In all petrographic facies, the northeast lobe presents near-vertical magnetic lineations (Figure 2.7 D), while the southwest lobe presents magnetic lineations with low-angle (Figure 2.7 E).

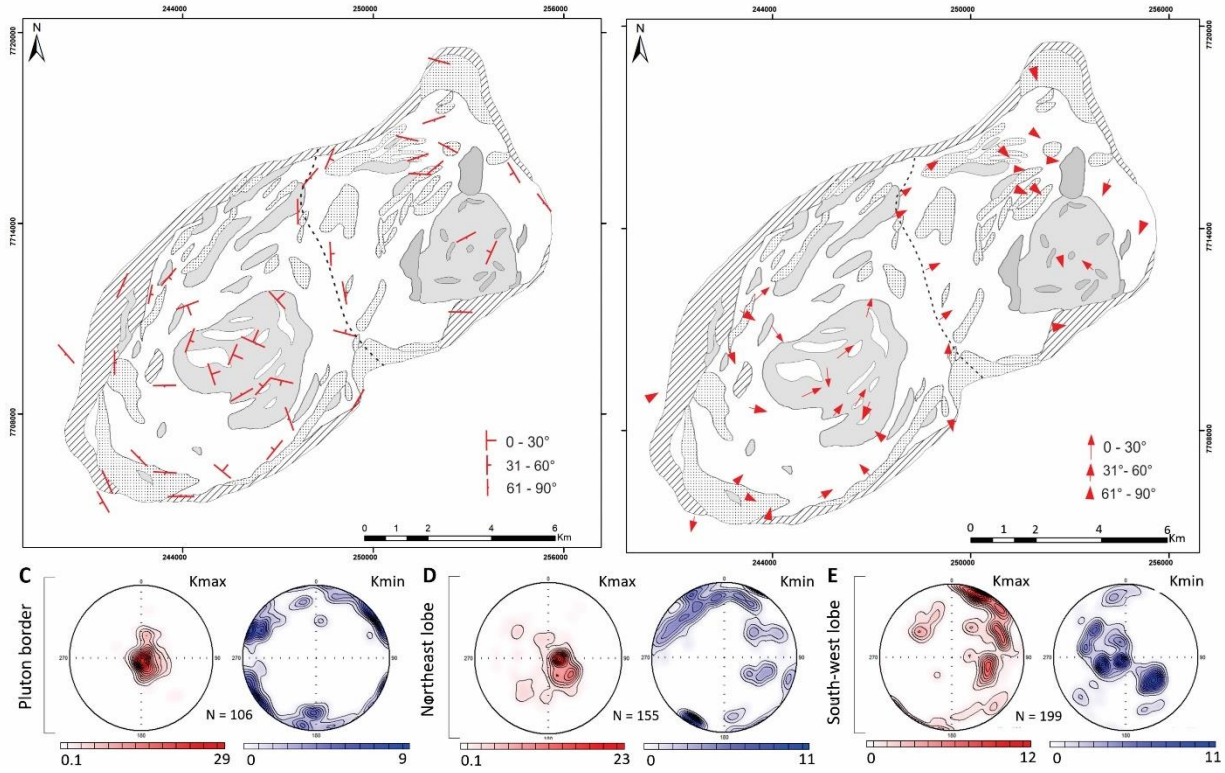

Figure 2.7. AMS directional data after elimination of scattered sites (for error ellipses above 26°). (A) Magnetic foliations (K_3); (B) Magnetic lineations (K_1); Contour plot of Kmax and Kmin on the border (C), northeast lobe (D) and southwest lobe (E) of the pluton.

3.3 Magnetic mineralogy

Magnetic susceptibility vs temperature (k-T) curves were analyzed for one sample from each lithology of the Santa Angélica pluton in order to identify the ferromagnetic minerals. Specimens with moderate to high magnetic susceptibilities show similar, simple behaviors during cooling and heating, with steep drops at temperatures below -153°C and above 580°C (Fig. 2.5 A-D), coincident with the Verwey transition and the Curie temperature of magnetite, respectively. The sample SA68 taken from the dike displays Verwey transitions that are poorly defined, and the decrease in magnetic susceptibility at higher temperatures indicates the dominant contribution of paramagnetic phases for this sample (Fig. 2.5 E). The increase of the magnetic susceptibility around 450°C and its subsequent abrupt decay at 580°C indicates that some new magnetic phases were formed in the heating cycle.

Figure 2.6 shows hysteresis loops, FORC diagrams (Figure 2.6 A-E) and IRM (Figure 2.6 F). Low values of coercivity can be seen in the hysteresis curves. This fact is also supported by the values of Mrs/Ms and Hcr/Hc, which are typical of multi-domain (MD) magnetite

according to Day et al. (1977) and Dunlop (2002). By the qualitative analysis in the FORC diagrams (Figure 2.6 A-D), the distribution is also typical of MD magnetite (Roberts et al., 2000). The dike (Figure 2.6 E) has a distribution less concentrated on the B (T) axis and higher Bc (T) than the samples from inside the pluton, in addition to Mrs/Ms and Hcr/Hc values which are typical of pseudo single domain (PSD) or vortex-state magnetite grains (Roberts et al., 2000).

3.4 Anisotropy of anhysteretic remanence magnetization (AARM)

The AARM reflects the sole contribution of ferromagnetic phases (Jackson, 1991), because paramagnetic minerals are incapable of retaining a remanent magnetization. In order to further restrict the selection of fabric carriers, we obtained the AARM within a coercivity window between 0 and 50 mT, in accordance with the coercivity range of coarse-grained magnetite (Jackson et al., 1988, Trindade et al., 2001).

Figure 2.8 shows the AMS and AARM results for five sampling sites, distributed in all lithotypes of the Santa Angélica pluton. The AMS and AARM magnetic fabric are very similar for all lithotypes, thus attesting the dominant role of the multi-domain magnetite in the definition of the magnetic fabric in these rocks. This indicates that the dispersion in the AMS fabric of these sites is not related to the influence of other magnetic phases, but mainly reflects the dispersion in the orientation of the MD magnetite grains in the rock.

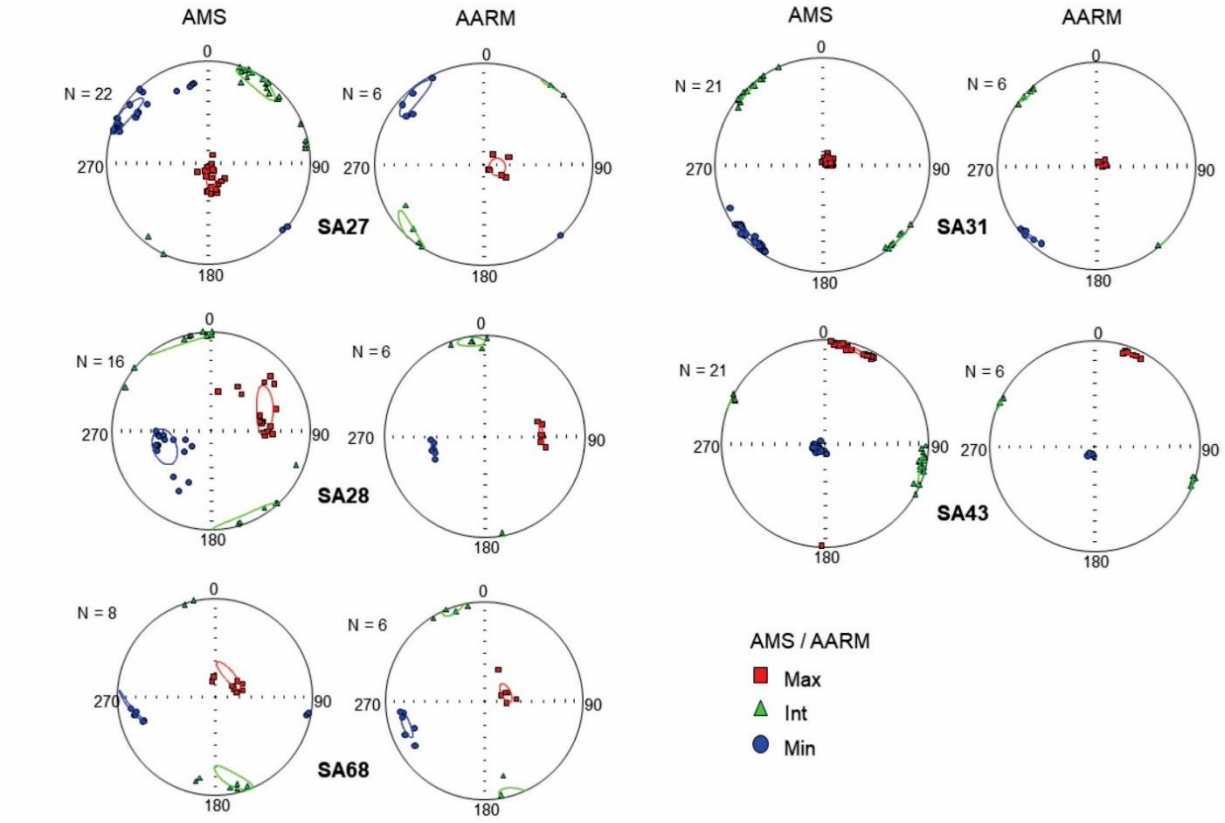

Figure 2.8. Comparison of AARM and AMS directions for sites SA27, SA28, SA31, SA43 and SA68. While AMS is related to the bulk magnetic response of all minerals, the AARM is exclusively controlled by the shape of magnetite. Agreement between AARM and AMS fabrics suggests a magnetic fabric controlled by large, multi-domain magnetite.

4 Geochronology

4.1 Sampling and methods

Three new U-Pb ages of zircon were determined for this study. Two samples were collected inside the pluton (border and core) and a third sample was obtained from the dike in the country rock located 700 m from the western border of the pluton (Fig. 2.2). Sample SA31 is a foliated granite taken from near the southern border of the pluton. Sample SA43 is a gabbro taken from the southwestern node of the pluton. SA68 is a dioritic dike.

The separation of the zircons was carried out at the Centro de Pesquisas em Geocronologia e Geoquímica Isotópica (CPGeo) at the Universidade de São Paulo. The samples were cleaned of weathered material, jaw crushed, milled and sieved. The zircon fractions were concentrated using gravity separation on a Wilfley table. Magnetic material was removed from the dense fraction using a hand magnet and subsequently using a Frantz magnetic separator at 0.5 A and

1.5 A. The residual non-magnetic fraction was then passed through bromoform and methyl iodide solutions to separate the denser minerals. Zircons were then hand-picked from the non-magnetic, highest density aliquot using a binocular microscope. The zircon grains were finally mounted into epoxy resin discs of 2.5 cm diameter that were sanded and polished, exposing a cross section of each zircon grain at the surface of the disc. Morphology and texture of the polished zircons were imaged using transmitted and reflected light and cathodoluminescence (CL) techniques (see in appendix A). The U–Pb analyses were carried out on the Sensitive High Resoution Ion Microprobe (SHRIMP-II) installed at CPGeo.

4.2 Results

Cathodoluminescence (CL) images of the zircons and sample spots are shown together with U-Pb analysis data in the appendix A. Discordant data were eliminated from the age calculation.

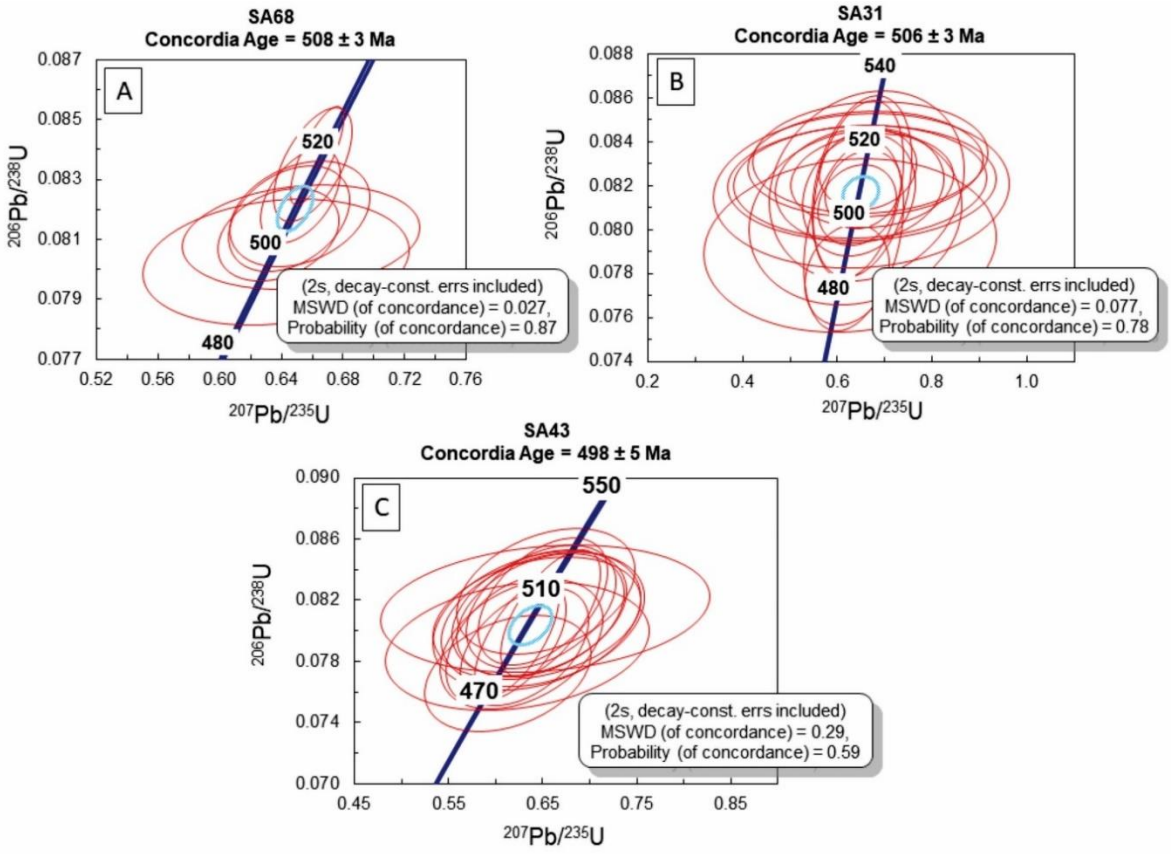

Figure 2.9. Concordia diagrams of samples SA68 (dioritic dyke), SA31 (granite) and SA43 (gabbro) with zircon U-Pb ages determined by average of the concordant data. Data-point error ellipses are 2σ. SA68 represents a dike which is located 700 m away from the western border of the pluton and intrudes the pre to sin-orogenic granitoids. SA31 represents the foliated granite from the border of the pluton. SA43 represents the gabbroic core from the southwest lobe.

Two samples were collected from the different lithologies of the Santa Angelica pluton. In sample SA31 (granite) zircon grains are euhedral to subhedral with few fractures. A weakly-developed zoning is observed under cathodoluminescence, with light rims with and few dark cores. Eighteen spots were analyzed in different zircon grains. All analyses are concordant, and we calculated a weighted mean 206Pb/238U age of 506 ± 3 Ma (MSWD = 0.077, 2-sigma) (Fig. 2.9 B). Zircons from sample SA43 (gabbro) are generally subhedral, with some well-preserved prismatic faces. The CL images show weak internal zoning. Eighteen spots were analyzed on different zircon grains. Most analyses are concordant and a weighted mean 206Pb/238U age of 498 ± 5 Ma (MSWD = 0.29) was obtained on the concordia diagram (Fig. 2.9 C). Two analyses were discordant (#16.1, 545 ± 11 Ma and #17.1, 556 ± 10 Ma), probably inherited zircons from the pre-collisional plutonic country rocks.

A third sample (SA68) was collected from the dioritic dyke outside the pluton. Zircon grains separated from this sample are anhedral in form, with many fractures present. The CL images show moderate zoning with few light rims in some zircons. Eighteen spot analyses were carried out on different zircons, of which eight analyses yielded concordant results. A weighted mean 206Pb/238U age of 508 ± 3 Ma (MSWD = 0.027) was obtained on the concordia diagram (Fig. 2.9 A). Ten analyses were discordant with ages ranging from 542 ± 4 Ma (#5.1) to 481 ± 6 Ma (#3.1).

5 Discussion

5.1 Significance of magnetic fabric

The magnetic fabric of the Santa Angélica pluton is controlled by coarse-grained, multi-domain magnetite. The presence of magnetite is clear from the susceptibility versus temperature (k-T) diagrams (Figure 2.5). The geometry of the bulk magnetic fabric (AMS) is confirmed by AARM measurements with both techniques yielding very similar orientations of principal axes for all the analyzed samples (Figure 2.8). The AARM ellipsoids were obtained on a low-coercivity window of 0 to 50 mT, being therefore defined only by the coarse-grained multidomain magnetite grains (Trindade et al., 2001).

Microstructural analysis confirms the predominance of solid-state deformation features along the entire border of the pluton. Solid-state deformation is also observed within the pluton along the shear zone that divides the northeast and southwest lobes. The strong fabrics created by solid-state deformation presents correspondingly high values of P (up to 1.7) and a prolate

fabric consistent with the development of a well-defined stretching lineation. In the shear zone, all sites have magnetic lineations with northeast-bearing lineation. High dip angles of magnetic lineation are found in both regions.

Magnetic foliations and lineations of all lithotypes inside the pluton show a clear map view pattern of concentric structures centered on the gabbrodioritic cores (Fig. 2.7). These two lobes are separated by the NW-SE shear zone, which is clearly visible in the AMS data from the contact region between the two lobes. In the inner part of the pluton (core and mingling zone) only sub-magmatic deformation was observed. The AMS patterns reflect deformation recorded by magmas during their emplacement and crystallization, whereas the inner part of the pluton (core and mingling zone) only submagmatic deformation was observed. The magmatic mingling zone is generally marked by planar fabric with high values of P (up to 2.04). Both mafic cores present similar AMS patterns, with high values of P (up to 1.4) and planar fabric.

The different lobes can be distinguished on the basis of their magnetic lineations (Fig. 2.7), with the northeastern lobe marked by steeply-plunging lineations (61-90°). Magnetic lineations in the southwest lobe plunge at much more shallow angles (0-29°). Vertical lineations (> 60°) may indicate the presence of a magma feeder zone where differentiated, late-magmatic granite subtypes are also found (Bouchez ans Stephens, 1997). If true, this observation suggests that the northeastern lobe is fed more directly by deeper sourced material than the southwestern lobe.

Although previous works (Bayer et al., 1987; Schmidt-Thomé and Weber-Diefenbach, 1987; De Campos, et al. 2004; Pedrosa-Soares et al., 2011) have reported an isotropic or low anisotropic pattern inside the Santa Angélica pluton, the new AMS data shows a strongly anisotropic pattern corroborated by the evidence of both sub-magmatic and solid-state type fabrics (Fig. 2.2). The good agreement between magnetic and petrofabric geometries have been demonstrated by comparison of AMS and thin-section image analysis data (Fig. 2.2), confirming the utility of AMS in detecting cryptic structures in plutonic rocks. Syntectonic plutons are characterized by coherent, unidirectional magnetic lineations at the pluton scale (e.g., Bouchez et al., 1990; Archanjo et al., 2002, Langille et al., 2014). In contrast, the Santa Angélica pluton shows a well-defined concentric pattern of magnetic lineations suggesting that magma deformation was controlled by magma buoyancy forces (Sant'Ovaia et al., 2000; Oliveira et al., 2010). In addition, in contrast to previous Santa Angélica pluton emplacement models (Bayer et al., 1987; Schmidt-Thomé and Weber-Diefenbach, 1987, Zanon et al., 2015)

that show it as a single pluton generated in a post-collisional environment, our new AMS data makes it possible to distinguish two partly overlapping intrusions that form the Santa Angelica pluton. This new information sets precedents for new interpretations regarding the emplacement of the body.

5.2 Geochronology

Two samples were dated by U-Pb systematics on zircons of the Santa Angélica pluton: from the border of the pluton (SA31, foliated granite) with weighted mean 206Pb/238U age of 506 ± 3 Ma (MSWD = 0.077) and from its mafic core (SA43, gabbro) with weighted mean 206Pb/238U age of 498 ± 5 Ma (MSWD = 0.29). We note that the geochronological results obtained for the sample SA43 are the first reported ages for the mafic core of the Santa Angélica pluton. We interpret these ages to reflect the age of pluton formation and crystallization. Overlapping analytical errors notwithstanding, the border of the pluton seems to have crystallized before the core, which would have been thermally buffered from the colder contact zone and would have stayed hotter for longer. The age of the granite sample SA31 is consistent with the ages obtained by Sollner et al. (1991), but our new age determination has greater accuracy. Other ages of post-collision plutons found in the southern segment of the AO were published and compiled by De Campos et al. (2016). These ages were calculated with few zircons and all using ID-TIMS: Varzea Alegre pluton 489 ± 5 Ma (zircon, n = 5); Mimoso do Sul pluton 498 ± 5 Ma (zircon, n = 5); Montanha pluton 500 ± 2 Ma (zircon, n = 4); Cotaché pluton 503 ± 3 Ma (zircon, n = 7). The larger number of zircon grains that form the basis of our age determinations (eighteen zircons each), demonstrate a robust geochronological correlation of the Santa Angelica and other post-collisional plutons in the region.

A dioritic dike located 700 m from the eastern border of the pluton, is observed to intrude pre-collision Ediacaran plutonic rocks. Zircons from this dyke yielded a weighted mean 206Pb/238U age of 508 ± 3 Ma (MSWD = 0.027). The age of the SA68 sample is in agreement with the ages obtained by Santiago et al. (2019), but again with greater analytical accuracy, probably due the more robust technique used here. The contemporaneous age of the dike and the Santa Angelica pluton and the similar dioritic compositions of both suggested that the two bodies are co-genetic.

5.3 Model of emplacement

Major lineaments such as deep fault zones provide a preferred avenue for the emplacement of magmas in the crust (e.g., Pitcher 1979; Grocott et al., 2009; Seymour et al., 2020). The Coastal Batholith of Peru (Pitcher & Bussell 1977) provides an example of the dominant role exerted by deep-seated structures on the locus magmatic ascent, versus the trivial role played by overburden geology. The final emplacement mechanisms of granitic magmas within the upper crust reflects a combination of factors (Pitcher 1977; Paterson and Schmidt, 1999; Chernicoff et al., 2002; Spacapan et al., 2016). The deep-seated crustal lineaments of the AO exerted a similar control on the locus of magmatic intrusion (Meneses and Paradella, 1978) with most plutons located within or adjacent to major lineaments (De Campos et al., 2004; Pedrosa-Soares et al., 2011).

Several workers report an integration of geochronology, microstructures (Jhnson et al., 2003, Vernon et al., 2004, Han et al., 2014, Gonçalves, et al., 2019) and AMS data (Sant'Ovaia et al., 2000; Gleizes et al., 2006; Žák et al., 2013) to document magma emplacement and progressive strain accumulation. Our integration of these datasets with U-Pb zircon geochronology provides a clear view of the origin and significance of magmatic and solid-state structures preserved within the Santa Angélica pluton (Fig. 2.4), yielding an integrated view of post-collisional pluton emplacement and deformation on the margins of the AO.

The emplacement of the Santa Angélica pluton corresponds to two partly overlapping intrusions (Fig. 2.10A). According to the previous model of emplacement of the Santa Angélica pluton (Schmidt-Thomi and Weber-Diefenbach, 1987), mafic magma were transferred into the lower crust crystallizing to gabbro during the cooling of the orogen. The emplacement of the Santa Angélica pluton likely remarked an early NE-SW-trending discontinuity (Guaçuí shear zone) parallel to the regional foliation. Basaltic materials generated within the mantle ascend in the form of diapirs in the southern portion of the AO (De Campos et al, 2004). Once in the crust, these magmas induced localized anatexis of crustal rocks and production of granitic magma (Schmidt-Thomi and Weber-Diefenbach, 1987). Structural data reveals border foliations in agreement with those of the country rocks for those plutons (Fig. 2.1B) including Santa Angélica pluton (Fig.2.2; Fig. 2.3E,F), suggesting its forced emplacement character. Geochronological data of the felsic border (506 ± 3 Ma) and the mafic core (498 ± 5 Ma) highlights the contemporaneity of both magmas. Geochemical data from Bayer et al. (1987) document mingling and mixing of mafic and felsic magmas inside the pluton. The mixing texture observed by those authors was generated by several, closely-timed pulses of magmatism. The mingling texture of basic and acidic magmas (Fig. 2.3C,D) reveals that the

feldspar crystals at the interface of coeval magmas of contrasting compositions (e.g. Knesel et al., 1999; Baxter and Feely, 2002; Perugini et al., 2005; Slaby et al., 2008). Bayer et al. (1987) combined petrographic and geochemical data of the Santa Angélica pluton, documenting the ongoing "ripening" of coarse-grained gabbro from fine-grained gabbro. The latter are classified as a more primitive rock with affinities towards alkali or transitional basaltic composition. Rapid consolidation of the magma body prevented complete homogenization of the commingled magmas, thus preserving a frozen-in state of magma mixing (Slaby et al., 2008). The absence of a distinct metamorphic aureole within the country rocks of the the Santa Angélica magma (Bayer et al. (1987) is consistent with a still hot host-rock during magma intrusion.

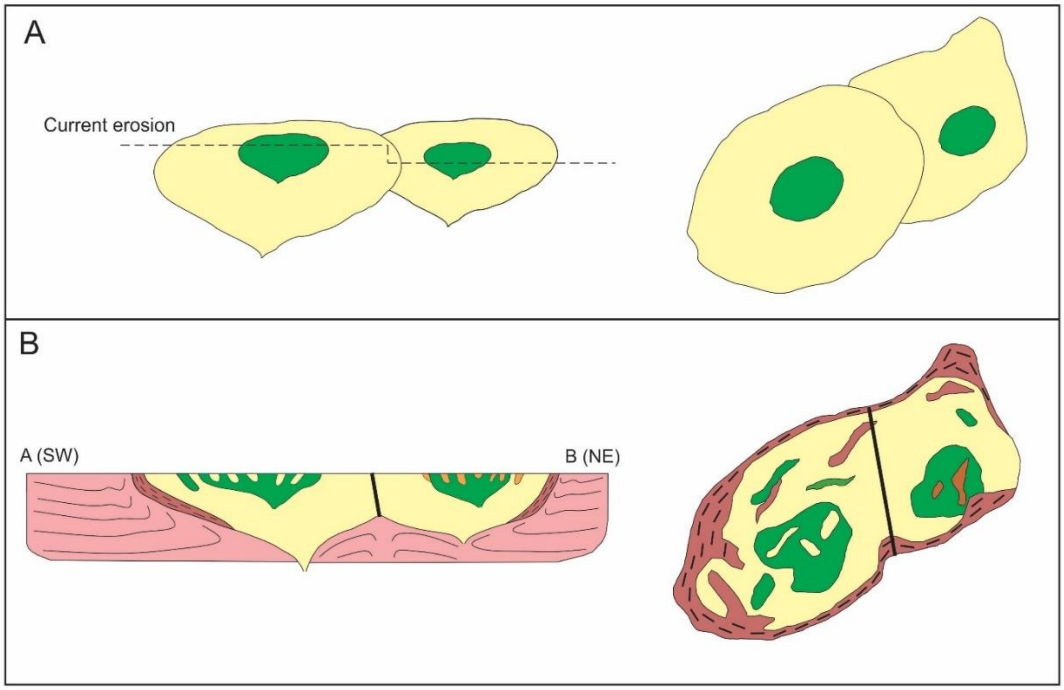

Figure 2.10. Emplacement model for the Santa Angélica pluton (right panel: map view, left panel: vertical sections). (A) Emplacement correspond to that of two partly overlapping intrusions (B) Profile A-B (see in Fig. 2.2) shows the structural relationship of the country rocks with the pluton. At the final stages of body emplacement, upward transport of the northeastern lobe relative to the southwestern lobe was accommodated along a shear zone between the two lobes, generating an internal shear zone.

Profile A-B (see in Fig. 2.2, Fig. 2.10B) shows the schematic structural relationship of the country rocks with the pluton that locally show melt veins along the sub-vertical foliation concordant to the border of the intrusive complex (Fig. 2.3E,F), which dip inwards towards the intrusion (Fig. 2.2). This geometry evidences the vertical rise of the pluton during its emplacement (Fig. 2.10B) with solid-state deformation across the border of the pluton and in

the neighboring country rocks when the granites were largely crystallized in a grain-supported regime indicating the waning presence of magma along the pluton's boundaries (Fig. 2.2). The profile A-B also shows the internal shear zone that affected the pluton, precisely at the contact between both plutons during final stage of the emplacement. This shear zone is characterized by solid-state deformation with a strong magnetic fabric corresponding to high values of P (up to 1.7) and a prolate fabric consistent with the development of a well-defined stretching lineation. All sites at the shear zone have magnetic lineations with a northeast trend and high dip angles. Based on the AMS data (Fig. 2.7D,E), we hypothesize that the two lobes represent different levels of erosion, where the northeast lobe represents the deepest sectors of the intrusion (Fig. 2.10A). Probably, such exposure difference of erosion levels occurred due final stage accommodation of the both plutons. Together, U-Pb and AMS data suggest that magma emplacement was controlled by magma buoyancy forces, (almost) free of tectonic stress.

5.4 Implications for Araçuai belt evolution

Orogens evolve along the T-M (temperature-magnitude) spectrum, and may grow from small-cold orogenies dominated by critical wedge mechanics to large scale hot orogens (Jaimieson and Beaumont, 2013). During the collision phase, the magnitude of the belt and the temperature increase as radioactive crustal material is accreted, buried and heated. In the Araçuaí-West Congo orogen, the high temperatures, slow cooling, and excessive amount of melt in the hinterland require a heat source capable of maintaining a high temperature for a long time, more specifically to keep the temperature above 700°C from 600 to 480 Ma (Fossen et al., 2017).

According to Jaimieson and Beaumont (2013), no material would be added to the orogenic system after convergence ends. In these final stages, orogens will decay by the effects of erosion and gravitational collapse, whereby extension and crustal thinning reduces lithospheric overburden through lateral flow of the hot orogenic interior. In the Araçuaí orogen, this extension phase initiated at 500 Ma. Geochronologic results suggest that the internal domain of the orogen was hot for a long time, cooling at $< 3°$ / Myr until 500 Ma (Petitgirard et al., 2009), and cooling through the Ar/Ar retention temperature for biotite around 470 Ma in both the eastern (Munha et al., 2005) and western (Petitgirard et al., 2009) parts of the hot internal orogenic domain. However, magmatism dominates the main period of orogeny from ca. 630 until ca. 560 Ma, with some form of tectonic activity ongoing until ~480 Ma (Pedrosa-Soares et al., 2011; Tedeschi et al., 2016; Gonçalves et al., 2016).

Figure 2.11. Schematic cross-sectional illustrations of the extensional collapse phase of the Araçuaí orogen at 500 Ma (modified from Fossen et al., 2017). Red and pink drops represent the post-collisional magmatism.

A schematic, N-S profile profile of the Araçuaí orogen (Fig. 2.11) illustrates the extensional collapse phase of the orogen. The plutons of 'I-type' granitoid are larger and more common in the northern portion of the Araçuaí orogen (Pedrosa-Soares et al., 2001, De Campos et al., 2004), which was defined as the hot, internal zone by Vauchez et al. (2007) and Cavalcante et al., (2018). Inside this zone, plutonic rocks contemporary to the Santa Angelica pluton (Petitgirard et al., 2009, Xavier et al. 2017) show completely different structural behavior than that oberved in our study region farther south. Geochronological and AMS studies carried out by Petitgirard et al., (2009) and Xavier et al. (2017) highlight internal structures typical of syn-collisional plutons, with a coherent N-S magnetic foliation, following the general structure of the belt in that sector. The usually weak and mostly magmatic fabrics in those plutons show a variably oriented but mostly low-angle magnetic foliation and gently plunging magnetic lineation oriented ~N-S (orogen-parallel). This pattern is consistent with a combination of gravity-driven deformation in addition to tectonically-driven flow in this part of the AO (Cavalcante et al., 2013, 2014). Such contrasting structural pattern for coeval plutons along strike of the orogen reveals the strain partitioning at the scale of the orogenic belt during the cooling of the AO. At 500 Ma the northern sector remains warm enough to allow a coherent deformation of intrusions and host rocks (Fig. 2.11). At the same time, more material was being added along the colder margins of the orogen, with diapir-like plutons being intruded whose internal structures were dominantly controlled by forces of magma ascent and emplacement.

The long axis of the Santa Angelica pluton is oriented parallel to the dextral Guaçuí shear zone, a regional structure with steep dips and dextral offest. However, the plutonic pattern of concentric foliation indicates that its final emplacement and deformation were little affected by tectonics. This suggests that magma was emplaced within a crust where horizontal stresses were minimal. Magmatic ascent opportunistically followed this pre-existing structure, but only buoyant forces appeared to be active by the time of magma formation and ascent. Thus, the

NE-SW dextral shearing and magmatic foliation are two distinct features that formed at different times.

The post-collisional period of gravitational collapse suggests that differential amounts of exhumation of deep-seated metamorphic rocks occurred between the hotter, central portion of the orogen versus its flanks. The current exposure of these rocks in the AO allows us to understand the different post-collisional deformational magmatic regimes across the temperature gradient from the core to the flanks of the orogen. Similarly, Guillot et al. (1993) showed through magnetic fabric studies that the Manaslu granite from Central Nepal (Himalayan belt) was emplaced during the gravitational collapse phase but it is related to localized E-W dextral shearing.

6 Conclusions

At the end of the orogenic event of the Neoproterozoic-Cambrian Western Aracuaí-Congo orogen (~ 500 Ma) the Araçuaí orogen was marked by intense magmatic activity (I-type granite). These plutons were emplaced along high angle ductile shear zones and core of antiform structures. Through the geochronological data, was determined that the Santa Angélica pluton was emplaced in the late Cambrian (506 ± 3 Ma for the felsic border and 498 ± 5 Ma for the mafic core). Such ages are interpreted as pluton crystallization. An age of 508 ± 3 Ma was obtained for a dioritic dike at 700 m from the eastern border of the pluton, which intrudes pre-collision Ediacaran plutonic rocks. Such dike may be related to the Santa Angelica pluton, as an apophysis.

The magnetic fabric study of the Santa Angélica pluton, shows that its anisotropy of magnetic susceptibility is carried by coarse-grained magnetite. Magnetic foliations and lineations of all lithotypes inside the pluton show a clear concentric pattern around both lobes that are separated by an intern shear zone with vertical sinistral movement. The emplacement of the Santa Angélica pluton corresponds to that of two partly overlapping plutons. At the final stages of body emplacement, an up movement of the northeastern lobe in relation to the southwestern lobe caused an internal sinistral shear zone between the two lobes. Because of this movement and AMS data, we hypothesize that the two lobes represent different levels of erosion, where the northeast lobe represents the deepest sectors of the intrusion, close to its feeding root. U-Pb and AMS data suggest that magma emplacement was controlled by magma buoyancy forces, (almost) free of stress tectonic.

Santa Angélica pluton is located close to Ribeira belt connection, far from the warmer internal zone of the orogen at 500 Ma. In this part of the orogen, some plutons (including Santa Angélica) of 'I-type' granitoid were emplaced along pre-existing high angle ductile shear zones and core of antiform structures, probably marking the extension phase of the orogenic event of the Western Aracuaí-Congo orogen. Then, the data indicate that the Santa Angélica pluton configures an intrusion associated to the last stage of granitogenesis of the Araçuaí belt, related to the extensional phase of the orogen. In contrast, in the northern part of the Araçuaí orogen these plutons of 'I-type' granitoid are larger and more common. These Cambrian plutonic rocks have organized structure typical of syn-collisional plutons. The structural difference between the internal concentric pattern of the pluton and the regional foliation pattern of the shear zone in which the pluton was emplaced is also observed in other large orogens (e.g. Himalayan belt).

Acknowledgments

The authors would like to express their gratitude to C.R. Cioffi for his support in the acquisition of data during field work, C. Guacaneme, J. W. L. Afonso and T. R. Moncinhatto for their support in the geochronological analysis. The infrastructure and collaborations of the Laboratório de Paleomagnetismo of the Universidade de São Paulo. This works was funded by grants of São Paulo Research Foundation (FAPESP, #2016/06114-6 and #2017/11672-0). The opinions, hypotheses and conclusions or recommendations expressed in this material are the authors' responsibility and do not necessarily reflect FAPESP's vision. SHRIMP analysis data used in this study are available in Supporting Information, geological survey data are available in the Brazilian Geological Survey database (http://geosgb.cprm.gov.br/). The data of the work will be available at mendeley data, doi: 10.17632/3xth2s5cp9.1. We thank the reviewers for many constructive comments and suggestions that greatly improved the manuscript.

References

Alkmim, F. F., Marshak, S., Pedrosa-Soares, A. C., Peres, G. G., Cruz, S. C. P., & Whittinton, A. (2006). Kinematic evolution of the Araçuaí-West Congo orogen in Brazil and Africa: Nutcracker tectonics during the Neoproterozoic assembly of Gondwana. *Precambrian Research*, 149(1-2), 43– 64. https://doi.org/10.1016/j.precamres.2006.06.007

Almeida, C. N., Guimarães, I. P., & Silva Filho, A. F. (2002). A-type post-collisional granites in the Borborema Province - NE Brazil: The Queimadas Pluton. *Gondwana Research*, 5(3), 667– 681. https://doi.org/10.1016/S1342-937X(05)70637-7

Amaral, L., Caxito, F. D. A., Pedrosa-Soares, A. C., Queiroga, G., Babinski, M., Trindade, R., Lana, C., & Chemale, F. (2020). The Ribeirão da Folha ophiolite-bearing accretionary wedge (Araçuaí Orogen, SE Brazil): New data for Cryogenian plagiogranite and metasedimentary rocks. *Precambrian Research*, 336, 105522. https://doi.org/10.1016/j.precamres.2019.105522

Archanjo, C. J., Trindade, R. I., Bouchez, J. L., & Ernesto, M. (2002). Granite fabrics and regional-scale strain partitioning in the Seridó belt (Borborema Province, NE Brazil). *Tectonics*, 21(1), 1– 14. https://doi.org/10.1029/2000TC001269

Archanjo, C. J., & Bouchez, J. L. (1997). Magnetic fabrics and microstructures of the post-collisional aegirine-augite syenite Triunfo Pluton, northeast Brazil. *Journal of Structural Geology*, 19(6), 849– 860. https://doi.org/10.1016/S0191-8141(97)00008-4

Baxter, S., & Feely, M. (2002). Magma mixing and mingling textures in granitoids: Examples from the Galway granite, Connemara, Ireland. *Mineralogy and Petrology*, 76(1), 63– 74. https://doi.org/10.1007/s007100200032

Bayer, B., Schimidt-Thomé, R., Weber-Diefenbach, K., & Horn, H. A. (1987). Complex concentric granitoid intrusions in the coastal mobile belt, Espírito Santo, Brazil: The Santa Angélica Pluton—An example. *Geologische Rubdschau*, 76(2), 357– 371. https://doi.org/10.1007/BF01821080

Beaumont, C., Nguyen, M. H., Jamieson, R. A., & Ellis, S. (2006). Crustal flow modes in large hot orogens. *Geological Society of London*, Special Publication, 268(1), 91– 145. https://doi.org/10.1144/GSL.SP.2006.268.01.05

Bosum, W. (1973). O levantamento aeromagnético de Minas Gerais e Espírito Santo e sua seqüência quanto a estrutura geológica. *Revista Brasileira de Geociencias*, 3(3), 149– 163. https://doi.org/10.25249/0375-7536.1973149159

Bouchez, J. L. (1997). Granite is never isotropic: An introduction to AMS studies of granitic rocks. In J. L. Bouchez, D. H. W. Hutton, & W. E. Stephens (Eds.), Granite: From segregation of melt to emplacement fabrics (Vol. 8, pp. 95– 112). Dordrecht: Kluwer Publishing Co.

Bouchez, J. L., Gleizes, G., Djouadi, T., & Rochette, P. (1990). Microstructure and magnetic susceptibility applied to emplacement kinematics of granites: the example of the foix pluton (French pyrenees). *Tectonophysics*, 184(2), 157– 171. https://doi.org/10.1016/0040-1951(90)90051-9

Bouchez, J. L., Guillet, P., & Chevalier, F. (1981). Structures d'ecoulement liees a Ia mise en place du granite de Guerande (Loire-Atlantique, France). Bulletin de la Société Géologique de France, S7-XXIII(4), 387– 399. https://doi.org/10.2113/gssgfbull.s7-xxiii.4.387

Calegari, S. S., Neves, M. A., Guadagnin, F., França, G. S., & Vincentelli, M. G. C. (2016). The Alegre lineament and its role over the tectonic evolution of the Campos Basin and adjacent continental margin, southeastern Brazil. *Journal of South American Earth Sciences*, 69, 226– 242. https://doi.org/10.1016/j.jsames.2016.04.005

Campos-Neto, M. C., & Figueiredo, M. C. H. (1995). The Rio Doce orogeny South-eastern Brazil. *Journal of South American Earth Sciences*, 8(2), 143– 162. https://doi.org/10.1016/0895-9811(95)00002-W

Cavalcante, C., Fossen, H., Almeida, R. P., Hollanda, M. H. B. M., & Egydio-Silva, M. (2019). Reviewing the puzzling intracontinental termination of the Araçuaí-West Congo orogenic belt and its implications for orogenic development. *Precambrian Research*, 322, 85– 98. https://doi.org/10.1016/j.precamres.2018.12.025

Cavalcante, C., Hollanda, M. H., Vauchez, A., & Kawata, M. (2018). How long can the middle crust remain partially molten during orogeny? *Geology*, 46(10), 839– 842. https://doi.org/10.1130/G45126.1

Cavalcante, C., Vauchez, A., Merlet, C., Egydio-Silva, M., Hollanda, M. H. B., & Boyer, B. (2014). Thermal conditions during deformation of partially molten crust from TitaniQ geothermometry: rheological implications for the anatectic domain of the Araçuaí belt, eastern Brazil. *Solid Earth*, 6(1), 1223– 1242. https://doi.org/10.5194/se-5-1223-2014

Cavalcante, G. C. G., Egydio-Silva, M., Vauchez, A., & Camps, P. (2013). Strain distribution across a partially molten middle crust: Insights from the AMS mapping of the Carlos Chagas Anatexite, Araçuaí belt (East Brazil). *Journal of Structural Geology*, 55, 79– 100. https://doi.org/10.1016/j.jsg.2013.08.001

Chernicoff, C. J., Richards, J. P., & Zappettini, E. O. (2002). Crustal lineament control on magmatism and mineralization in northwestern Argentina: Geological, geophysical, and remote sensing evidence. *Ore Geology Reviews*, 21(3-4), 127– 155. https://doi.org/10.1016/S0169-1368(02)00087-2

Chung, S. L., Chua, M. F., Zhangb, Y., Xieb, Y., Loa, C. H., Leec, T. Y., Land, C. Y., Lib, X., Zhange, Q., & Wang, Y. (2005). Tibetan tectonic evolution inferred from spatial and temporal variations in post-collisional magmatism. *Earth-Science Reviews*, 68(3-4), 173– 196. https://doi.org/10.1016/j.earscirev.2004.05.001

Cruden, A. R., & Launeau, P. (1994). Structure, magnetic fabric and emplacement of the Archean Lebel stock, SW Abitibi greenstone belt. *Journal of Structural Geology*, 16(5), 677– 691. https://doi.org/10.1016/0191-8141(94)90118-X

Davidson, A. (1995). A review of the Grenville orogen in its North American type area. *Journal of Australian Geology & Geophysics*, 16(1), 3– 24. http://pid.geoscience.gov.au/dataset/ga/81418

Day, R., Fuller, M., & Schmidt, V. A. (1977). Hysteresis properties of titanomagnetites: Grain-size and compositional dependence. *Physics of the Earth and Planetary Interiors*, 13(4), 260– 267. https://doi.org/10.1016/0031-9201(77)90108-X

De Campos, C. M., Medeiros, S. R., Mendes, J. C., Pedrosa-Soares, A. C., Dussin, I., Ludka, I. P., & Dantas, E. L. (2016). Cambro-Ordovician magmatism in the Araçuaí Belt (SE Brazil): Snapshots from a post-collisional event. *Journal of South American Earth Sciences*, 68, 248– 268. https://doi.org/10.1016/j.jsames.2015.11.016

De Campos, C. M., Mendes, J. C., Ludka, I. P., Medeiros, S. R., Moura, J. C., & Wallfass, C. (2004). A review of the Brasiliano magmatism in southern Espírito Santo, Brazil, with emphasis on post-collisional magmatism. *Journal of the Virtual Explorer*, 17, 1– 39. https://doi.org/10.3809/jvirtex.2004.00106

Dewey, J. F. (1988). Extensional collapse of orogens. *Tectonics*, 7(6), 1123– 1139. https://doi.org/10.1029/TC007i006p01123

Dunlop, D. J. (2002). Theory and application of the Day plot (M rs /M s versus H cr /H c) 1. Theoretical curves and tests using titanomagnetite data. *Journal of Geophysical Research*, 107(B3), 1– 22. https://agupubs.onlinelibrary.wiley.com/doi/full/10.1029/2001JB000486

Egydio-Silva, M., Vauchez, A., Fossen, H., Cavalcante, C. G., & Xavier, B. C. (2018). Connecting the Araçuaí and Ribeira belts (SE–Brazil): Progressivetransition from

contractional to transpressive strain regime during the Brasiliano orogeny. *Journal of South American Earth Sciences*, 86, 127– 139. https://doi.org/10.1016/j.jsames.2018.06.005

Fossen, H., Cavalcante, G. C., & de Almeida, R. P. (2017). Hot versus cold orogenic behavior: Comparing the Araçuaí-West Congo and the Caledonian Orogens. *Tectonics*, 36, 2159–2178. https://doi.org/10.1002/2017TC004743

Gleizes, G., Crevon, G., & asrat, A., Barbey, P. (2006). Structure, age and modeof emplacement of the Hercynian Boederes-Louron Pluton (CentralPyrenees, France). *International Journal of Earth Sciences*, 95(6), 1039– 1052. https://doi.org/10.1007/s00531-006-0088-4

Gonçalves, A., Sant'ovaia, H., & Noronha, F. (2019). Emplacement mechanism of Caria-Vila da Ponte Pluton, (Vol. 124, pp. 91– 111). Northern Portugal: Building and internal magmatic record. *Journal of Structural Geology*. https://doi.org/10.1016/j.jsg.2019.04.009

Gonçalves, L., Alkmim, F. F., Pedrosa-Soares, A. C., Dussin, I. A., Valeriano, C. D. M., Lana, C., & Tedeschi, M. (2016). Granites of the intracontinental termination of a magmatic arc: An example from the Ediacaran Araçuaí Orogen, southeastern Brazil. *Gondwana Research*, 36, 439– 458. https://doi.org/10.1016/j.gr.2015.07.015

Gradim, C., Roncato, J., Pedrosa-Soares, A. C., Cordani, U., Dussin, I., Alkmim, F. F., Queiroga, G., Jacobsohn, T., Silva, L. C., & Babinski, M. (2014). The hot back-arc zone of the Araçuaí Orogen, eastern Brazil: From sedimentation to granite generation. *Brazilian Journal of Geology*, 44(1), 155– 180. https://doi.org/10.5327/Z2317-4889201400010012

Grocott, J., Arévalo, C., Welkner, D., & Cruden, A. (2009). Fault-assisted vertical pluton growth: Coastal cordillera, north Chilean Andes. *Journal of the Geological Society*, 166(2), 295– 301. https://doi.org/10.1144/0016-76492007-165

Guillot, S., Pêcher, A., Rochette, P., & Le Fort, P. (1993). The emplacement of the Manaslu granite of Central Nepal: Field and magnetic susceptibility constraints. *Geological Society*, 74(1), 413– 428. https://doi.org/10.1144/GSL.SP.1993.074.01.28

Han, Y., Wang, Y., Zhao, G., & Cao, Q. (2014). Syn-tectonic emplacement of the late Mesozoic Laojunshan granite pluton in the eastern Qinling, Central China: An integrated fabric and geochronologic study. *Journal of Structural Geology*, 68, 1– 15. https://doi.org/10.1016/j.jsg.2014.08.005

Heilbron, M., & Machado, N. (2003). Timing of terrane accretion in the Neoproterozoic-Eopaleozoic Ribeira orogen (SE Brazil). *Precambrian Research*, 125(1-2), 87– 112. https://doi.org/10.1016/S0301-9268(03)00082-2

Horn, A. H. (2006). Folha Espera Feliz SE-24-V-A-IV, 1:100.000: Relatório final, (pp. 17–24). Belo Horizonte: UFMG, CPRM.

Horn, H. A., & Weber-Diefenbach, K. (1987). Geochemical and genetic studies of three inverse zoned intrusive bodies of both alkaline and subalkaline composition in the Araçuaí-Ribeira Mobile Belt (Espírito Santo, Brazil). *Revista Brasileira de Geociências*, 17(4), 488– 497. http://www.ppegeo.igc.usp.br/index.php/rbg/article/view/11961

Hrouda, R., & Hruskova, I. (1990). On the detection of weak strain parallel to the bending by magnetic anisotropy: A mathematical study. *Studia Geophysica et Geodaetica*, 34(4), 327–341. https://doi.org/10.1007/BF02316953

Jackson, M. (1991). Anisotropy of magnetic remanence: A brief review of mineralogical sources, physical origins, and geological applications, and comparison with susceptibility anisotropy. *Pure and Applied Geophysics*, 136(1), 1– 28. https://doi.org/10.1007/BF00878885

Jackson, M., Gruber, W., Marvin, J., & Banerjee, S. K. (1988). Partial anhysteretic remanence and its anisotropy: Applications and grainsize-dependence. *Geophysical Research Letters*, 15(5), 440– 443. https://doi.org/10.1029/GL015i005p00440

Jamieson, R. A., & Beaumont, C. (2011). Coeval thrusting and extension during post-convergent ductile flow— Implications for exhumation of high-grade metamorphic rocks. *Journal of Metamorphic Geology*, 29(1), 33– 51. https://doi.org/10.1111/j.1525-1314.2010.00908.x

Jamieson, R. A., & Beaumont, C. (2013). On the origin of orogens. *GSA Bulletin*, 125(11-12), 1671– 1702. https://doi.org/10.1130/B30855.1

Jelínek, V. (1978). Statistical processing of anisotropy of magnetic susceptibility measured on groups of specimen. *Studia Geophysica et Geodaetica*, 22(1), 50– 62. https://doi.org/10.1007/BF01613632

Johnson, S. E., Fletcher, J. M., Fanning, C. M., Vernon, R. H., Paterson, S. R., & Tate, M. C. (2003). Structure, emplacement and lateral expansion of the San José tonalite pluton, Peninsular Ranges batholith, Baja California, México. *Journal of Structural Geology*, 25(11), 1933– 1057. https://doi.org/10.1016/S0191-8141(03)00015-4

Knesel, K. M., Davidson, J. P., & Duffield, W. A. (1999). Open-system evolution of silicic magma by assimilation followed by recharge: Evidence from Sr isotopes in sanidine phenocrysts, Taylor Creek rhyolite, NM. *Journal of Petrology*, 40(5), 773– 786. https://doi.org/10.1093/petroj/40.5.773

Langille, J. M., Jessup, M. J., Cottle, J., & Ahmad, T. (2014). Kinematic and thermal studies of the Leo Pargil dome: Implications for synconvergent extension in the NW Indian Himalaya. *Tectonics*, 33, 1766– 1786. https://doi.org/10.1002/2014TC003593

Leblanc, D., Gleizes, G., Lespinass, E. P., Olivier, P. H., & Bouchez, J.-L. (1994). The Maladeta granite polydiapir, Spanish Pyrenees: A detailed magneto- structural study. *Journal of Structural Geology*, 16(2), 223– 235. https://doi.org/10.1016/0191-8141(94)90106-6

Marsh, B. D. (1981). On the crystallinity, probability of occurrence, and rheology of lava and magma. *Contributions to Mineralogy and Petrology*, 78(1), 85– 98. https://link.springer.com/article/10.1007/BF00371146

Medeiros, S. R., Wiedemann-Leonardos, C. M., & Mendes, J. C. (2000). Post-collisional multistage magmatism in the Ribeira mobile belt: Geochemical and isotopic study of the Várzea Alegre intrusive complex, Espírito Santo, Brazil. *Revista Brasileira de Geociencias*, 30(1), 030–034. https://doi.org/10.25249/0375-7536.2000301030034

Medeiros, S. R., Wiedemann-Leonardos, C. M., & Vriend, S. (2001). Evidence of mingling between contrasting magmas in a deep plutonic environment: The example of Várzea Alegre, in the Ribeira Mobile Belt, Espírito Santo, Brazil. *Anais da Academia Brasileira de Ciências*, 73(1), 99– 119. https://doi.org/10.1590/S0001-37652001000100009

Meneses, P. R., & Paradella, W. R. (1978). Síntese geológica preliminar da parte sul do Estado do Espírito Santo. In Simpósio Brasileiro de Sensoriamento Remoto (Vol. 5, pp. 479– 499). São José dos Campos (SP), 499: INPE/CNPq, Anais.

Mondou, M., Egydio-Silva, M., Vauchez, A., Raposo, M. I. B., Bruguier, O., & Oliveira, A. F. (2012). Complex, 3D strain patterns in a synkinematic tonalite batholith from the Araçuaí Neoproterozoic orogen (eastern Brazil): Evidence from combined magnetic and isotopic chronology studies. *Journal of Structural Geology*, 39, 158– 179. https://doi.org/10.1016/j.jsg.2012.02.015

Munhá, J. M. U., Cordani, U., Tassinari, C. C. G., & Paácios, T. (2005). Petrologia e termocronologia de gnaisses migmatíticos da Faixa de Dobramentos Aracuaí (Espírito Santo, Brasil). *Revista Brasileira de Geociencias*, 35, 123– 134. https://doi.org/10.25249/0375-7536.2005351123134

Narduzzi, F., Farina, F., Stevens, G., Lana, C., & Nalini, H. A. (2017). Magmatic garnet in the cordilleran-type Galiléia granitoids of the Araçuaí belt (Brazil): Evidence for crystallization in the lower crust. *Lithos*, 282-283, 82– 97. https://doi.org/10.1016/j.lithos.2017.02.017

Noce, C. M., Macambira, M. B., & Pedrosa-Soares, A. C. (2000). Chronology of Neoproterozoic-Cambrian granitic magmatism in the Araçuaí Belt, Eastern Brazil, based on single zircon evaporation dating. *Revista Brasileira de Geociências*, 30, 25– 29. https://doi.org/10.25249/0375-7536.2000301025029

Oliveira, D. C., Neves, S. P., Trindade, R. I. F., Dall'Agnol, R., Mariano, G., & Correia, P. B. (2010). Magnetic anisotropy of the Redenção granite, eastern Amazonian craton (Brazil): Implications for the emplacement of A-type plutons. *Tectonophysics*, 493(1-2), 27– 41. https://doi.org/10.1016/j.tecto.2010.07.018

Paterson, S. R., & Schmidt, K. L. (1999). Is there a close spatial relationship between faults and plutons? *Journal of Structural Geology*, 21(8-9), 1131– 1142. https://doi.org/10.1016/S0191-8141(99)00024-3

Paterson, S. R., Vernon, R. H., & Tobisch, O. T. (1989). A review of criteria for the identification of magmatic and tectonic foliations in granitoids. *Journal of Structural Geology*, 11(3), 349– 363. https://doi.org/10.1016/0191-8141(89)90074-6

Pedrosa-Soares, A. C., Alkmim, F. F., Tack, L., Noce, C. M., Babinski, M., Silva, L. C., & Martins-Neto, M. A. (2008). Similarities and differences between the Brazilian and African counterparts of the Neoproterozoic Aracuai-West Congo orogen. *Geological Society of London*, Special Publication, 294(1), 153– 172. https://doi.org/10.1144/SP294.9

Pedrosa-Soares, A. C., Campos, C. P., Noce, C., Silva, L. C., Novo, T., Roncato, J., Medeiros, S., Castañeda, Q. G., Dantas, E., Dussin, I., & Alkimim, F. (2011). Late Neoproterozoic-Cambrian granitic magmatism in the Araçuaí Orogen (Brazil), the eastern Brasilian Pegmatite Province and related mineral resources. *Geological Society*, 350(1), 25– 51. https://doi.org/10.1144/SP350.3

Pedrosa-Soares, A. C., Castañeda, C., Queiroga, G., Gradim, C., Belém, J., Roncato, J., Novo, T., Dias, P., Gradim, D., Medeiros, S., Jacobsohn, T., Babinski, M., & Vieira, V. (2006). Magmatismo e tectônica do Orógeno Araçuaí no Espírito Santo (18° - 19°, 41°- 40° 30'W). *Geonomos*, 16, 97– 111. https://doi.org/10.18285/geonomos.v14i2.114

Pedrosa-Soares, A. C., Cordani, U. G., & Numan, A. (2000). Constraining the age of Neoproterozoic glaciation in eastern Brazil: First U-PB (SHRIMP) data of detrital zircons. *Revista Brasileira de Geociências*, 30, 058–061. https://doi.org/10.25249/0375-7536.2000301058061

Pedrosa-Soares, A. C., Noce, C. M., Wiedemann, C. M., & Pinto, C. P. (2001). The Araçuaí–West Congo orogen in Brazil: An overview of a confined orogen formed during Gondwanland assembly. *Precambrian Research*, 110(1-4), 307– 323. https://doi.org/10.1016/S0301-9268(01)00174-7

Pedrosa-Soares, A. C., Wiedemann, C. M., Fernandes, M. L. S., Faria, L. F., & Ferreira, J. C. H. (1999). Geotectonic significance of the Neoproterozoic granitic magmatism in the Araçuaí Belt, eastern Brazil: a model and pertinent questions. *Revista Brasileira de Geociências*, 29(l), 59– 66. https://doi.org/10.25249/0375-7536.1999295966

Pedrosa-Soares, A. C., & Wiedemann-Leonardos, C. M. (2000). Evolution of the Araçuaí belt and its connection to the Ribeira Belt, eastern Brazil. In U. G. Cordani, E. J. Milani, A. Thomaz Filho, & D. A. Campos (Eds.). Tectonic evolution of South America, (pp. 265–285). SBG: São Paulo.

Perpétuo, M. P., Amaral, W. S., da Costa, F. G., Filho, E. C. U., & de Sousa, D. F. M. (2016). Geochemistry of the Serra das Melancias Pluton in the Serra da Aldeia suite: A classic post-collisional high Ba-Sr granite in the Riacho do Pontal Fold Belt, NE Brazil. Brazilian *Journal of Geology*, 46(2), 221– 237. https://doi.org/10.1590/2317-4889201620160002

Perugini, D., Poli, G., & Valentini, L. (2005). Strange attractors in plagioclase oscillatory zoning: Petrological implications. *Contributions to Mineralogy and Petrology*, 149(4), 482– 497. https://doi.org/10.1007/s00410-005-0667-6

Petitgirard, S., Vauchez, A., Egydio-Silva, M., Bruguier, O., Camps, P., Monié, P., & Mondou, M. (2009). Conflicting structural and geochronological data from the Ibituruna quartz-syenite (SE Brazil): Effect of protracted "hot" orogeny and slow cooling rate? *Tectonophysics*, 477(3-4), 174– 196. https://doi.org/10.1016/j.tecto.2009.02.039

Pitcher, W. S. (1978). The anatomy of a batholith. *Journal of the Geological Society*, 135(2), 157– 182. https://doi.org/10.1144/gsjgs.135.2.0157

Pitcher, W. S. (1979). The nature, ascent, and emplacement of granitic magrnas. *Journal of the Geological Society London*, 163, 627– 662. https://doi.org/10.1144/gsjgs.136.6.0627

Pitcher, W. S., & Bussel, M. A. (1977). Structural control of batholithic emplacement in Peru: a review. *Journal of the Geological Society*, 133(3), 249– 256. https://doi.org/10.1144/gsjgs.133.3.0249

Platt, J. P., & Vissers, R. L. M. (1989). Extensional collapse of thickened continental lithosphere: A working hypothesis for the Alboran Sea and Gibraltar arc. *Geology*, 17(6), 540– 543. https://doi.org/10.1130/0091-7613(1989)017<0540:ECOTCL>2.3.CO;2

Raposo, M. I. B., & Gastal, M. C. P. (2009). Emplacement mechanism of the main granite pluton of the Lavras do Sul intrusive complex, South Brazil, determined by magnetic anisotropies. *Tectonophysics*, 466(1-2), 18– 31. https://doi.org/10.1016/j.tecto.2008.10.015

Rey, P., Vanderhaeghe, O., & Teyssier, C. (2001). Gravitational collapse of the continental crust: Defi nition, regimes and modes. *Tectonophysics*, 342(3-4), 435– 449. https://doi.org/10.1016/S0040-1951(01)00174-3

Richter, F., Lana, C., Stevens, G., Buick, I., Pedrosa-Soares, A. C., Alkmim, F. F., & Cutts, K. (2016). Sedimentation, metamorphism and granite generation in a back-arc region: Records from the Ediacaran Nova Venécia complex (Araçuaí Orogen, southeastern Brazil). *Precambrian Research*, 272, 78– 100. https://doi.org/10.1016/j.precamres.2015.10.012

Roberts, A. P., Pike, C. R., & Verosub, K. L. (2000). First-order reversal curve diagrams: A new tool for characterizing the magnetic properties of natural samples. *Journal of Geophysical Research*, 105(B12), 28,461– 28,475. https://doi.org/10.1029/2000JB900326

Salazar, C. A., Archanjo, C. J., Babinski, M., & Liu, D. (2008). Magnetic fabric and zircon U-Pb geochronology of the Itaoca Pluton: Implications for the Brasiliano deformation of the southern Ribeira Belt (SE Brazil). *Journal of South American Earth Sciences*, 26(3), 286– 299. https://doi.org/10.1016/j.jsames.2008.08.007

Sant'Ovaia, H., Bouchez, J. L., Noronha, F., Leblanc, D., & Vigneresse, J. L. (2000). Composite-laccolith em-placement of the post-tectonic Vila Pouca de Aguiar granite pluton (northern Portugal): A combined AMS and gravity study: Transactions of the Royal Society of Edinburgh. Earth Sciences, Earth and Environmental Science Transactions of the Royal Society of Edinburgh, 91(1–2), 123– 137. https://doi.org/10.1017/S026359330000732X

Santiago, R., Caxito, F. A., Neves, M. A., Dantas, E. L., Medeiros Junior, E. B., & Queiroga, G. N. (2020). Two generations of mafic dyke swarms in the southeastern Brazilian coast: Reactivation of structural lineaments during the gravitational collapse of the Araçuaí-Ribeira Orogen (500 ma) and West Gondwana breakup (140 ma). *Precambrian Research*, 340. https://doi.org/10.1016/j.precamres.2019.105344

Schmidt-Thomé, R., & Weber-Diefenbach, K. (1987). Evidence for frozen-in magma mixing in Brasiliano calc-alkaline intrusions. The Santa Angélica Pluton, southern Espírito Santo, Brazil. *Revista Brasileira de Geociências*, 17, 498– 506.http://www.ppegeo.igc.usp.br/index.php/rbg/article/view/11962

Seymour, N. M., Singleton, J. S., Mavor, S. P., Gomila, R., Stockli, D. F., Heuser, G., & Arancibia, G. (2020). The relationship between magmatism and deformation along the intra-arc strike-slip Atacama fault system, northern Chile. *Tectonics*, 39, e2019TC005702. https://doi.org/10.1029/2019TC005702

Silva, L. C., Amstrong, R., Noce, C. M., Carneiro, M., Pimentel, M. M., Pedrosa-Soares, A. C., Leite, C. A., Vieira, V. S., Silva, M. A., Paes, V. J. C., & Cardoso Filho, J. M. (2002). Reavaliação da evolução geológica em terrenos pré-cambrianos brasileiros com base em novos dados U-Pb SHRIMP, parte II: Orógeno Araçuaí, Cinturão Móvel Mineiro e Cráton São Francisco Meridional. *Revista Brasileira de Geociências*, 32, 161– 174. https://doi.org/10.25249/0375-7536.2002324513528

Silva, L. C., McNaughton, N. J., Armstrong, R., Hartmann, L., & Fletcher, I. (2005). The Neoproterozoic Mantiqueira Province and its African connections. *Precambrian Research*, 136(3-4), 203– 240. https://doi.org/10.1016/j.precamres.2004.10.004

Slaby, E., Götze, J., Wörner, G., Simon, K., Wrzalik, R., & Śmigielski, M. (2008). K-feldspar phenocrysts in microgranular magmatic enclaves: A cathodoluminescence and geochemical study of crystal growth as a marker of magma mingling dynamics. *Lithos*, 105, 85– 97. https://doi.org/10.1016/j.lithos.2008.02.006

Söllner, F., Lammerer, B., & Weber-Diefenbach, K. (1991). Die Krustenentwicklung in der Küstenregion nördlich von Rio de Janeiro/Brasilien. Münchener Geowissenschaftliche Hefte 11, (Vol. 4). München: Friedrich Pfeil Verlag.

Söllner, H. S., Lammerer, B., & Wiedemann-Leonardos, C. (2000). Dating the Araçuaí-Ribeira Mobile Belt of Brazil. In: Sonderheft, Zeit. f. Angwandte Geologie, 1, 245– 255.

Spacapan, J. B., Galland, O., Leanza, H. A., & Planke, S. (2016). Control of strike-slip fault on dyke emplacement and morphology. *Journal of the Geological Society*, 173(4), 573– 576. https://doi.org/10.1144/jgs2015-166

Tedeschi, M., Novo, T., Pedrosa-Soares, A. C., Dussin, I., Tassinari, C., Silva, L. C., Gonçalves, L., Alkmim, F., Lana, C., Figueiredo, C., Dantas, E., Medeiros, S., De Campos, C., Corrales, F., & Heilbron, M. (2016). The Ediacaran Rio Doce magmatic arc revisited (Araçuaí-Ribeira orogenic system, SE Brazil). *Journal of South American Earth Sciences*, 68, 167– 186. https://doi.org/10.1016/j.jsames.2015.11.011

Trindade, R. I. F., Bouchez, J. L., Bolle, O., Nédélec, A., Peschler, A., & Poitrasson, F. (2001). Secondary fabrics revealed by remanence anisotropy: Methodological analysis and examples from plutonic rocks. *Geophysical Journal International*, 147(2), 310– 318. https://doi.org/10.1046/j.0956-540x.2001.01529.x

Vanderhaeghe, O. (2012). The thermal-mechanical evolution of crustal orogenic belts at convergent plate boundaries: A reappraisal of the orogenic cycle. *Journal of Geodynamics*, 56-57(57), 124– 145. https://doi.org/10.1016/j.jog.2011.10.004

Vauchez, A., Egydio-Silva, M., Babinski, M., Tommasi, A., Uhlein, A., & Liu, D. (2007). Deformation of a pervasively molten middle crust: Insights from the neoproterozoic Ribeira-Araçuaí orogen (SE Brazil). *Terra Nova*, 19(4), 278– 286. https://doi.org/10.1111/j.1365-3121.2007.00747.x

Vernon, R. H., Johnson, S. E., & Melis, E. A. (2004). Emplacement-related microstructures in the margin of a deformed pluton: The San José tonalite, Baja California, México. *Journal of Structural Geology*, 26(10), 1867– 1884. https://doi.org/10.1016/j.jsg.2004.02.007

Vieira, V. S. (2007). Significado do grupo Rio Doce no contexto do Orógeno Araçuaí. Tese de Doutorado, Belo Horizonte: Instituto de Geociências da Universidade Federal de Minas Gerais. 117 pp

Vigneresse, J. L., & Bouchez, J. L. (1997). Successive Granitic Magma Batches During Pluton Emplacement: the Case of Cabeza de Araya (Spain). *Journal of Petrology*, 38(12), 1767– 1776. https://doi.org/10.1093/petroj/38.12.1767

Wiedeman, C. L., Medeiros, S. R., Ldka, I. P., Mendes, J. C., & Costa-de-Moura, J. (2002). Architecture of late orogenic plutons in the AraGuai-Ribeira Fold Belt, Southeast Brazil. *Gondwana Research*, 5(2), 381– 399. https://doi.org/10.1016/S1342-937X(05)70730-9

Wiedemann, C. M., Bayer, P., Horn, H., Lammerer, B., Ludka, I. P., Schmidt-Thomé, R., & Weber-Diefenbach, K. (1986). Maciços intrusivos do sul do Espírito Santo e seu contexto regional. *Revista Brasileira de Geociências*, 16, 24– 37. https://doi.org/10.25249/0375-7536.19862437

Xavier, B. C. (2017). Relações tectônicas no Central da Faixa Araçuaí: Análise estrutural por AMS e geocronologia U/Pb e Lu/Rf (pp. 1– 123). São Paulo: Thesis Universidade de São Paulo.

Žák, J., Verner, K., Sláma, J., Kachlík, V., & Chlupáčová, M. (2013). Multistage magma emplacement and progressive strain accumulation in the shallow-level Krkonoše-Jizera plutonic complex, Bohemian Massif. *Tectonics*, 32, 1493– 1512. https://doi.org/10.1002/tect.20088

Zanon, M. L., Chaves, A. O., Rangel, C. V. G. T., Gaburu, L., & Pire, C. R. (2015). Os aspectos geológicos do Maciço Santa Angélica (ES): Uma nova abordagem. *Brazilian Journal of Geology*, 45(4), 609– 633. https://doi.org/10.1590/2317-4889201520150005

Chapter III

Magma ascent and storage across a collapsing large and hot orogen

F. A. Temporim, R. I. F. Trindade, M. Egydio-Silva, T.V. Angelo, E. Tohver, C. C. Soares, L. P. Gouvêa, J.C. Mendes, S.R. Medeiros, A.C. Pedrosa-Soares, G.G., Silva

Submitted to *Geology*

For supporting material see Appendix B

Abstract: Large and hot orogens undergo gravitational collapse producing mass flow directed to its flanks. Featuring a 3000 km-long large and hot orogen, the Mantiqueira Province provides a rare opportunity to study the process of gravitational collapse at mid to deep crustal levels. Distinct but contemporary (~500 Ma) post-collisional intrusions show structures and anisotropy of magnetic susceptibility (AMS) fabrics related to their emplacements, recording different internal flow patterns. In southern deep-seated intrusions, ellipsoidal-shaped roots with gabbroic-to-hybrid cores surrounded by granitic rocks show concentric patterns of AMS fabrics that cut across the NE-trending regional foliation. In contrast, northern intrusions, exposed as the upper sections of batholith-size bodies of coarse-grained granite emplaced at the shallow to mid-crust, show general NS-trending magnetic fabrics roughly parallel to strike of the orogen and the regional foliation of host rocks. These contrasting magnetic patterns from shallow to deep crust suggest magma migration from the overthickened orogen core to be stored across its thinner stretched flanks during the gravitational collapse of the orogen edifice.

Keywords: orogen collapse; magma emplacement; magnetic anisotropy; Araçuaí orogen

1. Introduction

Large and hot orogens are characterized by wide plateaus developed over an overthickened crust, with high thermal gradients that cause partial melting on suitable rocks in the middle and lower crust along the orogen's core (Brown, 2001; Vanderhaeghe and Teyssier, 2001). Crustal high heat production through radiogenic decay also tends to weakens the orogen's infrastructure (England and Thompson, 1984; Henk, 2000; Vanderhaeghe et al., 2003). In the final stages, orogenic topography is flattened by the effects of erosion and gravitational collapse, whereby extension and crustal thinning reduces lateral gradients of gravitational potential energy through lateral flow of the hot orogenic interior towards its flanks (Rey et al., 2001). The geological expressions of these tectonic processes in an orogen hot core are hard to decode since they usually overprint complex pre-collisional and syn-collisional structures.

The Mantiqueira Province (Fig. 3.1) comprises several attributes expected for a large and hot orogen (Cavalcante et al., 2018). The Araçuaí–Ribeira orogenic system (AROS) experienced intense magmatic activity between 630–480 Ma (Fig. 3.1D) with a high-temperature regime sustained for ~90 m.y. in the orogen core, followed by a significant low in magmatic-metamorphic activity (ca. 540–520 Ma) before post-collisional igneous episodes (Pedrosa-Soares et al., 2020). The syn-kinematic high-temperature regime assisted the development of a complex 3D deformation pattern (Alkmim et al., 2006; Pedrosa-Soares et al., 2011), including orogen-parallel mass transport and stretching in the center of the belt (Mondou et al., 2012; Cavalcante et al., 2018), building up the orogenic framework that came to host the post-collisional magmatism.

The post-collisional Cambrian-Ordovician magmatism resulted in a string of intrusions decreasing in size from north to south along eastern AROS (Fig. 3.1C). They form composite stocks to batholiths, rich in magma mingling-mixing features of high-K calc-alkaline-ferroan A- and I-type granitic, and charnockitic rocks (De Campos et al., 2016; Araujo et al., 2020). Post-collisional intrusions found in the north have provided crystallization pressures in the range of 2.4-3.5 kbar, while in the south they were emplaced at pressures around 5.7-11.5 kbar (Fig. 3.1C). The current exposure level represents a crustal section from former depths of ~10 km, in the north to ~35 km, in the south (Wiedemann et al., 2002; Serrano et al., 2018). In the north, post-collisional plutons form large, elongated, N-striking bodies parallel to the belt. In contrast, in the south, the deep-seated sections of post-collisional intrusions consist mostly of round-shaped plutons with hybrid cores.

We performed a detailed mapping of magnetic fabrics using the anisotropy of magnetic susceptibility (AMS) of coeval plutons at different sectors of the belt, corresponding to different crustal levels (Fig. 3.1C). The presence of melt in a deforming crust and the lateral temperature gradients across the orogen implies that the strain is heterogeneous on various scales (Vanderhaeghe and Teyssier, 2001). The internal fabric of granitic plutons results from the interplay between body forces due to magma chamber dynamics and the regional and gravitational stresses imposed onto the magma bodies. The dominance of regional stress over body forces is reflected in the degree of coupling between the pluton interior and the host rocks.

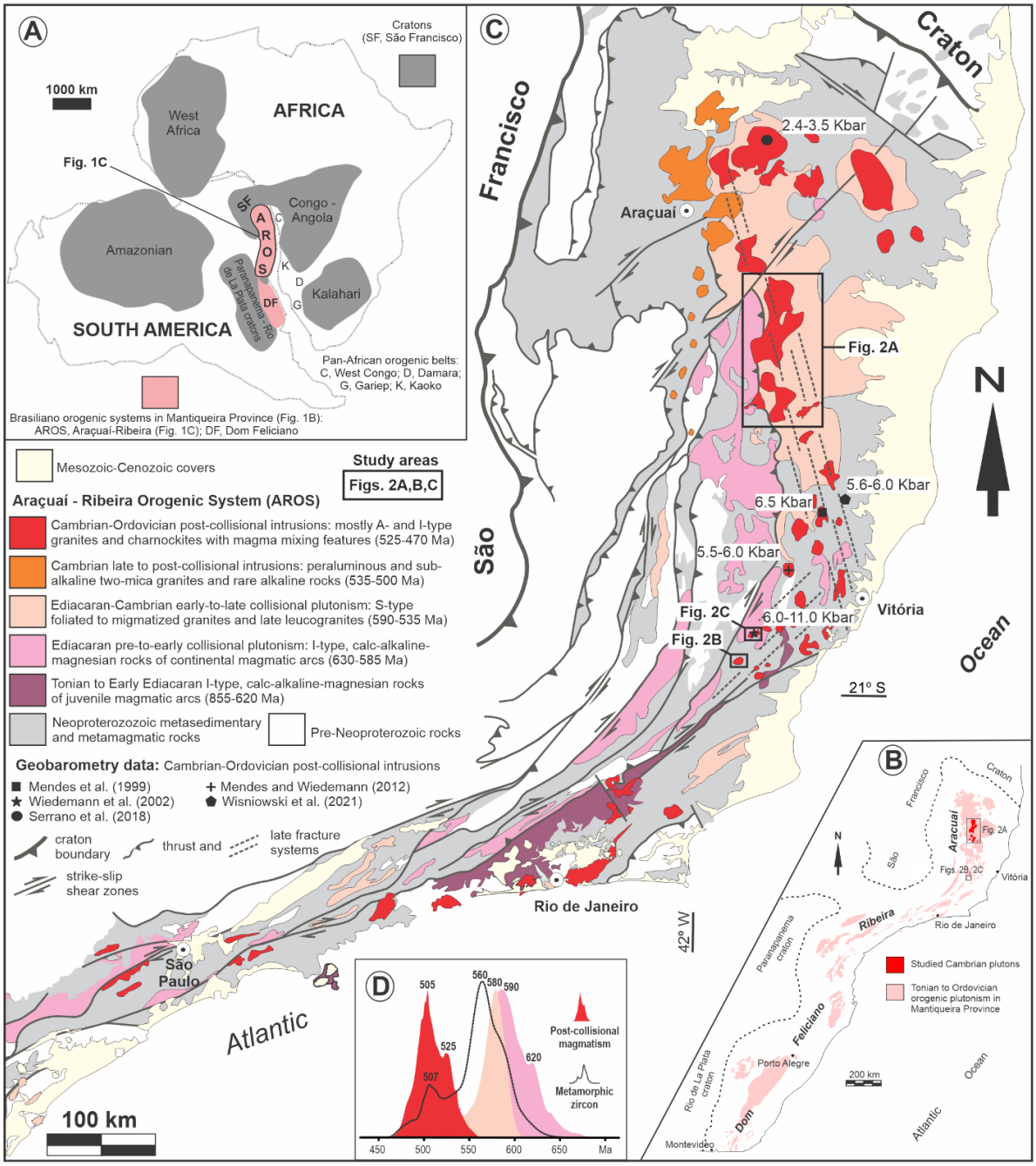

Figure 3.1. A, the study region in West Gondwana. B, sketch map highlighting the igneous rocks of the Mantiqueira Province (simplified from Silva et al., 2005). C, the Araçuaí-Ribeira orogenic system with location of study areas. D, U-Pb ages for zircons from orogenic igneous rocks, and U-Pb ages for metamorphic zircons (Pedrosa-Soares et al., 2020) and compilation of geobarometry data from post-collisional intrusions.

2. Geological Setting

The AROS is an orogenic system about 3000 km long and up to 800 km wide (Fig. 3.1). The N-trending Araçuaí orogen shows a double-verging hot core, comprising different assemblages of orogenic igneous rocks formed in distinct tectonic stages: the pre-collisional (630-580 Ma), syn-collisional (585-545 Ma), late-collisional (545-530 Ma), and post-collisional (530-480 Ma) (Pedrosa-Soares et al., 2011, updated in Table B1 of Appendix B). These successive events of magma production imply in high geothermal gradients maintained for a long time span (Gradim et al., 2014; Cavalcante et al., 2018). Thermobarometric data coupled with U-Pb ages suggest the middle crust was partially molten (750–920 ºC) at intermediate to quite high pressures (5–11 kbar) between 600–540 Ma in the orogen core (Vauchez et al., 2007; Melo et al., 2017; Pedrosa-Soares et al., 2020). Slow cooling (~3-5°/Myr) persisted up to ~525 Ma, under low decompression (42.5 bar/Ma) and exhumation (157 m/Ma) rates, but it was followed by crustal reheating associated with voluminous production of granitic magma until ~500 Ma (Serrano et al., 2018; Vauchez et al., 2007; Araujo et al., 2020), when the studied plutons were emplaced (Fig. 3.2). The Araçuaí orogen merges southward into the NE-trending Ribeira orogen where wrench and strike-slip tectonics dominate in late orogenic stages (Egydio-Silva et al., 2018). The studied plutons are located in the central-eastern Araçuaí orogen and in the Araçuaí–Ribeira boundary sector (Fig. 3.1B).

3. Sampling and Results

A total of 295 magnetic anisotropy stations were compiled from the literature (references in Fig. 3.2) and 52 new stations were added in the present study. Datasets were compiled for rocks from the north (Vargem Grande – VG, and Caladão – C, plutons; Fig. 3.2A) and south domains (Santa Angelica – SA, and Conceição de Muqui - CM plutons; Figs. 3.2B and 3.2C). All magnetic measurements were carried out with an MFK1 susceptometer (Agico Ltd.) at the Laboratório de Paleomagnetismo of Universidade de São Paulo (USPmag). In addition, hysteresis loops and measurements of susceptibility against temperature were performed to characterize the magnetic mineralogy of the rocks (Table B2 of Appendix B).

Thermomagnetic curves for CM and SA plutons show a simple behavior during cooling and heating, with steep drops in susceptibility at temperatures of -153°C and 580°C, coincident with the Verwey transition and the Curie temperature of pure magnetite, respectively (Fig. B.1 of Appendix B). VG and C plutons, in the north, show poorly defined Verwey (-153°C) and Morin (-18°C) transitions that characterize magnetite and hematite, respectively (Fig. B.2 of

Appendix B). Heating of samples from these intrusions causes an increase in susceptibility at ~480°C and a subsequent decrease at ~580°C (Fig. B.2 of Appendix B). In all cases, constricted magnetic hysteresis and first-order reversal curves indicate low-coercivity multi-domain magnetite is the main carrier of the magnetic fabric in these rocks (Fig. B.3 of Appendix B) (Cavalcante et al., 2013; Xavier, 2017; Angelo et al., 2020; Temporim et al., 2020).

Fig. 3.3 shows AMS parameters for the north and south domains. T x P plot shows a dominantly flattened fabric for the northern plutons (red circles), whereas those from the south (blue circles) have triaxial ellipsoid shapes with T values ranging from 0.5 to -0.5. The south domain shows high values of Km and P, while the north domain presents low to medium values of Km and P.

Magnetic and field measurements are consistent for both regions. In the north, AMS results are homogenous, with shallowly dipping magnetic foliation that ranges in strike from NW to NE. Such structural pattern is consistent with magnetic and magmatic foliations reported by Mondou et al. (2012) and Angelo et al. (2020), as well as with the double-verging ductile fabrics of the central orogen core (Novo et al., 2018), revealing a strong coupling between those post-collisional plutons and the regional tectonic framework. The C pluton shows shallowly dipping NS to NE-striking magnetic foliations with a magnetic lineation that plunges gently to the SW. Magnetic foliations within the VG pluton (Fig. 3.2A) dip gently to the NE to NW with a sub-horizontal NNW-trending magnetic lineation. A small subset of samples from the VG pluton has sub-vertical magnetic lineations (Fig. 3.2A). In contrast, the south domain rocks are defined by concentric patterns of lithology distribution and structural fabric (Figs. 3.2B,C), with gently-dipping NE to E-trending lineations at felsic borders and vertical in the mafic cores (Fig. 3.2C).

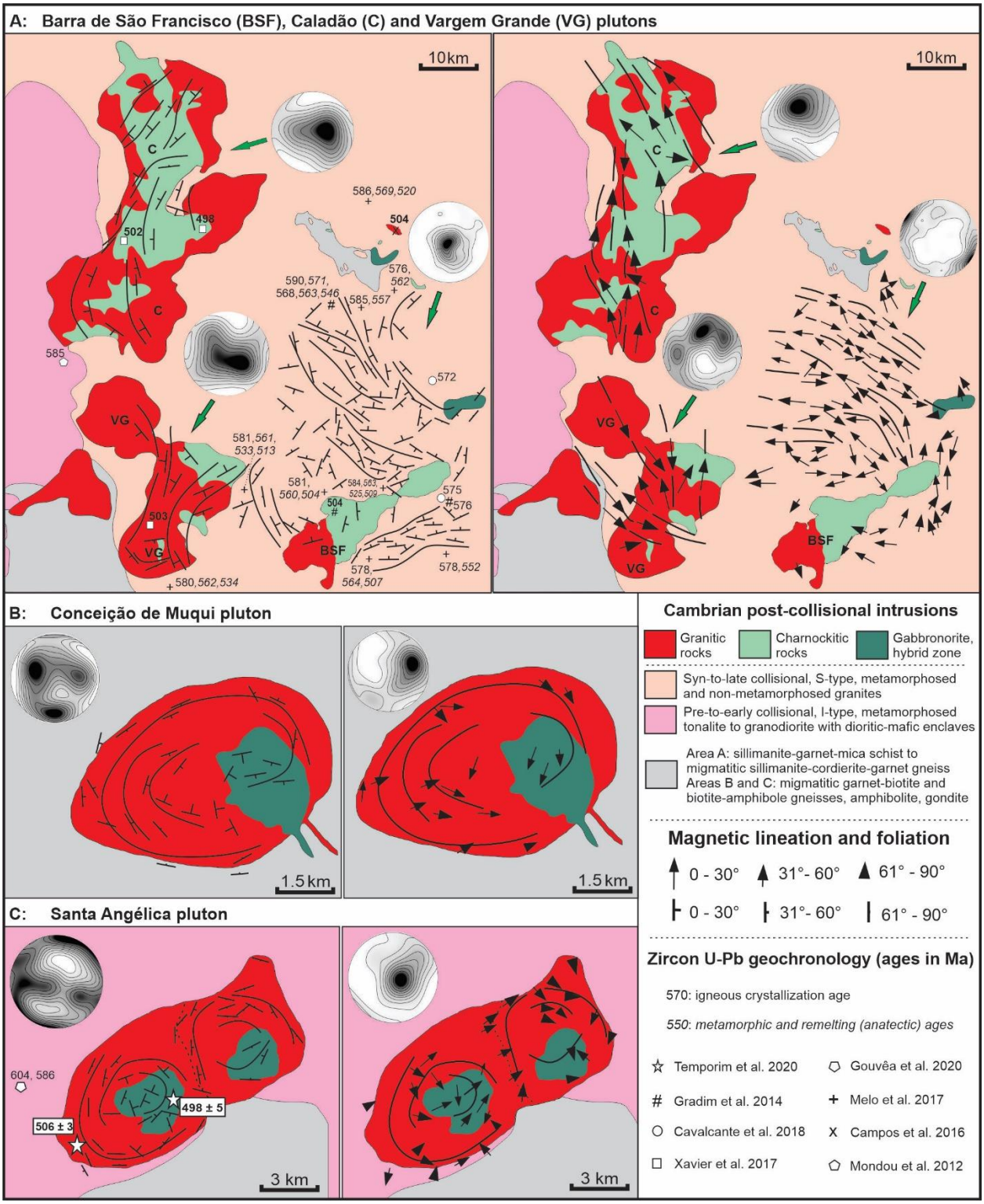

Figure 3.2. Magnetic foliations and lineations of post-collisional plutons and compilation of U-Pb radiometric ages for the north (A) and south (B and C) study areas. Stereoplots for AMS foliation and lineation are displayed for each studied pluton. Magnetic data sources: Vargem Grande (VG), this study; Xavier et al. (2017); Angelo et al. (2020); Barra do São Francisco (BSF), Cavalcante et al. (2013); Caladão (C), this study, Mondou et al. (2012); Xavier et al. (2017); Angelo et al. (2020); Conceição de Muqui Pluton: this study; Santa Angélica pluton: Temporim et al. (2020).

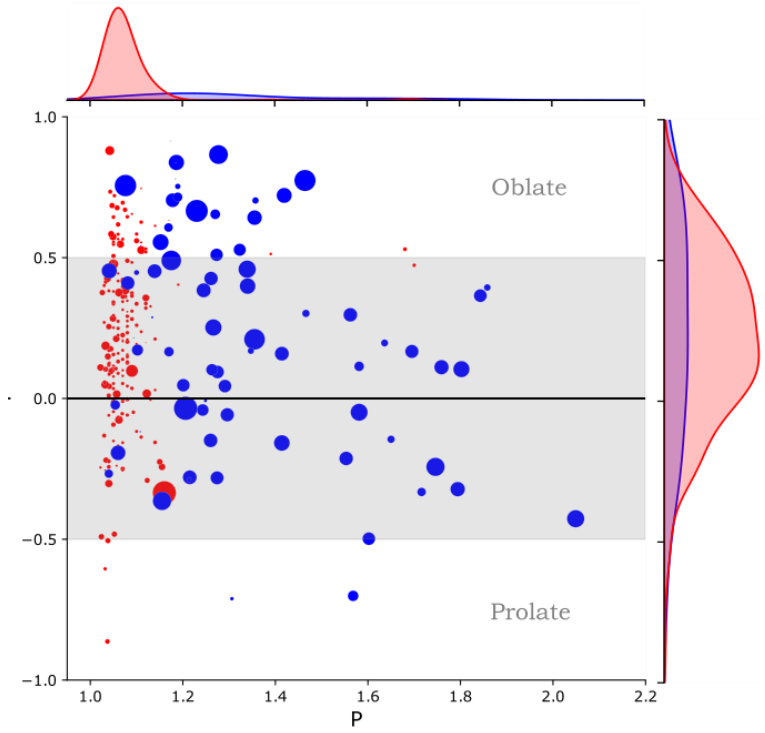

Figure. 3.3. Jelinek plot (TxP). Red and blue circles represent north and south domain respectively, and the size of the circles varies with the bulk magnetic susceptibility (Km). The dispersion of the T and P parameters also is shown in the figure.

4. Discussion

In the Araçuaí orogen, post-collisional plutons (~500 Ma) are exposed at different crustal levels with a depth range of 10-20 km between the north and the south. The plutons show distinct relations to the previous regional structural framework. In the north (Fig. 3.2A), early-to-late collisional granites and amphibolite-facies migmatites (785 °C and 7.5 kbar, Richter et al., 2016) are the main host rocks enclosing post-collisional plutons. In the south (Fig. 3.2B), plutons are hosted by high-amphibolite to granulite facies rocks (670-860 °C and 5.24-10.2 kbar, Gouvêa et al., 2020) of the Ediacaran magmatic arc and related supracrustal rocks. Before magmatic quiescence between 545–525 Ma in the north domain, high amounts of melt hindered strain localization into major shear zones (Cavalcante et al., 2018; Melo et al., 2017). Both areas attained the metamorphic peak at ~560 Ma (Pedrosa-Soares et al., 2021). Under such conditions, strain is widely distributed in the middle crust, taken up wherever melt is present (Vauchez et al., 2007). The collisional granitic rocks generally show a variably oriented magnetic pattern but mostly shallowly dipping, with a lineation varying from perpendicular (E-

W) to locally parallel (N-S) to the orogen (Fig. 3.2A). The north domain post-collisional plutons show a low-angle NS to NE-SW trending magnetic foliation bearing a down-dip magnetic lineation following the general trend of the orogen, but cutting the magnetic pattern of the exposed host collisional granitic rocks (Fig. 3.2A). However, the low-angle NS to NE-trending magnetic pattern is consistent with the regional magnetic pattern and tectonic framework of the central orogen core, suggesting magma migration along the main NS-trending structures and, finally, being emplaced at extensional sites cutting across the host collisional batholith. In the south, the fabric developed during the late collisional event is concentrated along previous dextral strike-slip shear zones (Fig. 3.1). Post-collisional plutons accompanying these shear zones are nearly isotropic in the field, they truncate previously developed fabrics and show a concentric magnetic fabrics with vertical lineation at their central nuclei, in a pattern similar to those found in post-tectonic intrusions where magma emplacement forces dominate their internal deformation (Temporim et al., 2020).

During orogen collapse the outward gravitational spreading drives thrusting at the flanks of the orogen that is simultaneous with ductile extension and thinning in the core (Rey et al., 2001). The flow direction is determined by the path of least resistance. Usually, 2D models are incapable of modeling the complexity of the orogen-parallel post-convergent processes. But orogen-parallel mass flow is ubiquitous in active and past orogens being reported in the Tibetan Plateau (Royden et al., 2008; Jessup et al., 2014), the Eastern Alps (Frisch and Kuhlemann, 2000) and the Canadian Cordillera (Vanderhaeghe and Teyssier, 2001). The current AROS crustal exposures allow us to depict the different regimes of post-collisional magmatic ascent and storage along-strike and across a crustal section comprising the shallow crust in the north and deeper crustal levels in the south.

Figure 3.4 represents a crustal block diagram during orogen collapse. In the north, upper crust thinning was accommodated by E-W extension recorded in low-angle shear zones that operated synchronously to the extensive post-tectonic granite plutonism (Peixoto et al., 2017), showing that the whole crust was involved in orogen collapse. Inside the orogen core, the dominant structures observed are sub-horizontal foliations associated with flattening and horizontal along-strike mass flow (Figs. 3.2A and 3.4). Previously formed steeply dipping structures may have been strongly obliterated by this mass flow. In the south, deeper in the crust, the feeding zones of this large post-collisional magmatism are represented by vertical fabrics (Fig. 3.3 and 3.4) in the plutons with a strong contribution of mantle derived magmas, sometimes mingled with the granitic types or forming the nuclei of the intrusions.

Such specific relationships between the steep orogenic structures at the orogenic flanks and the late, pervasive sub-horizontal structures in the orogenic core, are also observed in other large and hot orogens (e.g., Grenville orogen, Jamieson et al., 2010). Post-convergent exhumation of deep-seated metamorphic rocks accompanies the erosion at the orogenic flanks and the extension and ductile thinning in the orogenic core (Jamieson and Beaumont, 2011). Since in the AROS these different lithotectonic domains were exhumed, we have a rare opportunity to actually see this rheological stratification (Fig. 3.4) and the root from where large volumes of magma originated from the mantle and the mantle-crust boundary (De Campos et al., 2016). These magmas were likely entrained by the relatively steep shear zones that transect the metamorphic sequence and border the plutons in the southern sector (Fig. 3.4), cutting down into the deep crust as predicted in numerical models (Jamieson and Beaumont, 2011). In this case, the emplacement of hot material over a cooler substrate is commonly interpreted as resulting in an "inverted" metamorphic sequence (Jamieson and Beaumont, 2013), with a peak temperature at the partially molten mid-crustal section (Fig. 3.4).

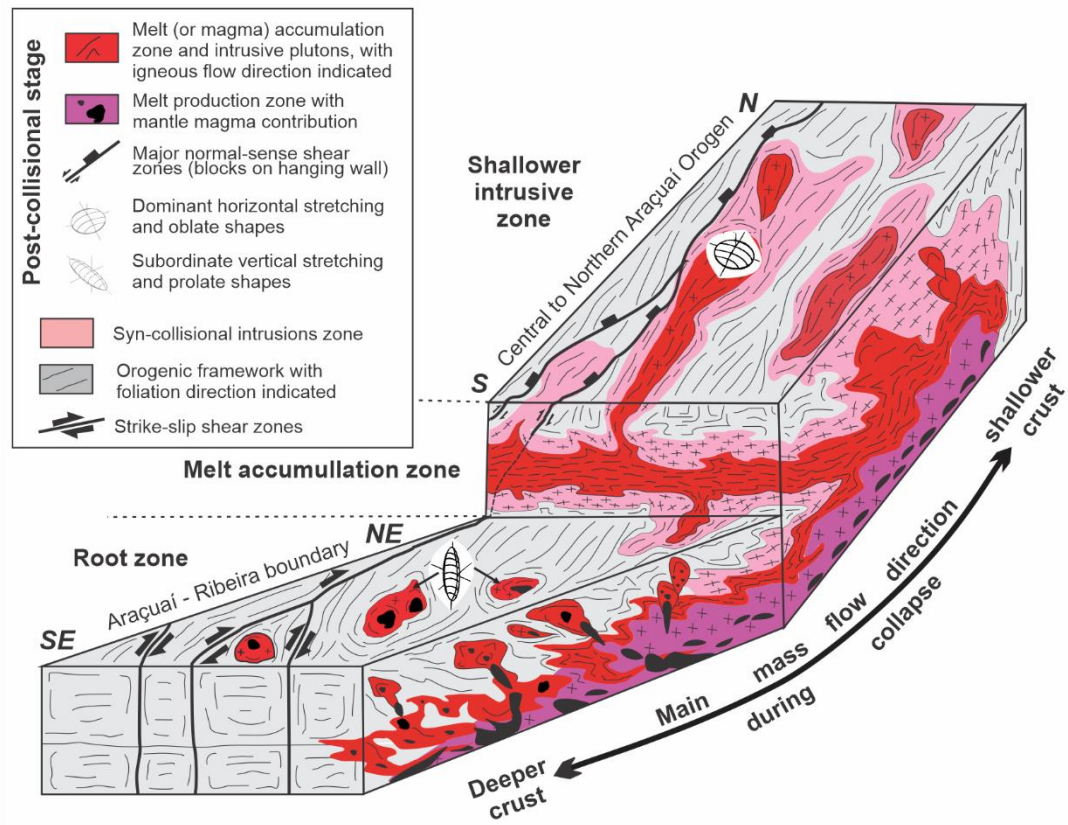

Figure 3.4. Schematic 3D cross-section of orogen-parallel post-convergent gravitational collapse at ~500 Ma. A substantial amount of orogenic core material in the form of hybrid magma was transported through NE-trending shear zones and emplaced at the mid-crust.

5. Conclusion

In the collapse phase, contrasting rheological behavior of the crust at different levels is well marked by the structures in magmatic rocks from northern to southern Aracuai-Ribeira orogenic system. In the north, post-collisional magmatic rocks have ~NS-trending magnetic foliations following the collisional tectonic framework and marking a general along-strike magmatic flow from south to north, i.e., from deeper to shallower crustal levels. In turn, coeval deep-seated intrusions in the south present a concentric distribution of foliations and lineations, in striking contrast with the general NE-SW trend of the host rocks. Such contrasting magnetic patterns coupled with structural fabrics and geochemical signatures demonstrate that gravitational collapse was accompanied by the generation of abundant magmatism in the orogen's hot keel that flowed from these deep sources to its previously stretched flanks.

Acknowledgments

Funds were granted by São Paulo Research Foundation (#2016/06114-6 and #2017/11672-0); Coordenação de Aperfeiçoamento de Pessoal de Nível Superior, Brasil (CAPES/SIU 0013) and Conselho Nacional de Desenvolvimento Científico e Tecnológico (#405954/2016-6 and #304214/2018-3). The opinions, hypotheses and conclusions or recommendations expressed in this material are the authors' responsibility and do not necessarily reflect FAPESP's vision.

References

Alkmim, S. Marshak, A.C. Pedrosa-Soares, G.G. Peres, S.C.P. Cruz, A. Whittington, (2006). Kinematic evolution of the Araçuaí-West Congo orogen in Brazil and Africa: Nutcracker tectonics during the Neoproterozoic assembly of Gondwana. *Precambr. Res*., 149: pp. 43-64

Angelo, T.V., Egydio-Silva, M., Temporim, F.A., Seraine, M., (2020). Midcrust deformation regime variations across the Neoproterozoic Araçuaí hot orogen (SE Brazil): Insights from structural and magnetic fabric analyses. *Journal of Structural Geology*, v. 134, 104007, https://doi.org/10.1016/j.jsg.2020.104007.

Araujo, C., Pedrosa-Soares, A., Lana, C., Dussin, I., Queiroga, G., Serrano, P., Medeiros-Junior, E., (2020). Zircon in emplacement borders of post-collisional plutons compared to country rocks: A study on morphology, internal texture, U-Th-Pb geochronology and Hf isotopes (Araçuaí orogen, SE Brazil). *Lithos*, v. 352, p. 105252. https://doi.org/10.1016/j.lithos.2019.105252.

Beaumont, C., Jamieson, R., Nguyen, M., (2010). Models of large, hot orogens containing a collage of reworked and accreted terranes. *Canadian Journal of Earth Sciences*, v. 47, p. 485-515.

Brown, M., (2001) Orogeny, migmatites and leucogranites: a review. *J. Earth Syst. Sci*. 110, 313-336.

Cavalcante, G. C. G., Egydio-Silva, M., Vauchez, A., Camps, P., (2013). Strain distribution across a partially molten middle crust: Insights from the AMS mapping of the Carlos Chagas Anatexite, Araçuaí belt (East Brazil). *Journal of Structural Geology*, v. 55, p. 79-100, https://doi.org/10.1016/j.jsg.2013.08.001.

Cavalcante C., Hollanda M. H., Vauchez A., Kawata M. (2018). How long can the middle crust remain partially molten during orogeny?. *Geology*, v. 46, p. 839-842, https://doi.org/10.1130/G45126.1.

De Campos C.M., Medeiros, S. R., Mendes J.C., Pedrosa-Soares, A. C., Dussin, I., Ludka, I. P., Dantas, E. L. (2016). Cambro-Ordovician magmatism in the Araçuaí Belt (SE Brazil): Snapshots from a post-collisional event. *Journal of South American Earth Sciences*, v. 68, p. 248-268. https://doi.org/10.1016/j.jsames.2015.11.016.

Egydio-Silva, M., Vauchez, A., Fossen, H., Cavalcante, C. G., Xavier, B. C. (2018). Connecting the Araçuaí and Ribeira belts (SE–Brazil): Progressive transition from contractional to transpressive strain regime during the Brasiliano orogeny. *Journal of South American Earth Sciences*, v. 86, p. 127-139, https://doi.org/10.1016/j.jsames.2018.06.005.

England, P.C., Thompson, A.B. (1984). Pressure-temperature-time paths of regional metamorphism I. Heat transfer during the evolution of regions of thickened continental crust. *J. Petrol*. 25, 894-928.

Frisch W., Dunkl, I., Kuhlemann, J. (2000). Post-collisional orogen-parallel large-scale extension in the Eastern Alps. *Tectonophysics*, v. 327, p. 239-265. DOI:10.1016/S0040-1951(00)00204-3.

Gouvêa, L.P., Medeiros, S.R., Mendes, J.C., Soares, C., Marques, R., Melo, M. (2020). Magmatic activity period and estimation of P-T metamorphic conditions of pre-collisional opx-metatonalite from Araçuaí-Ribeira orogens boundary, SE Brazil. *Journal of South American Earth Sciences*, v. 99, 102506, https://doi.org/10.1016/j.jsames.2020.102506.

Gradim C., Roncato J., Pedrosa-Soares A.C., Cordani U.G., Dussin I.A., Alkmim F.F., Queiroga G., Jacobsohn T., Silva L.C., Babinski M. (2014). The hot back-arc zone of the Araçuaí orogen, Eastern Brazil: from sedimentation to granite generation. *Brazilian Journal of Geology*, 44(1):155-180. 10.5327/Z2317-4889201400010012

Henk, A., von Blanckenburg, F., Finger, F., Schaltegger, U., Zulauf, G. (2000). Syn-convergent high-temperature metamorphism and magmatism in the Variscides: a discussion of potential heat sources. *Geol. Soc. Lond*., Spec. Publ. 179, 387-399. https://doi.org/10.1144/GSL.SP.2000.179.01.23

Jamieson, R.A., and Beaumont, C. (2011). Coeval thrusting and extension during post-convergent ductile flow - Implications for exhumation of high-grade metamorphic rocks. *Journal of Metamorphic Geology*, v. 29, p. 33–51, doi:10.1111/j.1525-1314.2010.00908.x.

Jamieson, R. A., and Beaumont, C. (2013). On the origin of orogens: GSA Bulletin, v. 125, p. 1671-1702, https://doi.org/10.1130/B30855.1.

Jessup, M.J., Newell, D.L., Cottle, J.M., Berger, A.L., Spotila, J.A. (2014). Orogen-parallel extension and exhumation enhanced by denudation in the trans-Himalayan Arun River gorge, Ama Drime Massif, Tibet-Nepal. *Geology*, v. 36; p. 587-590. doi:10.1130/G24722A.1.

Melo, M.G., Lana, C., Stevens, G., Pedrosa-Soares, A.C., Gerdes, A., Alkmin, L.A., Nalini Jr., H.A., Alkmim, F.F. (2017). Assessing the isotopic evolution of S-type granites of the Carlos Chagas batholith, SE Brazil: Clues from U-Pb, Hf isotopes, Ti geothermometry and trace element composition of zircon. *Lithos* 284-285, 730-750.

Mondou, M., Egydio-Silva, M., Vauchez, A., Raposo, M. I. B., Bruguier, O., Oliveira, A. F., (2012). Complex, 3D strain patterns in a synkinematic tonalite batholith from the Araçuaí Neoproterozoic orogen (Eastern Brazil): evidence from combined magnetic and isotopic chronology studies. *Journal of Structural Geology*, v. 39, p. 158-179. https://doi.org/10.1016/j.jsg.2012.02.015.

Novo, T.A., Pedrosa-Soares, A., Vieira, V.S., Dussin, I., Silva, L.C. (2018). The Rio Doce Group revisited: An Ediacaran arc-related volcano-sedimentary basin, Araçuaí orogen (SE Brazil). *Journal of South American Earth Sciences* 85, 345-361.

Pedrosa-Soares, A.C., Campos, C., Noce, C., Silva, L.C., Novo, T., Roncato, J., Medeiros, S., Castañeda, C., Queiroga, G., Dantas, E., Dussin, I., Alkmim, F. (2011). Late Neoproterozoic-Cambrian granitic magmatism in the Araçuaí orogen (Brazil), the Eastern Brazilian Pegmatite Province and related mineral resources. In: A.N. Sial, J.S. Bettencourt, C.P. De Campos, V.P. Ferreira (Eds.), Granite-Related Ore Deposits, Geological Society, Special Publications, London, pp. 25-51.

Pedrosa-Soares, A.C., Deluca, C., Araujo, C.S., Gradim C., Lana, C., Dussin, I., Silva, L.C., Babinski, M. (2020). O Orógeno Araçuaí à luz da geocronologia: um tributo a Umberto Cordani. In: Geocronologia e evolução tectônica do Continente Sul-Americano: a contribuição de Umberto Giuseppe Cordani. São Paulo: Solaris Edições Culturais, p. 250-272.

Peixoto, E., Alkmim, F.F., Pedrosa-Soares, A., Lana, C., Chaves, A.O. (2017). Metamorphic record of collision and collapse in the Ediacaran-Cambrian Araçuaí orogen, SE-Brazil: Insights from P–T pseudosections and monazite dating. *J Metamorph Geol*., v. 36, p. 147–172. DOI: 10.1111/jmg.12287.

Rey, P., Vanderhaeghe, O., and Teyssier, C. (2001). Gravitational collapse of the continental crust: Definition, regimes and modes. *Tectonophysics*, v. 342, p. 435–449, doi:10.1016/S0040-1951(01)00174-3.

Rey, P.F., Teyssier, C., and Whitney, D.L. (2009). Extension rates, crustal melting, and core complex dynamics. *Geology*, v. 37, p. 391–394, doi:10.1130/G25460A.1.

Royden, L.H., Burchfiel, B.C., van der Hilst, R.V. (2008). The Geological Evolution of the Tibetan Plateau. *Science*, v. 321, p. 1054-1058. DOI:10.1126/science.1155371.

Serrano, P., Pedrosa-Soares, A., Medeiros-Junior, E., Fonte.Boa, T., Araujo, C., Dussin, I., Queiroga, G., Lana, G. (2018). A-type Medina batholith and post-collisional anatexis in the

Araçuaí orogen (SE Brazil). *Lithos*, v. 320, p. 515-536. https://doi.org/10.1016/j.lithos.2018.09.009.

Silva, L. C. da, McNaughton, N. J., Armstrong, R., Hartmann, L. A., Fletcher, I. R. (2005). The Neoproterozoic Mantiqueira Province and its African connections: a zircon-based U–Pb geochronologic subdivision for the Brasiliano/Pan-African systems of orogens. *Precambrian Research*, v. 136, p. 203-240.

Temporim, F.A., Trindade, R.I.F., Tohver, E., Soares, C.C., Gouvêa, L.P., Egydio-Silva, M., Amaral, C.A.D., Souza Jr., G.F. (2020). Magnetic fabric and geochronology of a Cambrian "isotropic" pluton in the Neoproterozoic Araçuaí orogeny. *Tectonics*, v. 39(5), e2019TC005877. https://doi.org/10.1029/2019TC005877.

Vanderhaeghe, O., Teyssier, C. (2001). Crustal-scale rheological transitions during late-orogenic collapse. *Tectonophysics*, v. 335, p. 211-228. DOI:10.1016/S0040-1951(01)00053-1

Vanderhaeghe, O., Medvedev, S., Fullsack, P., Beaumont, C., Jamieson, R.A. (2003). Evolution of orogenic wedges and continental plateaux: insights from crustal thermal-mechanical models overlying subducting mantle lithosphere. *Geophys. J. Int*. 153, 27-51.

Vanderhaeghe, O., Teyssier, C. (2001). Partial melting and flow of orogens. *Tectonophysics*, 342, 451-472.

Vauchez, A., Egydio-Silva, M., Babinski, M., Tommasi, A., Uhlein, A., Liu, D. (2007). Deformation of a pervasively molten middle crust: insights from the Neoproterozoic Ribeira-Araçuaí orogen (SE Brazil). *Terra Nova*, v.19, p. 278-286, https://doi.org/10.1111/j.1365-3121.2007.00747.x.

Xavier, B.C. (2017). Relações tectônicas no Central da Faixa Araçuaí: análise estrutural por AMS e geocronologia U/Pb e Lu/Rf [Msc Thesis]: São Paulo, Universidade de São Paulo 123p.

Wiedemann, C. L., Medeiros, S. R., Ludka, I. P., Mendes, J. C., Costa-de-Moura, J. (2002). Architecture of Late Orogenic Plutons in the Araçuaí-Ribeira Fold Belt, Southeast Brazil. *Gondwana Research*, v. 5, p. 381-399, 10.1016/S1342-937X(05)70730-9.

Chapter IV

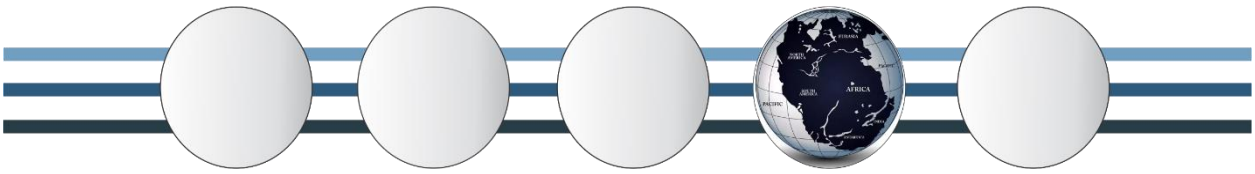

Reassessing the Cambrian drift of Gondwana with new paleomagnetic data from post-collisional plutons of the Araçuaí orogen, SE Brazil

F. A. Temporim, U. D. Bellon, M. Domeier, R. I. F. Trindade, M.S. D'Agrella-Filho, E. Tohver

Published in *Precambrian Research* in July 2021, *https://doi.org/10.1016/j.precamres.2021.106212*

For supporting material see Appendix C

Abstract: Despite their importance in constraining the dynamics of Gondwana's final phase of assembly, Cambrian paleomagnetic data from Gondwana are sparse. The Cambrian paleomagnetic dataset of Western Gondwana is especially poor, being defined by only a handful of poles. Here we contribute new Furongian paleomagnetic data from the ~500 Ma post-collisional, Santa Angelica and Venda Nova plutons from the southern portion of the Araçuaí orogen in SE Brazil. The characteristic magnetization isolated from both plutons reveals two groups of directions that are demonstrated to be antipodal. On the basis of a thermal diffusion model, we attribute these antipodal directions to primary thermoremanent magnetizations acquired by cooling of the plutons in the presence of a reversing field. Together, paleomagnetic results from 35 sites distributed between the two plutons allows computation of a new ~500 Ma paleopole, the SAVN: 4.7° N, 332.2° E, A95=4.06 and K=68.82. This pole does not resemble any younger paleomagnetic poles either from Gondwana or the independent South American plate after the demise of Pangea, but instead closely corresponds to the Miaolingian and Furongian sector of reference apparent polar wander paths for Gondwana. It also agrees well with the limited existing individual early Paleozoic poles from Western Gondwana. Our new result may thus be regarded as a reference pole for Western Gondwana in Furongian time. Considerations of the Cambrian paleomagnetic data from Eastern and Western Gondwana suggest that while the supercontinent was amalgamated by ~500 Ma, there was likely significant motion between Eastern and Western Gondwana in earlier Cambrian time (Terreneuvian-Cambrian Epoch 2).

Keywords: Paleomagnetism, Western Gondwana, Cambrian, Araçuaí Orogen, Thermal diffusion model

1. Introduction

Gondwana was the largest continental crustal unit on Earth for over 200 million years (Meert and Van der Voo, 1997). This supercontinent comprised the current African continent, Madagascar, India, Arabia, and much of southwestern Europe, South America, Antarctica, Australia (Torsvik & Cocks, 2011), as well as many smaller units such as Florida, the Taurides of Turkey, and parts of central Asia and China (Torsvik and Cocks, 2017). Following the breakup of preceding supercontinental assemblies (Meert and Van der Voo, 1997), Gondwana was generated through a series of major orogenic events, including the East African and Brasiliano-Pan-African events, which marked the closure of Neoproterozoic oceans (Kröner & Stern, 2005). The East African orogeny started the process between 800 and 650 Ma (Wilson et al., 1997), but the subsequent evolution of Gondwana remains somewhat unclear. Although the bulk of the supercontinent is generally considered to have been assembled by ca. 550 Ma (Meert and Van der Voo, 1997), some important cratonic elements (e.g. Amazonia, West Africa) may not have fully amalgamated with central Gondwana until the Cambrian Epoch 2–Furongian (Trindade et al., 2006; Tohver et al., 2012), although an early amalgamation, at 650-600 Ma, is also advocated (e.g., Ganade de Araújo et al., 2014). Some terranes (e.g. Avalonian and Armonian Terrane Assemblage) along the eastern flank of the Appalachian–Caledonian orogen (Pollock et al. 2012), were separated from Gondwana in the Late Cambrian (Furongian) and Lower Ordovician (Tremadocian) (Torsvik and Cocks, 2017). To reach a full understanding of this key terminal phase of Gondwana's assembly will require additional paleogeographic constraints.

Continental paleogeography can be derived from paleomagnetic studies that can determine the latitude and orientation of a given continent with respect to the spin axis of the Earth (Torsvik et al., 2012). However, there is a scarcity of high-quality paleomagnetic data of Cambrian age from Gondwana, resulting in persisting uncertainties concerning global paleogeography at this time (Tohver et al., 2006; Li et al., 2013). Here we work to rectify this deficiency through the presentation of a high-quality paleomagnetic pole obtained from Furongian post-collisional plutons of the Araçuaí orogen, SE Brazil. Together with the existing data from Gondwana, we use this new result to constrain the Furongian-Tremadocian drift of Gondwana.

2. Regional geology of the post-collisional pluton from the Araçuaí orogen

The Ribeira, Araçuaí, and Western Congo belts form an orogenic system ~500 km wide and >1000 km long resulting from the Brasiliano-Pan-African event, and represent the final amalgamation of the Gondwana supercontinent (Fig. 4.1A) (Pedrosa-Soares et al., 2001, Alkmim et al., 2006; Tedeschi et al., 2016). This Neoproterozoic-Cambrian orogen is contained in a great recess delineated on three sides by ancient, crystalline basement rocks of the São Francisco and Congo cratons. The Araçuaí orogen (AO) merges to the south with the coastal Ribeira orogen, forming the Araçuaí-Ribeira orogenic system (AROS) (Tedeschi et al., 2016) (Fig. 4.1A).

Different magmatic supersuites following the typical geochemical and structural evolution of collisional settings have been recognized in the region (Pedrosa Soares et al., 2011), comprising : (i) a pre-collisional G1 supersuite, represented by the Rio Doce magmatic arc (630–585 Ma); (ii) a syn-collisional G2 supersuite, represented by garnet-bearing leucogranites (585–560 Ma); (iii) a late-collisional G3 supersuite comprising mostly leucogranites (560–535 Ma); and (iv) post-collisional supersuites G4 and G5 (530–480 Ma). This last phase is inferred to relate to the gravitational collapse of the orogen, leading to an extensional regime at the end of the Brasiliano Orogeny. In the north, Cambrian post-collisional plutons form large, elongated N-striking bodies parallel to the belt (Fig. 4.1A). In the south, the volume of post-collisional magma was significantly lower and the intrusions are mostly circular in shape (Fig. 4.1A). These plutons mostly include I-type and A-type granitic rocks, and their Opx-bearing charnockitic equivalents (Pedrosa-Soares & Wiedemann-Leonardos, 2000; De Campos et al., 2016). Usually they form inversely-zoned, balloon-like plutons, composed of granitic-charnockitic rocks and gabbronoritic cores, with striking magma mixing and mingling features, and chemical-isotopic evidence of mantle involvement (De Campos et al., 2016) (Fig. 4.1B,C). No tectonic movement is recorded after this phase in the AO, therefore the post-collisional plutons from the south do not show evidence of displacement (De Campos et al., 2016, Temporim et al., 2020).

The Venda Nova (VN) pluton corresponds to an elliptical structure with a ~75 km² area (Fig. 4.1B) and concentric structures arrayed about the whole body (Mendes and De Campos, 2012). The country rocks are biotite-garnet-sillimanite gneisses and orthogneisses. Gradual contacts are subvertical and the foliation of the pluton is parallel to the contact with the country rocks and it dips towards the interior of the intrusion (Mendes and De Campos, 2012). The VN

pluton is inversely zoned with a felsic border and mafic core. It exhibits a gabbro-norite core, a chanockitic ring at the western border, and a syeno-monzonite envelope and monzodiorite in the interior of the pluton, as a result of commingling between the syeno-monzonite and gabbro-norite units (Mendes and De Campos, 2012).

The Santa Angelica (SA) pluton (Fig. 4.1C) covers about 200 km² and is an elliptical-shaped intrusion elongated along a NE-SW axis and with concentric structures arrayed about a twin, bull´s eye pattern (De Campos et al., 2016; Temporim et al., 2020). The country rocks are biotite-garnet-sillimanite gneisses and biotite-hornblende granodioritic to tonalitic gneisses. Gradual contacts between the intrusion and the country rock are subvertical and the foliation at the border of the pluton is parallel to the contact with the country rocks (De Campos et al., 2016), dipping towards the interior of the intrusion. The SA pluton is also inversely zoned with felsic rocks at the borders and more intermediate-mafic rocks towards the cores of the twin intrusions (Schmidt-Thomé and Weber-Diefenbach, 1987). The commingling and mixing zones are defined through field and geochemical data by Bayer et al. (1987). Hybrid rocks, resulting from commingling of basic and acidic magmas are widespread in the intrusion. U-Pb zircon ages constrain the crystallization age of different suites within the SA: 506 ± 3 Ma for the felsic border and 498 ± 5 Ma for the mafic core (Temporim et al., 2020).

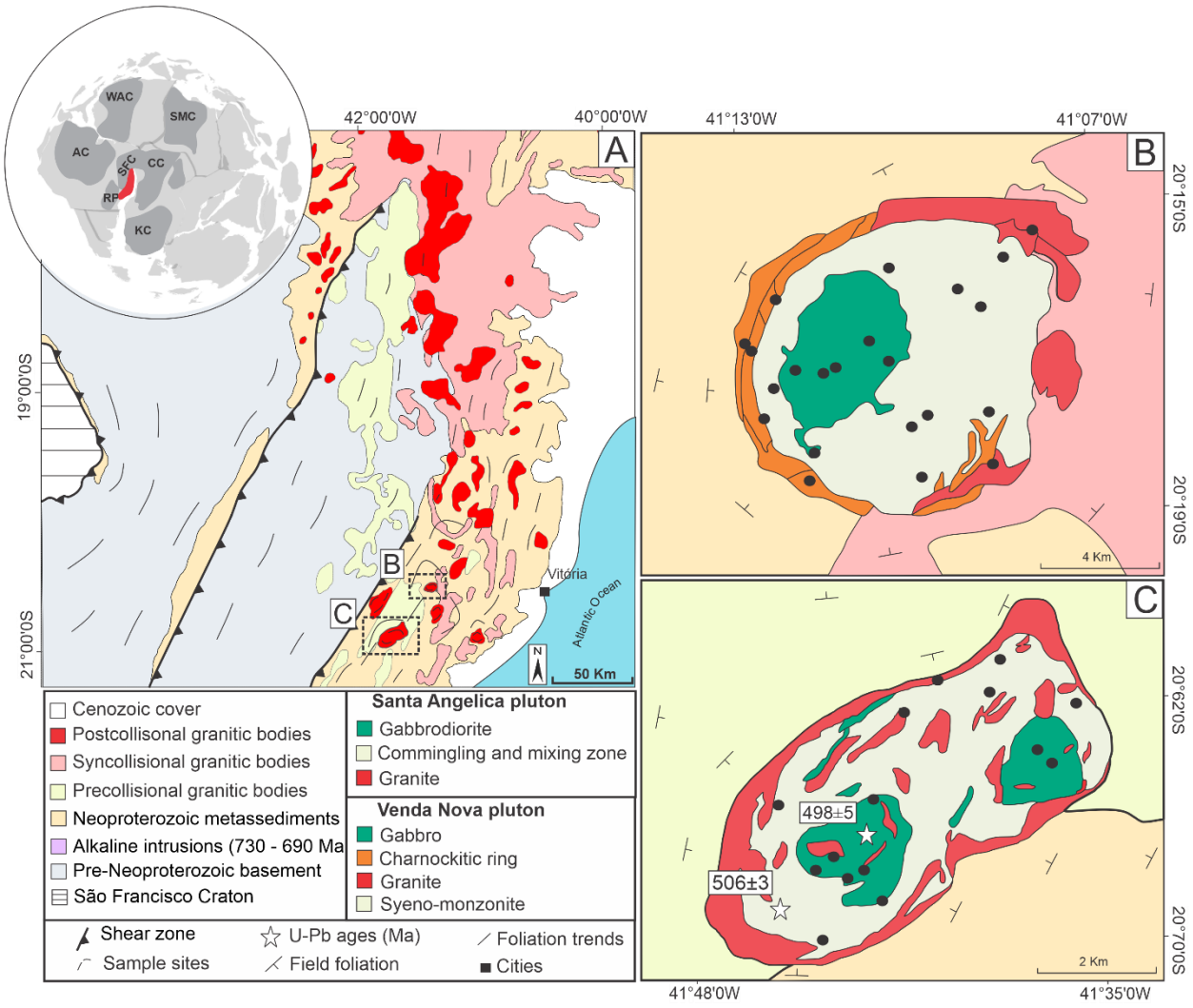

Figure 4.1. (A) Simplified geological map of the Araçuaí orogenic system (the red inset shows the location of the Araçuaí-Ribeira orogen in Western Gondwana) (modified from Pedrosa Soares and Wiedmann-Leonardos, 2000). (B) Geological map with facies distribution for Venda Nova (VN) pluton and country rocks (Mendes and De Campos, 2012). (C) Geological map with facies distribution for Santa Angélica (SA) pluton and country rocks (modified from Schmidt-Thomi and Weber-Diefenbach 1987). Paleomagnetic sampling sites are denoted with black dots. Stars represent U-Pb analyses from SA (Temporim et al., 2020). AC: Amazonian Craton; CC: Congo Craton; KC: Kalahari Craton; RP: Rio de la Plata Craton; SFC: São Francisco Craton; SMC: Sahara Meta-Craton; WAC: West African Craton.

3. Paleomagnetism

3.1. Sampling and Methods

Paleomagnetic samples were collected from multiple rock types from both VN (22 sites) and SA (15 sites) (Fig. 4.1B,C). Between five and seven cores of approximately 8 cm in length and 2.5 cm in diameter were collected at each site using a portable gasoline-powered drill. The

cores were oriented in the field by sun and magnetic compasses. In the laboratory, samples were cut into 22×25 mm cylindrical specimens and submitted to thermal (TH) or alternating field (AF) demagnetization. Paleomagnetic analyses were performed in the Laboratório de Paleomagnetismo of the Universidade de São Paulo (USPmag). Remanent magnetizations were measured with a 2G-Enterprises SQUID magnetometer. AF demagnetizations were executed with an automated three-axis AF-demagnetizer coupled with the magnetometer. TH demagnetizations were performed with an ASC TD48SC paleomagnetic oven (peak temperatures within ±5 ◦C). These instruments are housed in a magnetically shielded room with ambient field <500 nT. Magnetic components for each specimen were identified in orthogonal plots and calculated through principal component analysis (PCA) (Kirschvink, 1980). Vector mean directions were computed using standard Fisher statistics (Fisher, 1953).

A total of 127 specimens from the SA pluton and 198 specimens from the VN pluton were analyzed. After measuring their natural remanent magnetization (NRM), two specimens from each site were submitted to AF demagnetization with steps of 1 mT (1-10 mT), 2 mT (10-20 mT), 5 mT (20-50 mT) and 10 mT (50-100 mT), and two other specimens were submitted to TH with steps of 50 °C (100-500 °C), 20 °C (500-560 °C), 10 °C (560-580 °C) and 20 °C (580-680 °C). AF demagnetization was then applied to all sites where AF demagnetization was effective. For all remaining sites (for which AF demagnetization was not adequate alone), demagnetization followed a combination of two steps: AF demagnetization at 5 and 10 mT to suppress the contribution of MD magnetite, and then complete TH demagnetization with the steps described above.

A series of rock magnetic experiments were executed to investigate the magnetic mineralogy to better understand the paleomagnetic results. Thermomagnetic experiments were conducted under argon flux to prevent excessive oxidation during heating using a CS-2 furnace attached to an Agico Kappabridge KLY 4 CS. All thermomagnetic K-T curves (susceptibility vs. temperature) were determined in the temperature interval from −200 to 700°C. Isothermal remanent magnetization (IRM) curves and hysteresis curves were obtained with a vibrating sample magnetometer (VSM) MicroMag 3,900 (Princeton Measurements Corp).

3.2. Paleomagnetic results

K-T curves, magnetic hysteresis and IRMs were measured on several samples from each lithology of the SA and VN plutons to characterize the magnetic mineralogy. All facies have

almost the same behavior, as showed by Temporim et al, (2020). Hence, the results from one sample from each pluton are presented in Fig. 4.2.

The K-T curves of all samples exhibit major transitions (identified from the derivative of the curves, i.e. dK/dT) at -169.3°C and 578.6°C for SA, and at -168.9°C and 566.3°C for VN pluton, interpreted as the Verwey Transition (VT) and the magnetite Curie Temperature (MCT), respectively (Fig. 4.2A). Magnetic hysteresis (Fig. 4.2B) of the samples reveal similar Mrs/Ms relations and a high Hcr/Hc, with thin hysteresis, typical of an assemblage dominated by multidomain (MD) magnetite. IRMs (Fig. 4.2C) show quick saturation around 0.1T and an Hcr smaller than 20 mT. These results suggest that magnetite is the main carrier of the magnetic remanence in both the SA and VN plutons, and that some of the magnetite occurs in the form of MD grains. The presence of such MD magnetite is of concern since it can acquire a remanence at relatively low temperatures, but may survive TH treatment up to 450°C, and can thus obscure the remanent magnetizations carried by pseudo-single and single domain magnetite (Dunlop and Argyle, 1991). To address this problem, all specimens subjected to TH demagnetization were first subjected to AF of 5 and 10 mT to suppress any contributions from MD magnetite. A typical example of the success of this approach can be seen in sample SA43D2 (Fig. 4.3).

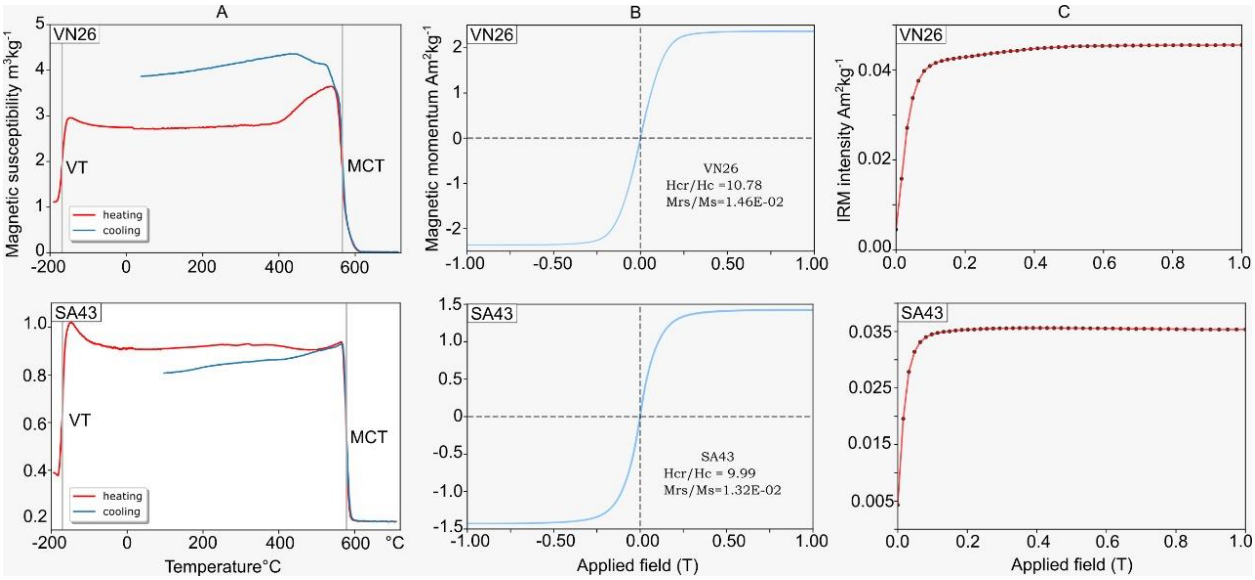

Figure 4.2 - Investigations of the magnetic mineralogy of the Venda Nova (VN) and Santa Angélica (SA) plutons. A- thermomagnetic curves for gabbroic rocks of VN and SA showing the Verwey transition (VT) and magnetite Curie temperature (MCT). B- Magnetic hysteresis and C- Isothermal remanence magnetization (IRM) acquisition curves. Hcr: remanence coercivity, Hc: bulk coercivity, Mrs: saturation remanent magnetization, Ms: saturation magnetization.

Submitted to demagnetization, individual samples exhibited a variety of magnetization unblocking behaviors. Some samples exhibited unstable behavior during demagnetization with no well-defined linear segments or great-circle trajectories and so were excluded from further analysis. All other paleomagnetic results from the VN and SA plutons are summarized in Table 4.1. Characteristic AF and TH demagnetization results are depicted in Fig. 4.3. AF demagnetization proved effective for almost all sites (Fig. 4.3), and the complete demagnetization of most samples was attained at relatively high peak fields between 40-100 mT (Fig. 4.3). Some sites were not completely demagnetized by AF and TH demagnetization was necessary (SA40 and VN9). In these cases, demagnetization was generally characterized by 'hard-shouldered' behavior, with unblocking mostly occurring within a narrow range of temperatures between 540-580 °C (e.g. SA40A3, VN7D2, VN9G2 and VN25C1 in Fig. 4.3). However, both methods of demagnetization resulted in similar directional data (Fig. 4.3). The most common behavior observed during demagnetization was dual-component decay, with a low coercivity/temperature component being eliminated before reaching a stable high temperature or high coercivity direction (e.g. SA43 in Fig. 4.3). In these samples, the low-stability component was removed during the initial steps of demagnetization (5–20 mT or 100–150 °C), and its remanence is probably carried by coarse-grained MD grains. After removal of the low-stability component, the magnetic vector proceeds univectorially to the origin, allowing definition of the characteristic remanent magnetization (ChRM). SA43D2 (Fig. 4.3) sample present ~80% of decay in intensity of the demagnetization curve during the initial steps of AF demagnetization (5 and 10 mT) before starting thermal treatment (representing ~20% of decay). It shows how a low-stability component was removed during the initial steps of demagnetization, which is most likely related to MD grains of magnetite.

Site#	N/m	Geographical coordinates		Site mean direction				VGP	
		Lat. (S)	Long. (W)	Dec (°)	Inc (°)	α_{95}	K	Plong. (°E)	Plat. (°N)
Santa Angélica pluton									
SA23	6/6	20° 41′ 57.902″	41° 26′ 54.866″	354.5	55.0	14.6	22.12	227.7	55.1
SA34	6/6	20° 43′ 39.204″	41° 26′ 42.743″	76.2	60.8	6.2	116.66	84.2	59.6
SA37	12/8	20° 42′ 39.409″	41° 25′ 37.141″	46.2	75.1	3.0	352.45	30.4	83.2
SA38	8/8	20° 42′ 17.245″	41° 26′ 25.051″	65.1	83.5	5.5	103.17	357.7	68.3
SA40	10/10	20° 42′ 6.591″	41° 25′ 59.143″	65.8	78.6	2.7	328.71	21.5	73.1
SA42	9/8	20° 41′ 40.204″	41° 26′ 32.991″	45.3	59.1	10.6	28.04	135.7	70.6
SA43	13/13	20° 40′ 37.939″	41° 25′ 47.953″	19	69.2	11.7	13.46	226.7	79.5
SA44	10/7	20° 40′ 22.646″	20° 40′ 22.646″	359.4	66.7	11.2	29.95	242.7	67.5

SA49	8/8	20° 39′ 55.802′′	41° 21′ 52.343′′	17.8	61.6	14.1	16.4	202.7	71.3
SA50	8/8	20° 39′ 44.341′′	41° 22′ 22.077′′	182.8	-59.4	3.6	243.9	43.2	-62.9
SA53	7/7	20° 38′ 31.818′′	41° 21′ 29.632′′	191.3	-55.7	9.6	40.40	26.0	-63.2
SA55	8/8	20° 38′ 19.800′′	41° 23′ 8.249′′	83	74.2	6.3	78.75	43.9	65.9
SA59	11/11	20° 38′ 18.665′′	41° 24′ 43.889′′	247.4	-76.5	7.3	44.63	214.4	-73.4
SA61	8/8	20° 39′ 5.051′′	41° 25′ 18.916′′	29.0	78.0	7.0	64.38	325.6	80.7
SA66	11/11	20° 37′ 39.366′′	41° 22′ 53.633′′	28.7	73.2	4.6	103.13	266.7	86.6
Mean	135/127	20° 40′ 30.000′′	41° 25′ 15.600′′	29.2	71.4	10.0	15.4	335.4	6.8
Venda Nova pluton									
VN1	8/6	20° 19′ 4.079′′	41° 9′ 27.377′′	33	72.5	6	124.43	130.0	83.7
VN2	8/6	20° 19′ 10.042′′	41° 10′ 26.672′′	24.9	70.6	5.8	132.77	169.1	81.6
VN3	10/10	20° 18′ 38.211′′	41° 10′ 52.834′′	21.1	73.7	3.1	247.07	202.7	85.7
VN4	13/13	20° 18′ 24.871′′	41° 10′ 35.416′′	21.2	69.4	2.5	277.97	181.4	79.5
VN5	9/9	20° 18′ 57.275′′	41° 12′ 17.472′′	345.5	79.7	4.4	135.19	294.4	72.7
VN6	8/8	20° 17′ 18.463′′	41° 13′ 14.549′′	17.9	75.6	6.6	71.09	252.5	86.1
VN7	14/14	20° 17′ 15.302′′	41° 13′ 17.743′′	356.6	76.7	2.1	345.05	273.5	76.9
VN8	8/7	20° 16′ 36.128′′	41° 12′ 56.959′′	27	77.3	8.6	50.60	347.8	87.4
VN9	12/12	20° 16′ 3.724′′	41° 11′ 4.764′′	50.2	71.8	1.9	500.51	91.5	76.6
VN11	14/13	20° 18′ 22.548′′	41° 9′ 30.936′′	18.5	73.4	3.1	180.19	211.5	84.5
VN15	6/6	20° 15′ 38.447′′	41° 9′ 10.300′′	30.6	74.8	5.3	158.55	113.2	87.5
VN18	5/5	20° 15′ 23.171′′	41° 8′ 43.354′′	58.5	73.8	4.8	260.21	71.3	74.6
VN22	11/11	20° 18′ 54.745′′	41° 12′ 19.573′′	0.8	81.2	4.3	111.66	310.0	76.6
VN23	11/11	20° 17′ 41.426′′	41° 12′ 27.597′	20.8	72.5	5.4	73.75	193.7	83.9
VN24	10/10	20° 17′ 48.697′′	41° 11′ 54.963′′	27.4	80.8	4.6	109.02	345.2	81.1
VN25	11/11	20° 17′ 14.265′′	41° 11′ 13.540′′	26.2	72.3	2.0	525.36	165.3	84.3
VN26	10/10	20° 17′ 41.009′′	41° 11′ 40.622′′	22.6	83.3	3.3	209.67	339.7	76.3
VN30	8/8	20° 16′ 37.925′′	41° 9′ 33.174′′	29.7	73.6	5.6	97.97	139.4	86.1
VN31	9/9	20° 16′ 23.116′′	41° 9′ 55.503′′	30.8	71.2	3.4	236.65	145.3	82.3
VN33	9/9	20° 17′ 31.640′′	41° 10′ 59.414′′	59.1	73.4	5.2	100.24	72.9	74
VN35	6/6	20° 19′ 18.177′′	41° 12′ 15.183′′	21.1	77.8	7.6	78.46	312.3	85.8
VN36	4/4	20° 18′ 25.079′′	41° 13′ 4.506′′	26.7	77.0	7.4	155.96	345.5	87.9
Mean	204/198	20° 17′ 20.400′′	41° 10′ 40.800′′	26.74	75.66	3.8	67.44	330.5	3.2
Combined poles									
Mean	37/35	20° 17’ 49.200’’	41° 29’ 6.000’’	27.8	74.2	4.2	33.1	332.2	4.7

Table 4.1. Paleomagnetic results for SA and VN plutons. The mean ChRM is given by its declination (Dec), inclination (Inc), radius of the 95% confidence cone (α95), and precision parameter (K). N/n indicates number of samples collected/used in calculation of the mean. VGP Plat/Plong indicates virtual geomagnetic pole coordinates.

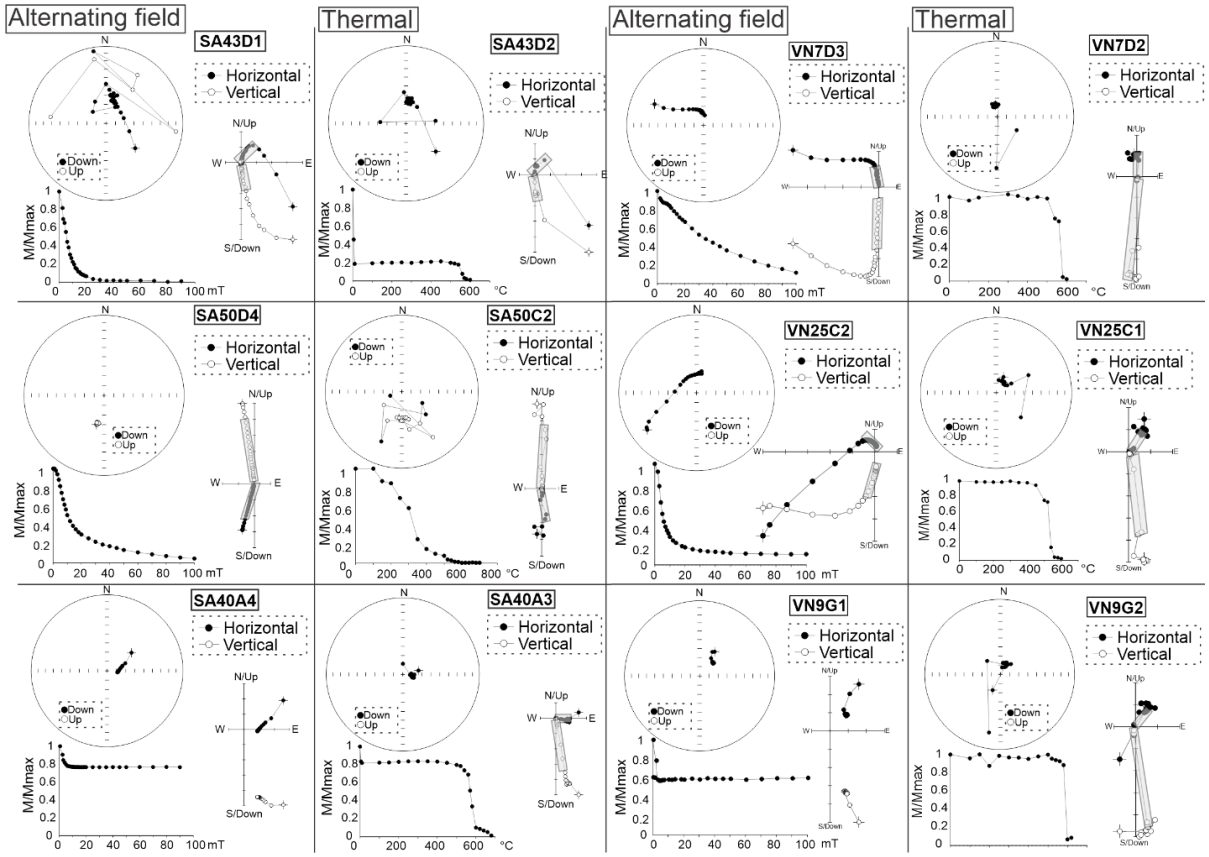

Figure 4.3 – Typical alternating field and thermal demagnetization results for Santa Angélica (SA) and Venda Nova (VN) pluton, shown as orthogonal and stereographic projections and magnetization intensity decay curves. Open (full) symbols correspond to negative (positive) inclinations in the stereographic projections.

The ChRMs of both the VN and SA plutons present two groups of directions: one directed steeply down to the NE (group 1), and a second group directed steeply up to the SW (group 2). In the VN pluton, all sites in the interior of the pluton exhibit group 1 directions, whereas seven sites located at the margin of the pluton present mixed group 1 and 2 directions (Fig. 4.4A). In the SA pluton, most sites exhibit group 1 directions, but 4 sites in the NE portion of the pluton present group 2 directions or mixed group 1 and 2 directions (Fig. 4.4B). To consider if the group 1 and group 2 directions could be antipodal (normal and reverse) components of a common population, we executed a test for a common true mean direction (CTMD; Koymans et al., 2016) after inverting the polarity of one of the groups. To consider the uncertainties associated with this test, a non-parametric bootstrap was performed following the approach described by Tauxe et al. (2010). It was not possible to perform this test on the data from the VN pluton because of the large dispersion of the group 2 directions, but application of this test to the data from the SA pluton reveals that the group 1 and group 2 directions are not

distinguishable at the 95% confidence level (Fig. 4.5A). Because these groups are antipodal, this constitutes a positive reversal test. Given this outcome, we interpret the group 1 and group 2 directions to be antipodal directions of a common population, and so treat them together in the following.

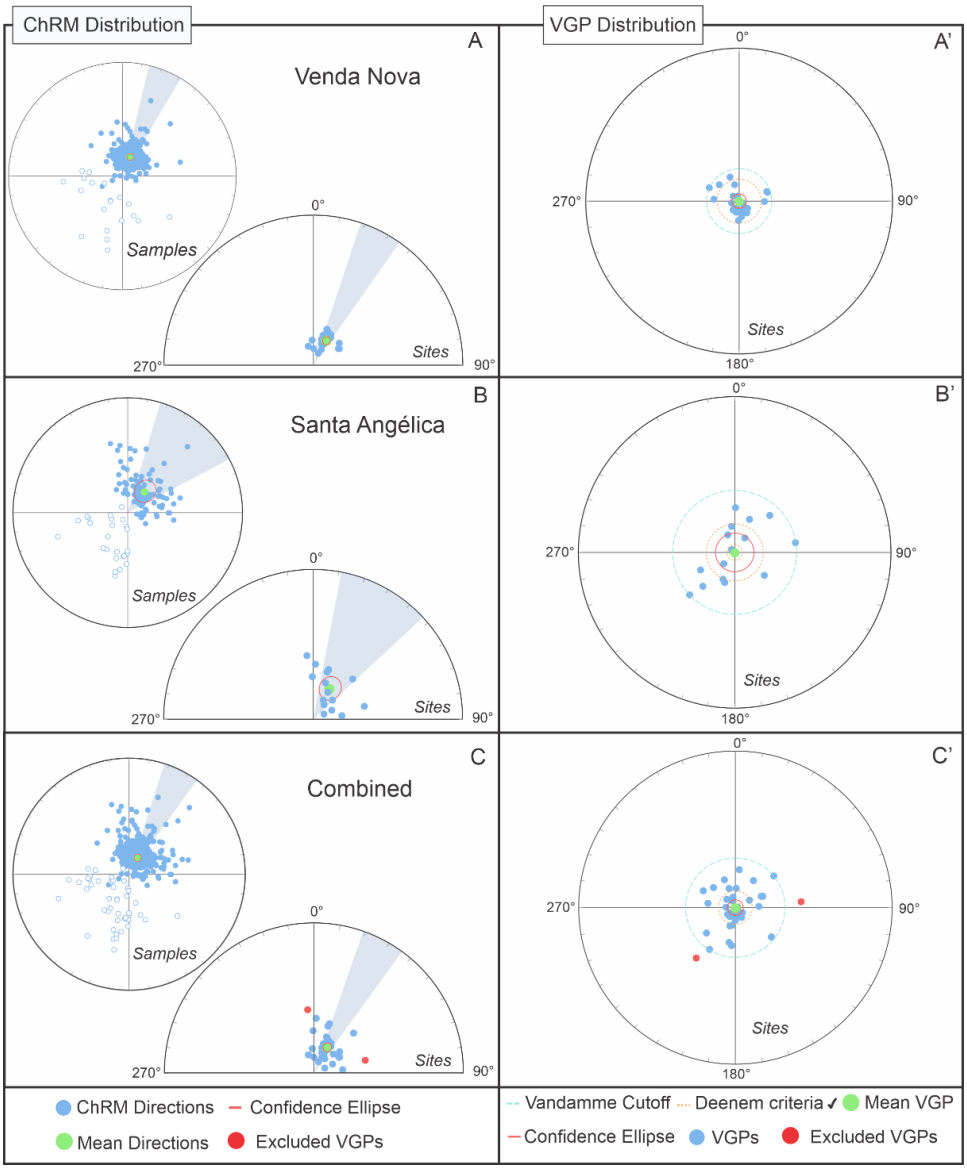

Figure 4.4 - Sample and site mean directions for the Santa Angélica (SA) and Venda Nova (VN) plutons and their corresponding VGPs. (A) ChRM directions of the VN samples and their site mean directions; (A') Relative VGP positions with the mean VGP rotated to the north pole. (B) ChRM directions of the SA samples and their site mean directions; (B') Relative VGP positions with the mean VGP rotated to the north pole. (C) ChRM directions of the combined samples and their site mean directions; (C') Relative VGP positions with the mean VGP rotated to the north pole. Filled (open) circles are projections on the lower (upper) hemisphere. Blue points are accepted, and red ones are rejected after a Vandamme cut-off (Vandamme et al., 1994). The illustrated confidence envelopes show the α95/A95 in grey shaded zone associated with the mean of the directions/VGPs. All quantitative values are reported in Table 4.1 of this work.

To consider whether the VN and SA directional populations may average paleosecular variation (PSV), we employed the approach of Deenen et al. (2011). In this approach, the A95 of virtual geomagnetic poles (VGPs) derived from a directional population are evaluated against theoretical bounding values (A95min and A95max) that are dependent on the number of observations (N); A95 values that fall between the reference bounding values are considered consistent with a population that has averaged PSV. Converting the site mean ChRM directions from VN to VGPs, we compute a mean paleomagnetic pole of 330.5 °E and 3.2 °N, with an A95 of 3.80° (Fig. 4.4A', Table 4.1). An interactive cut-off for this VGPs distribution (Vandamme et al., 1994) of 17.2° did not result in the exclusion of any sites. For N=22, A95max is 11.7° and A95min is 3.5°, and so our A95 of 3.8° falls between these values and is thus consistent with having averaged PSV. For the SA pluton, the site-based VGPs yield a paleomagnetic pole at 335.4 °E and 6.8 °N with an A95 of 10.0° (Fig. 4.4B', Table 4.1). The interactive cut-off was 32.6°, which again did not result in the exclusion of any sites. For N=15 the A95max is 14.9° and A95min 4.0°, so again our A95 falls within this envelope and is consistent with having averaged PSV.

The CTMD test was used to evaluate whether the VGPs of the VN and SA plutons could belong to the same population. Like the reversal test, the result (Fig. 4.5B) shows bootstrapped (x,y,z) coordinates for both directional populations as cumulative distribution functions. The confidence intervals for each coordinate overlap, indicating that the associated directions are statistically indistinguishable, and thus it can be concluded their populations share a common true mean direction at the 95% confidence level (Koymans et al., 2016). Since the VN and SA plutons are located only tens of kilometers apart, they are part of the same petrological suite, and their VGP populations are statistically indistinguishable, we combine their paleomagnetic data into a single pole. This combination improves the general statistical quality of the pole with a greater N. The combined paleomagnetic pole falls at 332.2° E and 4.7° N, with an A95 of 4.0° (Table 4.1). The interactive cut-off circle for the combined pole was 25.94°, which excluded two sites (Fig. 4.4C, C'). The observed A95 falls between the N=35 A95max of 8.73° and A95min of 2.89°, again indicating that the combined pole exhibits the dispersion expected from a time-averaged pole.

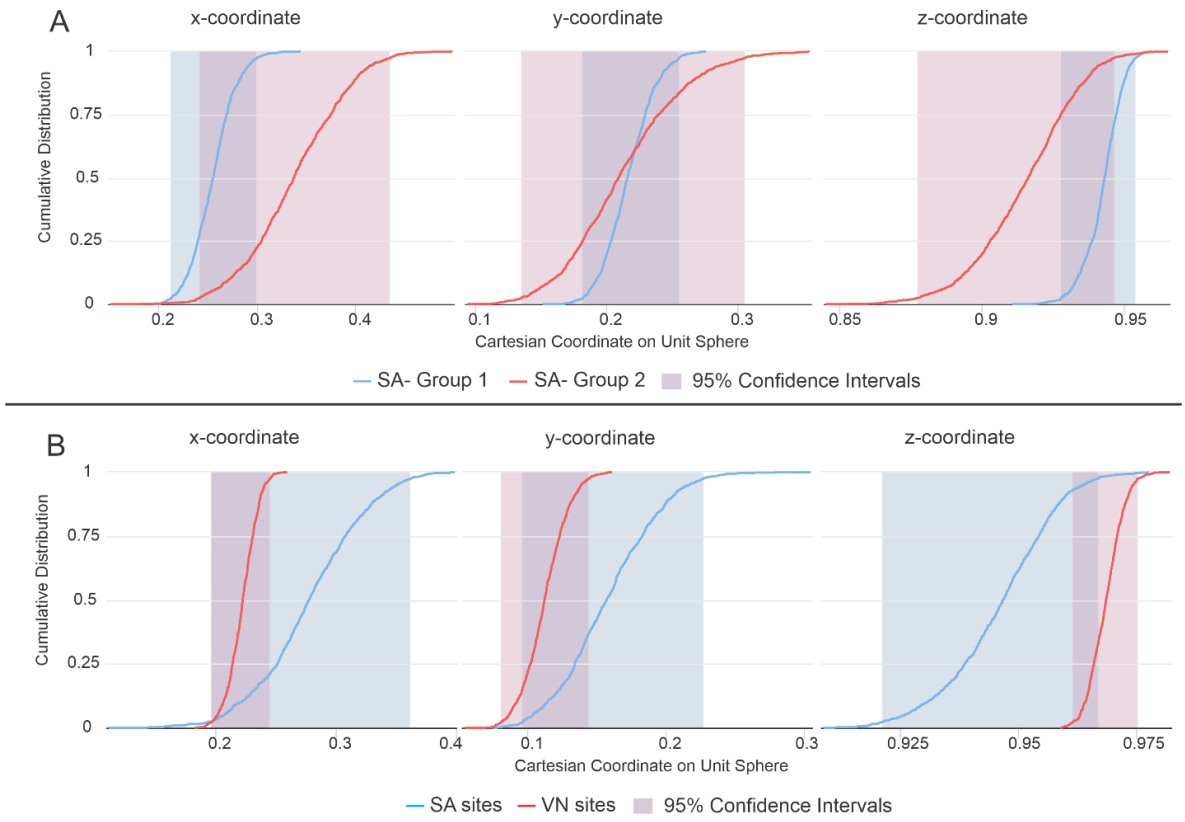

Figure 4.5. Common true mean direction (CTMD) test showing the cumulative distribution of Cartesian (x, y, and z) components of the mean directions from non-parametric bootstraps. If the confidence intervals of all components of the two sample sets overlap, they are determined to share a common true mean direction at 95% confidence. (A) CTDM test of the group 1 and 2 ChRMs of the SA pluton. (B) CTDM test of the SA and VN VGPs. Both test results reveal that the populations are indistinguishable at the 95% confidence level.

4. Thermal diffusion model

4.1. Model setup

If the magnetization preserved by the SA and VN plutons is primary, it would represent a thermoremanent magnetization (TRM) acquired during cooling of the plutons below a magnetic blocking temperature. It is therefore important to consider the thermal history of these bodies, and we thus construct a simple thermal diffusion model. To simulate the cooling process of the SA and VN plutons, a two-dimensional heat conservation equation was applied, which takes the form:

$$\left(\frac{dT}{dt}\right) = \kappa\left(\frac{\partial^2 T}{\partial x^2} + \frac{\partial^2 T}{\partial y^2}\right) + H \qquad \text{Equation (1)}$$

Assuming the term κ (thermal diffusivity)= (k ρ-1Cp-1), where ρ is the density of the material (kg m-3), Cp is the thermal capacity at a constant pressure (J / Kg / K), k is the thermal

conductivity (W/m/K) and H is the volumetric heat production (Wm-3). The terms accompanied by κ are the second derivative of the temperature of the medium, i.e., the temperature variation in the x and y directions. For most mantle and crustal rocks, radioactive heat only becomes relevant at temperatures above 1200 °C (Clauser, 2009), and as such, we ignored the heat production in Eq. (1). As Eq. (1) is a differential equation, it was solved numerically using a finite-difference method in a python script environment. Further details of this thermal diffusion model can be found in the appendix C.

In the case of the VN pluton, we directly simulated the initial matrix of T0 (the initial state, i.e, its emplacement) undergoing diffusion for 3 Ma. As proposed by Temporim et al. (2020), the SA pluton consists of two plutonic features, a SW and a NE lobe, separated by an internal magmatic shear zone. Therefore, two different scenarios were proposed for SA: a) these two plutons intrude at the same time with the same T0 and undergo heat diffusion for 3 Ma; b) the shallowest pluton (the NE lobe) intrudes first, cools down and then the SW pluton intrudes the nearby wall rocks. In scenario (b), the cooling process of the earlier NE pluton and its host was alternatively simulated for 100 kyr and 1 Ma prior to intrusion of the SW pluton, to investigate the differences associated with an approximately coeval intrusion versus a late emplacement. After the intrusion of the SW body, heat diffusion was simulated for an additional 3 Ma.

4.2. Model results

Given the presence of antipodal directions, one way to assess whether the magnetizations could be primary is to consider if the observed spatial distribution of the two polarities could be explained by cooling of the plutons. Thus, our thermal diffusion model can here serve as a kind of field stability test (Van der Voo, 1990; Meert et al., 2020). As discussed below, the results of our model indeed demonstrate that the spatial distribution of magnetic polarity can be related to cooling of the plutons, and thus the magnetization may be primary. The full details of the diffusion model used to draw this conclusion can be seen in the appendix C. In the following, we focus on the heat transfer pattern for each scenario and its relationship with the antipodal directions from each pluton (Fig. 4.6A, B).

In the VN pluton, heat diffusion occurs quickly through the first 100 kyr, in accordance with Fick's first law of diffusion. The gabbroic core transfers energy to the lower temperature syenite-monzonite envelope, and the highest temperature isotherms migrate from the gabbroic core to the center of the unit within 150 kyr. Before migration and re-setting of the hottest region of the pluton, the 600°C and 500°C isotherms are close together. Once the diffusion

takes an equal spreading regime from 150 kyr forward, these isotherms depart from each other. The polarities of the VN sites also exhibit a concentric distribution, with group 2 directions and mixed polarities located at the border of the pluton, and group 1 directions located at the core. Considering a range of magnetite Curie temperature (Tc) coherent with the 600°C isotherm and 500°C as a blocking temperature (Tb), and comparing it with the spatial distribution of the paleo-polarity at each site, it is possible to observe a coherent correlation, represented by the 375 kyr interpolation frame (Fig. 4.6C).

For the SA pluton, the same perspective between mafic core vs felsic envelope in the VN is observed. There is a difference in the thermal interaction between the NE and SW pluton. Both plutons are approximately coeval (Temporim et al., 2020), and our alternative thermal history scenarios (100 kyr vs. 1 Ma differences in emplacement timing) are simply formulated for the sake of comparison. The matter of which lobe would have intruded first is not relevant, because the goal is to determine whether the polarity could be related to the cooling process, and thus whether the magnetization could be primary. In the NE lobe, following 100 kyr of cooling, the 500°C and 600°C isotherms are close together and there is a hot core with temperatures near 900°C. In the SW intrusion, the heat causes a funneling effect of the isotherms towards the NE lobe and, once the heat distribution is equilibrated, isotherms depart again with a much lower cooling rate. In the 1 Ma cooling scenario, the NE lobe fully passes through Tb before the intrusion of the SW lobe. The funneling effect is also present and 500°C isotherms expands itself through a NE trend until nearly half of the NE body. Although with small differences between each other, in both scenarios the 500°C and 600°C isotherms are coherent with the paleo-polarity distribution in the SA - all sites that exhibit group 2 or mixed group 1 and 2 directions are located in the NE lobule and the SW lobule exhibits only group 1 directions (Fig. 4.6D,E).

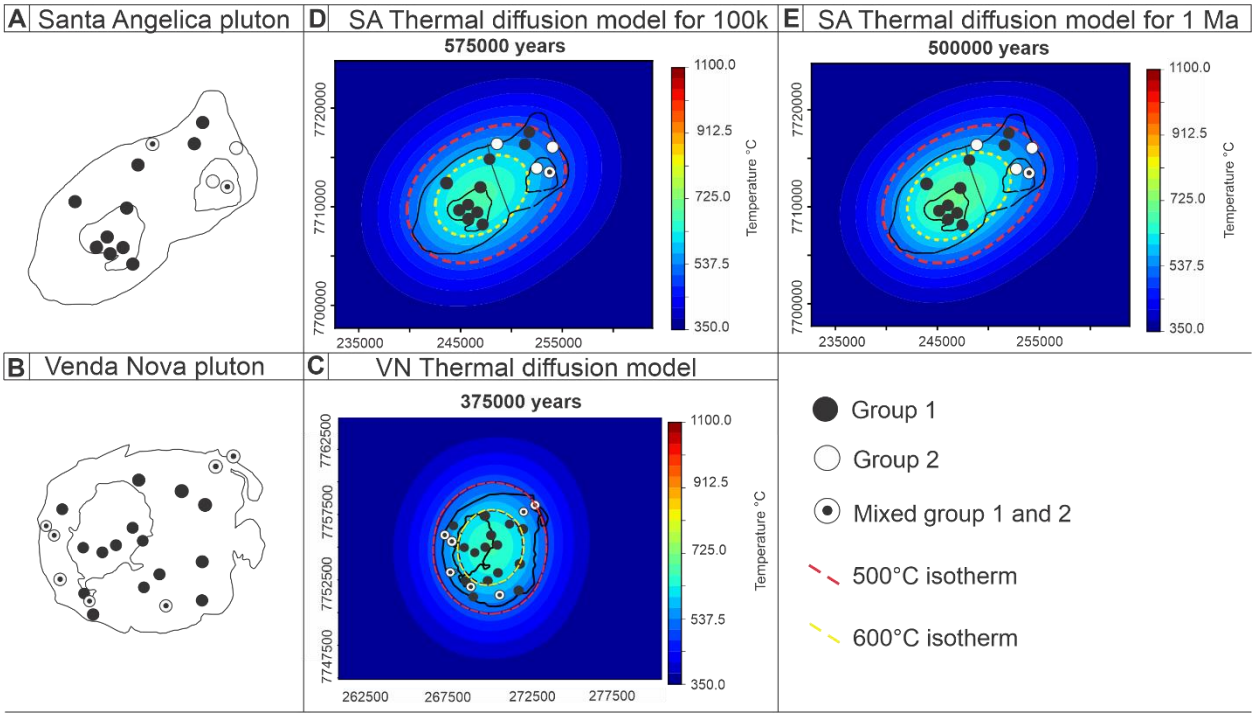

Figure 4.6 – Thermal diffusion model for the SA (A) and VN (B) plutons and the distribution of observed paleomagnetic polarities. (C) VN thermal diffusion model frame. (D) and (E) SA thermal diffusion model frame for 100k years and 1Ma, respectively.

5.Discussion

5.1. Paleomagnetic pole of the Cambrian plutons

Our paleomagnetic analysis revealed antipodal remanent magnetizations from both the SA and VN plutons, which pass a reversal test and represent indistinguishable directional populations, as attested by a CTDM test. In conjunction with our thermal diffusion models, the observed distribution of magnetic polarities is consistent with the ChRMs of the SA and VN plutons being thermoremanent magnetizations (TRMs) acquired during cooling of those plutons following their emplacement. That the A95 of the SA pluton is larger than that of the VN pluton is mostly likely due to their different cooling histories. According the thermal diffusion model, the amount of time to cool the SA pluton required ~600 kyr more than the VN pluton. Due the longer cooling time, SA pluton would record greater dispersion of directional data. Nevertheless, the directional dispersion of the VN data is still within the expected range for a time-averaged pole, and the presence of dual polarities strongly suggests that the dataset has averaged PSV.

Both plutons are part of a set of post-collisional plutons emplaced in a cold crust free of tectonic stresses (Fig. 4.1). These plutons were emplaced through large shear zones that were generated in the collision period and later inactive in the post-collisional stage (Alkmin et al., 2006, De Campos et al., 2016). There is a coherence between the directions observed in the plutons, even though they are separated by shear zones. Furthermore, concentric magnetic fabric obtained for the SA (Temporim et al., 2020) and VN shows a plunging angle increasing from the cores to the borders of plutons. The gradual contact between the intrusion and the country rock are subvertical and the foliation at the border of the SA and VN plutons is parallel to the contact with the country rocks. There is absence of spread internal solid-state deformation in the inner portion of the plutons. Such patterns are further evidence that the current spatial position of both plutons remain the same since its intrusion - lacking of any indications of either rotation or tilting.

Combination of the results from both plutons yields a paleomagnetic pole (hereafter 'SAVN' pole) at 332.2 °E and 4.7 °S (Table 4.1) for which an age of ~500 Ma is assigned based on the U-Pb analysis (Temporim et al., 2020). This pole completely satisfies all seven quality criteria proposed by Van der Voo (1990), as follows: (1) U-Pb zircon ages constraining the crystallization age of different facies within SA pluton are concordant and likely closely approximate the age of magnetization acquisition; (2) the pole was derived from a set of 309 samples (35 sites) and has adequate statistical precision (A95=4.06 and K=68.82); (3) remanence vectors were isolated after stepwise AF and TH demagnetization, both treatments giving similar results; (4) a thermal diffusion model was used to attest that the magnetization in both plutons is most likely a primary TRM; (5) the plutons intrude Neoproterozoic gneisses of the AO after the peak of deformation and metamorphism, as indicated by regional geochronological data and structural relations (details can be found in Temporim et al., 2020); (6) the Santa Angelica pluton presents reversals corroborated by a positive reversal test; (7) the pole does not resemble any younger paleomagnetic poles either from Gondwana or the independent South American plate after the demise of Pangea. The location of the SAVN pole is moreover similar to other ~500 Ma poles from Gondwana (see below). Meert et al. (2020) introduce a stricter (updated) R-criteria, but our new pole also completely satisfies their seven criteria. In sum, our new paleomagnetic pole may be regarded as a reference pole for the supercontinent Gondwana in Furongian time (~500 Ma).

The paleomagnetic data from this work also suggest that the Earth's magnetic field underwent at least one period of reversal during the acquisition of the remanence in these rocks.

Moreover, because Gondwana was in the southern hemisphere during the early Paleozoic (see below), we may recognize the group 1 directions (directed downward) as being of reverse polarity and the group 2 directions as being of normal polarity.

5.2. Comparisons with existing constraints

Several apparent polar wander paths (APWP) have been proposed for Gondwana in latest Neoproterozoic-early Paleozoic time (e.g. Meert et al., 2003, Trindade et al., 2006, Torsvik et al., 2012, Rapalini et al., 2018). These paths are based on different data selection and rejection criteria, resulting in a large variety of shapes. For reference, in Fig. 4.7 we show the Paleozoic segment of the Gondwana APWP of Torsvik et al., 2012 (one of the larger and more recent compilations), rotated into South American (Amazonian) coordinates. More specifically, this is the 10-Myr running mean (RM) path of Torsvik et al. (2012); a variation of this path that applies a blanket inclination shallowing correction (f=0.6) to all uncorrected clastic sedimentary rocks is also depicted (dashed line). Note that although this Paleozoic APWP is built from a relatively large number of poles (N=74), they are not uniformly distributed in time. Mean poles with a white A95 are based on only a single entry (whereas all means with a blue A95 have N > 1), and the poles at 340, 420 and 430 Ma (marked by grey squares) are interpolated (i.e. N=0).

Our new 500 Ma SAVN pole (Table 4.1) closely corresponds to the Furongian sector of this Gondwana APWP, and notably falls within the A95 of both the 500 and 510 Ma mean poles (Fig. 4.7). Aside from the Furongian segment, the only other part of the APWP of Gondwana that is somewhat close to the SAVN pole is the 390 Ma mean pole (10 °N, 15 °E). However, this 390 Ma mean is poorly defined, being based on only a single pole derived from sedimentary rocks that have not been corrected for inclination shallowing. Torsvik et al. (2012) discarded this pole in favor of an interpolated result (grey 390 Ma pole in Fig. 4.7), and, notably, application of an assumed inclination shallowing correction of f=0.6 results in a shift of the original mean toward this interpolated position.

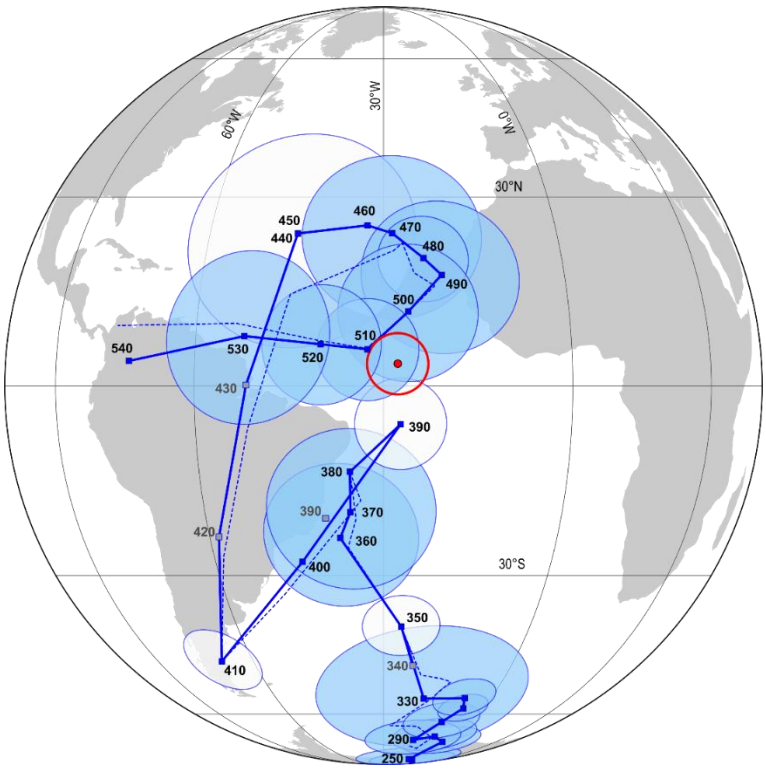

Figure 4.7 – Apparent Polar Wander Path (APWP) of Gondwana (Torsvik et al., 2012) in Amazonian coordinates. The solid line represents the 10-Ma running mean path (using a 20-Ma window) without correction for potential inclination shallowing; the dashed line is the same path after inclination shallowing correction with a blanket value of f=0.6. Mean poles with a white A95 are based on only a single entry (whereas all blue A95s have N > 1). Mean poles denoted by grey squares (430, 420, 390 and 340 Ma) were determined by interpolation from the neighboring mean poles. The SAVN pole is shown in red.

Although the comparison of the SAVN pole against the reference Gondwana APWP of Torsvik et al. (2012) is instructive, it is also important to directly compare it against similarly aged individual poles. This is especially important given the fact that the Cambrian Epoch 2-Tremadocian segment of the Gondwana APWP of Torsvik et al. (2012) is near-entirely dominated by results from Eastern Gondwana. Of the 19 late Cambrian Epoch 2-Tremadocian (530-480 Ma) poles from Gondwana in that compilation, ten are from Australia, four are from Antarctica and two are from Madagascar. The remaining three poles are from southeastern Africa and the Rio de la Plata Craton, and there are no Cambrian Epoch 2-Tremadocian (poles from Congo-São Francisco. We therefore compiled Cambrian Epoch 2-Tremadocian (525-480 Ma) poles from Western Gondwana (Table 4.2) to evaluate the position of SAVN with respect to coeval poles from more closely neighboring regions. In addition to the aforementioned poles from Torsvik et al. (2012), our compilation includes three poles from Congo-São Francisco and two poles from the Pampean Orogen. We sought poles with Q > 4, but retained the singular pole from Rio de la Plata with Q=3.

Code	Formation	Q	Plat	Plon	A_{95}	Age	EP	Reference
Congo-São Francisco								
SAVN	Santa Angelica/Venda Nova plutons, Araçuai Orogen	7	4.7	332.2	4.1	500	-	This work
PI	Piquete Formation, Ribeira-Araçuai Orogen	4	-0.8	346.5	10.2	500	-	D`Agrella and Pacca (1986)
JF	Juiz de Fora Complex	4	-0.6	335.2	10	510	-	D`Agrella et al. (2004)
IT	Itabaiana Dikes, Borborema Province	6	-34.9	134.6	7.3	525	-	Trindade et al. (2006)
Rio de la Plata								
SI	Sierra de las Animas volcanic Complex	3	5.9	338.1	18.1	510	[8.4, 111.2, -2.6]	Sánchez-Bettuccia and Rapalini (2002)
Pampean Orogen								
LP	La Pedrera Formation	5	38.3	340.4	8.8	485-477	[7.7, 298.5, 3.3]	Rodríguez Piceda et al. (2018)
CF	Campanario Formation	7	23.6	346.5	7	514-485	[7.7, 298.5, 3.3]	Franceschinis et al. (2020)
Southeastern Africa								
GF	Graafwater Formation, Cape Province	6	28	14	9	482.5	[50.0, -32.5, -55.1]	Bachtadse et al. (1987)
NR	Ntonya Ring Structure, Malawi	5	27.5	344.8	1.9	522	[50.2, 327.7, -55.0]	Briden, J., (1968)

Table 4.2. Selected paleomagnetic poles for Gondwana between 525 and 480 Ma. Q = Quality Factor (Van der Voo, 1990); A95=95% confidence ellipse; Lat/Lon = Pole Latitude/Longitude; Age in Ma. Figures in brackets represent values of rotation into Amazonia reference frame.

In Fig. 4.8 we plot the SAVN pole against these other poles after rotating them to South American (Amazonian) coordinates, following the reconstruction parameters of Torsvik et al. (2012) (see Table 4.2). Among these poles, the results from the Piquete Formation (PI, ca.500-490 Ma, D'Agrella Filho et al., 1986) and Juiz de Fora (JF, ca.510-500 Ma, D'Agrella et al., 2004) are the most directly comparable to SAVN, in being the only other poles from the Araçuaí orogen. JF lies only ~6° from SAVN and its A95 overlaps the SAVN mean, whereas the PI pole falls ~15° from SAVN and is statistically distinct from it. Although the first-order similarity among these pole positions is noteworthy, an interpretation of their differences is inhibited by the fact that the PI and JF poles are derived from metamorphic rocks whose ages are not precisely determined. Aside from the PI and JF poles, the only other similarly aged pole from Congo-São Francisco is the Itabaiana pole (IT, ca. 525 Ma; Trindade et al. 2006), which falls ~34° from SAVN. However, given that the best-estimated ages of these poles differ by ~25 Ma, their separation could be simply explained by plate motion at a rate on the order of 15 cm yr^{-1}.

Looking beyond Congo-São Francisco, the Cambrian Epoch 2 pole from Rio de la Plata (SI) falls close to (~6° from) the SAVN mean, but is associated with large spatial and temporal uncertainties. A Tremadocian pole from South Africa (Graafwater, GF pole) also falls ~10° from the SAVN mean, whereas the Cambrian Epoch 2 Ntonya Ring pole (NR) from southeastern Africa lies ~24° away. Observing that the latter falls close to the IT pole (Trindade et al. 2006), its position is again possibly reflective of the Cambrian Epoch 2 drift of Western Gondwana. These results are thus consistent with a general coherence between Congo-São Francisco, Rio de la Plata and southern Africa by Cambrian Epoch 2 time. In contrast, two Furongian-Tremadocian poles from the Pampean orogen fall more than 25° from SAVN and the other Furongian-Tremadocian poles from Western Gondwana (Franceschinis et al. 2020). Their pole positions are also significantly offset from the coeval mean poles of the APWP of Torsvik et al. (2012). Their anomalous positions could be interpreted as evidence of a significant younger displacement of the Pampean orogen with respect to greater Gondwana (e.g. Spagnuolo, et al., 2012), although the available geological evidence strongly opposes such a scenario (Rapela et al., 2007; Ramos et al., 2010). This remains an outstanding problem.

A key observation from these comparisons is that our ~500 Ma SAVN pole agrees well with the Gondwana APWP of Torsvik et al. (2012), which is dominated by Eastern Gondwana data, and with individual Terreneuvian-Tremadocian poles from Western Gondwana. This implies that Eastern and Western Gondwana must have been approximately coherent at least by this time. In contrast, the slightly older Cambrian poles (Cambrian Epoch 2) from Western Gondwana (IT and NR) appear to diverge from the Terreneuvian and Cambrian Epoch 2 trend of the Gondwana APWP of Torsvik et al. (2012) (Fig. 4.8), implying that Western and Eastern Gondwana may have still been moving relative to one another immediately prior to mid-Cambrian time (Robert et al. 2018).

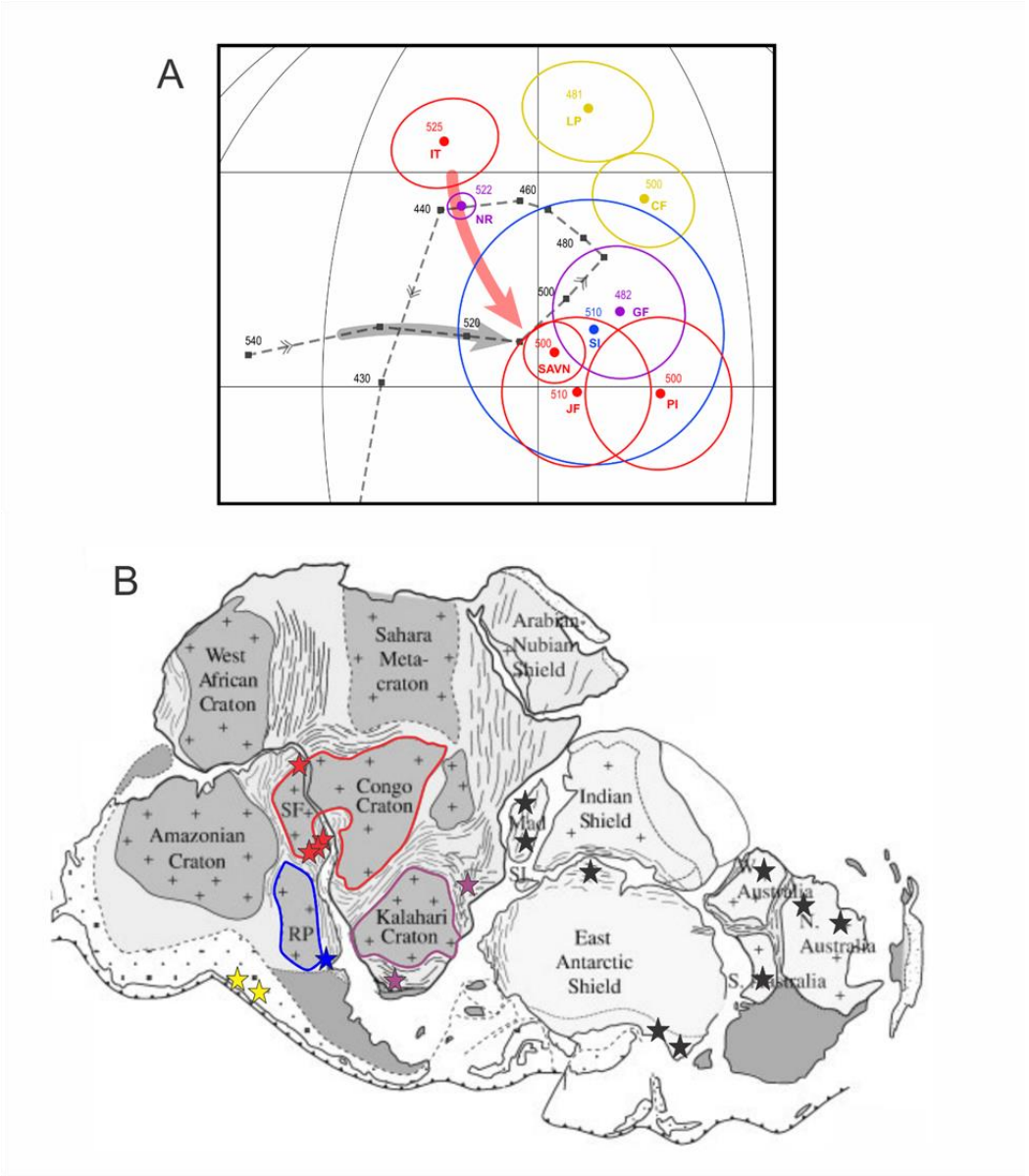

Figure 4.8. Cambrian Epoch 2 to Tremadocian paleomagnetic poles of Gondwana. A) Poles rotated to the Amazon coordinates following the reconstruction parameters of Torsvik et al. (2012). The collection includes poles from Congo-São Francisco craton (red), Pampean Orogen (yellow), Rio de la Plata (blue), and Southeastern Africa (purple). All information and references of the poles can be seen in the Table 4.2 of this work. APWP for Gondwana between 540–430 is represented in dashed gray lines (Torsvik et al., 2012). B) Gondwana map (Gray et al., 2007) with localities from Western Gondwana in colorful stars and localities from Eastern Gondwana in black stars.

6. Conclusions

Paleomagnetic analysis was conducted on the post-collisional Santa Angélica and Venda Nova plutons (~500 Ma) from the southern portion of the Araçuaí orogen (AO) in SE Brazil. The results of this analysis isolated a characteristic magnetization likely carried by PSD/SD magnetite grains, as determined from a series of rock magnetic experiments. The population of

magnetic directions from both plutons are associated with two groups which, for the Santa Angelica pluton, are demonstrated to be antipodal. A thermal diffusion model was used to demonstrate that the magnetization in both plutons is consistent with a primary thermoremanent magnetization, acquired in the midst of a field reversal. The SAVN pole computed from the pooled magnetic results (4.7° N, 332.2° E, N=35, A95=4.0° and K=68.8) does not resemble any younger paleomagnetic poles either from Gondwana or the independent South American plate after the demise of Pangea. In sum, this pole completely satisfies all seven quality criteria proposed by Van der Voo (1990), as well as the stricter (updated) R-criteria proposed by Meert et al. (2020).

The SAVN pole closely corresponds to the Miaolingian-Furongian sector of the Gondwana APWP (Torsvik et al., 2012), and notably falls within the A95 of both the 500 and 510 Ma mean poles of that path. The Terreneuvian-Tremadocian segment of the Gondwana APWP of Torsvik et al. (2012) is near-entirely dominated by results from Eastern Gondwana. The few poles from Western Gondwana are from southeastern Africa and the Rio de la Plata Craton, and there are no Terreneuvian-Tremadocian poles from Congo-São Francisco; our new pole therefore provides a critical new constraint from this block in the core of Western Gondwana. In comparing our SAVN pole with individual Cambrian Epoch 2-Tremadocian poles from Western and Eastern Gondwana, we may conclude that Eastern and Western Gondwana appear to share a common population of paleomagnetic poles by Furongian time (~500 Ma), but that there are paleomagnetic indications of strong motions between those blocks in earlier Terreneuvian-Cambrian Epoch 2 time.

Acknowledgments

The authors would like to express their gratitude to the Laboratório de Paleomagnetismo (USPmag) of the Universidade de São Paulo. This works was funded by grants of Fundação de Amparo à Pesquisa do Estado de São Paulo (FAPESP, #2016/06114-6, #2017/11672-0 and # 2019/18892-1). The opinions, hypotheses and conclusions or recommendations expressed in this material are the authors' responsibility and do not necessarily reflect FAPESP's vision. We also thank the fellowship provided by the Coordenação de Aperfeiçoamento de Pessoal de Nível Superior -Brasil (CAPES), Finance Code 001. This work was also supported by the Research Council of Norway (RCN) through its Centres of Excellence funding scheme, project 223272 (CEED) and through RCN project 250111. We thank the reviewers for constructive comments that greatly improved the manuscript.

References

Alkmim, F.F., Marshak S., Pedrosa-Soares A.C., Peres G.G., Cruz S.C.P., Whittinton A. (2006). Kinematic evolution of the Araçuaí-West Congo orogen in Brazil and Africa: nutcracker tectonics during the Neoproterozoic assembly of Gondwana. *Precambrian Research*. 149, 43-64. https://doi.org/10.1016/j.precamres.2006.06.007.

Bachtadse, V., Van der Voo, R., Hilbich, I.W. (1987). Paleomagnetism of the western Cape Fold belt, South Africa, and its bearing on the Paleozoic apparent polar wander path for Gondwana. *Earth and Planetary Science Letters*. 84: 487-499.

Bayer B., Schimidt-Thomé R., Weber-Diefenbach K., Horn H.A. (1987). Complex concentric granitoid intrusions in the coastal mobile belt, Espírito Santo, Brazil: the Santa Angélica Pluton – an example. *Geologische Rubdschau*. 76(2). 357-371. 10.1007/BF01821080.

Briden, J. (1968). Paleomagnetism of the Ntonya Ring Structure, Malawi. *Journal of Geophysical Research*. 73: 725-733.

Clauser, C. (2009). Heat transport processes in the earth's crust. *Surveys in Geophysics*. 30: 163–191. https://doi.org/10.1007/s10712-009-9058-2

D'Agrella Filho, M.S., Raposo, M.I.B., Egydio-Silva, M. (2004). Paleomagnetic Study of the Juiz de Fora Complex, SE Brazil: implications for Gondwana. *Gondwana Res*. 7, 103–113. https://doi.org/10.1016/S1342-937X(05)70309-9.

D'Agrella Filho, M.S., Pacca, I.G. (1986). Paleomagnetism of metamorphic rocks from the Piquete region – Ribeira Valley, Southeastern Brazil. *Rev. Brasileira de Geofisica*. 4: 79-84.

De Campos C.M., Medeiros, S. R., Mendes J.C., Pedrosa-Soares, A. C., Dussin, I., Ludka, I. P., Dantas, E. L. (2016). Cambro-Ordovician magmatism in the Araçuaí Belt (SE Brazil): Snapshots from a post-collisional event. *Journal of South American Earth Sciences*. 68, 248-268. https://doi.org/10.1016/j.jsames.2015.11.016.

Deenen, M.H.L., Langereis, C.G., van Hinsbergen, D.J.J., Biggin,A.J. (2011). Geomagnetic secular variation and the statistics of palaeomagnetic directions. *Geophys. J. Int*. 186(2), 509–520. https://doi.org/10.1111/j.1365-246X.2011.05050.x.

Dunlop, D.J., Argyle, K.S. (1991). Separating multidomain and single-domain-like remanences in pseudo-single-domain magnetites (215–540 nm) by low-temperature demagnetization. *Solid Earth*, 96, 2007-2017. https://doi.org/10.1029/90JB02338.

Fisher, R. A. (1953). Dispersion on a sphere. *Proc. R. Soc. London*. A217, 295–305. https://doi.org/10.1098/rspa.1953.0064.

Franceschinis, P.R., Rapalini, A,E., Escayola, M.P., Picedad, C.R. (2020). Paleogeographic and tectonic evolution of the Pampia Terrane in the Cambrian: New paleomagnetic constraints. *Tectonophysics*. 779, 228386. https://doi.org/10.1016/j.tecto.2020.228386.

Kirschvink, J.L. (1980). The least-squares line and plane and the analysis of palaeomagnetic data. *Geophysical Journal International*. 62(3), 699–718. https://doi.org/10.1111/j.1365-246X.1980.tb02601.x

Koymans, M.R., Langereis, G.C., Pastor-Galán, D., van Hinsbergen, D.J.J. (2016). Paleomagnetism.org: An online multi-platform open source environment for paleomagnetic data analysis. *Computers & Geosciences*. 93, 127–137. http://dx.doi.org/10.1016/j.cageo.2016.05.007.

Kröner, A., Stern, R.J. (2005). Africa: Pan-African Orogeny. Encyclopedia of Geology, vol. 1, Elsevier, Oxford (2005), pp. 1-13.

Li, Z.-X., Evans, D.A.D. & Halverson, G.P. (2013). Neoproterozoic glaciations in a revised global palaeogeography from the breakup of Rodinia to the assembly of Gondwanaland. *Sedimentary Geology*, 294, pp.219–232.

Meert, J.G., Van der Voo, R. (1997). The assembly of Gondwana 800–550 Ma. *Journal of*

Geodynamics 23, 223–235. https://doi.org/10.1016/S0264-3707(96)00046-4.

Meert, J.G., Nédélec, A., Hall, C. (2003). The stratoid granites of central Madagascar: paleomagnetism and further age constraints on neoproterozoic deformation. *Precambrian Research*. 120, 101-129. https://doi.org/10.1016/S0301-9268(02)00161-4

Meert, J.G., Pivarunas, A.F., Evans, D.A.D., Pisarevsky, S.A., Pesonen, L.J., Li, Z.X., Elming, S.A., Miller, S.R., Zhang, S., Salminen, J.M. (2020). The magnificent seven: A proposal for modest revision of the Van der Voo (1990) quality index. *Tectonophysics*. 790, 228549. https://doi.org/10.1016/j.tecto.2020.228549.

Mendes, J.C., De Campos, C.M.P. (2012). Norite and charnockites from the Venda Nova Pluton, SE Brazil: Intensive parameters and some petrogenetic constraints. *Geoscience Frontiers*. 3(6), 789-800. https://doi.org/10.1016/j.gsf.2012.05.009.

Munhá, J. M. U., Cordani, U., Tassinari, C. C. G., Paácios, T. (2005). Petrologia e termocronologia de gnaisses migmatíticos da Faixa de Dobramentos Aracuaí (Espírito Santo, Brasil): *Revista Brasileira de Geociencias*, v. 35, p. 123–134. 10.25249/0375-7536.2005351123134

Pedrosa-Soares A.C., Wiedemann-Leonardos C.M. (2000). Evolution of the Araçuaí belt and its connection to the Ribeira Belt, Eastern Brazil. In: U.G. Cordani, E.J. Milani, A. Thomaz Filho, D.A. Campos (Eds.) Tectonic Evolution of South America. São Paulo, SBG, 265-285.

Pedrosa-Soares, A.C., Noce, C.M., Wiedemann, C.M., Pinto, C.P. (2001). The Araçuaí-West Congo orogen in Brazil: An overview of a confined orogen formed during Gondwanland assembly. *Precambr. Res*. 110, 307–323. https://doi.org/10.1016/S0301-9268(01)00174-7

Pedrosa-Soares, A.C., De Campos, C.P., Noce, C.M., Silva, L.C., Novo, T., Roncato, J., Medeiros, S., Castaneda, C., Queiroga, G., Dantas, E., Dussin, I., Alkmim, F.F. (2011). Late Neoproterozoic-Cambrian granitic magmatism in the Araçuaí orogen (Brazil), the eastern Brazilian Pegmatite province and related Mineral resources. In: Sial, A.N., Bettencourt, J.S., De Campos, C.P., Ferreira, V.P. (Eds.), Granite related Ore Deposits, 350. Geological Society, London, pp. 25e51. Special Publications.

Pollock, J.C., Hibbard, J.P., van Staal, C.R. (2012). paleogeographical review of the peri-Gondwanan realm of the Appalachian orogen. *Canadian Journal of Earth Sciences*, 40: 1-30. doi:10.1139/E11-049

Ramos, V.A., Vujovich, G., Martino, R., Otamendi, J. (2010). Pampia: a large cratonic block missing in the Rodinia supercontinent. *J. Geodyn*. 50, 243–255. https://doi.org/10.1016/j.jog.2010.01.019.

Rapalini, A.E. (2018). Assembly of Western Gondwana reconstruction based on paleomagnetic data. In S. Siegesmund, M. Basei y P. Oyantzabal (Eds.), "Geology of Southwest Gondwana". Springer-Verlag, pp. 3-18. DOI: 10.1007/978-3-319-68920-3_1.

Rapela, C.W., Pankhurst, R.J., Casquet, C., Fanning, C.M., Baldo, E.G.A., González-Casado, J.M., Galindo, C., Dahlquist, J. (2007). The Río de la Plata craton and the assembly of SW Gondwana. *Earth Sci. Rev*. 83, 49–82. https://doi.org/10.1016/j.earscirev.2007.03.004.

Robert, B., Greff-Lefftz, M., Besse, J. (2018). True Polar Wander: A Key Indicator for Plate Configuration and Mantle Convection During the Late Neoproterozoic. *Geochemistry, Geophysics, Geosystems*. 19, 3478–3495. DOI: 10.1029/2018GC007490.

Rodríguez Piceda, C., Franceschinis, P.R., Escayola, M.P., Rapalini, A.E. (2018). Paleomagnetismo del Grupo Santa Victoria en la sierra de Mojotoro, Salta: aportes a la reconstrucción paleogeográfica de Pampia en el Paleozoico Temprano. *Revista de la Asociacion Geologica Argentina*. 4: 518–532. https://doi.org/10.1016/j.psep.2018.03.001.

Sanchez-Bettucci, L., Augusto E. Rapalini, A.E. (2002). Paleomagnetism of the Sierra de Las Animas Complex, southern Uruguay: its implications in the assembly of western Gondwana. *Precambrian Research*. 118: 243-265.

Schmidt-Thomé R., Weber-Diefenbach K. (1987). Evidence for frozen-in magma mixing in Brasiliano calc-alkaline intrusions. The Santa Angélica pluton, southern Espírito Santo, Brazil. *Revista Brasileira de Geociências*. 17, 498-506.

Spagnuolo, C.M., Rapalini, A.E., Astini, R.A. (2012). Assembly of Pampia to the SW Gondwana margin: A case of strike-slip docking?. *Gondwana Research*. 21? 406–421.

Tauxe, L., Butler, R.F., Van der Voo, R., Banerjee, S.K. (2010). Essentials of Paleomagnetism. University of California Press, California, ISBN:9780520260313.

Tedeschi, M., Novo, T., Pedrosa-Soares, A., Dussin, I., Tassinari, C., Silva, L.C., Dantas, E. (2016). The Ediacaran Rio Doce magmatic arc revisited (Araçuaí-Ribeira orogenic system, SE Brazil). *J. S. Am. Earth Sci*. 68, 167–186. http://dx.doi.org/10.1016/j.jsames.2015.11.011.

Temporim, F.A., Trindade, R.I.F., Tohver, E., Soares, C.C., Gouvêa, L.P., Egydio-Silva, M., Amaral, C.A.D., Souza Jr., G.F. (2020). Magnetic Fabric and Geochronology of a Cambrian "Isotropic" Pluton in the Neoproterozoic Araçuaí Orogen. *Tectonics*. 39(6), e2019TC005877. https://doi.org/10.1029/2019TC005877.

Tohver, E.; D'agrella Filho, M.S.; Trindade, R.I.F. (2006). Paleomagnetic record of Africa and South America for the 1200-500 Ma interval, and evaluation of Rodinia and Gondwana assemblies. *Precambrian Research*, 147, 193-222.

Tohver, E., Cawood, P.A., Rossello, E.A., Jourdan, F. (2012). Closure of the Clymene Ocean and formation of West Gondwana in the Cambrian: Evidence from the Sierras Australes of the southernmost Rio de la Plata craton, Argentina. *Gondwana Research*. 21, 394–405. 10.1016/j.gr.2011.04.001.

Trindade, R.I.F., D'Agrella-Filho, M.S., Epof, I., Brito Neves, B.B. (2006). Paleomagnetism of Early Cambrian Itabaiana mafic dikes (NE Brazil) and the final assembly of Gondwana. *Earth and Planetary Science Letters*. 244, 361–377. https://doi.org/10.1016/j.epsl.2005.12.039.

Torsvik, T.H., Cocks, R.M. (2011). The Palaeozoic palaeogeography of central Gondwana. *Geological Society*, London, Special Publications, 357, 137-166. https://doi.org/10.1144/SP357.8.

Torsvik, T., & Cocks, L. (2017). Earth History and Palaeogeography. Cambridge: Cambridge University Press. doi:10.1017/9781316225523.

Torsvik, T.H., Van der Voo, R., Preeden, U., Niocaill, C.M., Steinberger, B., Doubrovin, P.V., van Hinsbergen, D.J.J., Domeier, M., Gaina, C., Tohver, E., Meert, J.G., McCausland, J.A., Cocks, R.L.M. (2012). Phanerozoic polar wander, palaeogeography and dynamics. *Earth-Science Reviews*. 114: 325–368. doi: 10.1016/j.earscirev.2012.06.007.

Van der Voo, R. (1990). The reliability of paleomagnetic data. *Tectonophysics*. 184, 1–9. https://doi.org/10.1016/0040-1951(90)90116-P

Vandamme, D. (1994). A new method to determine paleosecular variation. *Phys. Earth Planet. Inter.* 85, 131–142. https://doi.org/10.1016/0031-9201(94)90012-4

Wilson, T.J., Grunow, A.M., Hanson, R.E. (1997). Gondwana assembly: The view from Southern Africa and East Gondwana. *Journal of Geodynamics*. 23, 263-286. https://doi.org/10.1016/S0264-3707(96)00048-8.

Xian, H., Zhang, S., Li, H., Xiao, O., Chang, L., Yang, T., Wu, H. (2019). How Did South China Connect to and Separate from Gondwana? New Paleomagnetic Constraints From the Middle Devonian Red Beds in South China. *Geophysical Research Letters*. 46, 7371-7378. https://doi.org/10.1029/2019GL083123.

Chapter V

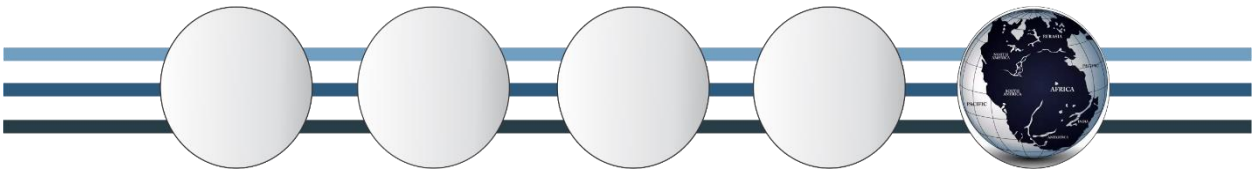

Throughout the development of my PhD project, which resulted in this thesis, I have explored a significant range of research topics about magma emplacement in large and hot orogens and the Cambrian drift of Gondwana. The main contributions of this thesis, as well as the immediate implications and perspectives, are summarized below, following each developed work.

1. Magma emplacement in large and hot collapsing orogens

1.1. Magma emplacement in the toes of a collapsing orogen

The first part of the thesis was dedicated to study the emplacement of magma in the toes of the large and hot Araçuaí orogen. In Temporim et al (2020), magnetic measurements, U-Pb geochronology and microstructures were used to determine the mechanisms of magma storage and deformation in the Santa Angélica pluton, emplaced in the southern portion of the Araçuaí orogen.

As implied by the numerical models of Jamieson and Beaumont (2013), in large and hot orogens no material is added to the orogenic system after convergence ends by tectonic advection, and the tectonic basal traction forces that support high topography are reduced or completely removed. In these final stages, orogens will decay by the effects of erosion and gravitational collapse, whereby extension and crustal thinning reduces lithospheric overburden through lateral flow of the hot orogenic interior.

The final stages of the Neoproterozoic-Cambrian Western Araçuaí-Congo orogen (~ 500 Ma) were marked by intense magmatic activity (I-type granite). U-Pb zircon ages were performed in Temporim et al. (2018) for the gabbroic core (498 ± 5 Ma), felsic border (506 ± 3 Ma) and a dioritic dike located 700 m away from the eastern border of the pluton (508 ± 3) which intrudes pre-collision Ediacaran plutonic rocks. All ages were interpreted as the age of magma crystallization. The dike was interpreted as an apophysis of the SA pluton. The magnetic fabric study indicates that AMS is dominantly carried by coarse-grained magnetite and shows a concentric structure for all lithotypes centered on the two gabbrodioritic nuclei. The different lobes can be distinguished on the basis of their magnetic lineations, with a marked difference in magnetic lineation inclination between the northeastern lobe where they are steeply-plunging to the southwestern lobe where dip with shallow angles. The form of these twin intrusions that form the Santa Angelica pluton was further detailed by a gravity study performed by Souza Junior et al (submitted). The authors complemented the previous AMS studies with structural analysis through anisotropy of magnetic susceptibility (AMS) and

microstructural data of oriented thin sections in the country rocks. 2D gravity modelling shows that the northeast lobe where lineations are almost vertical has a thickness of less than half of the southwest lobe and corresponds to the root of the pluton, similar to the configuration of the Cabeza de Araya pluton (Vigneresse and Bouchez, 1997). In contrast, the southwest lobe which is significantly thicker has shallowly-plunging lineations. Kinematic indicators suggest the mafic cores sink through a ductile and hot halo in midcrust conditions, and consequently deform the granites at the borders, as well as the country rocks, also generating the internal shear zone by the relative motion between the lobes. These results corroborate the interpretation of Temporim et al (2020) for the emplacement of the Santa Angélica pluton corresponding to that of two partly overlapping plutons, likely controlled by magma buoyancy forces, (almost) free of tectonic stress.

Bellon et al (2021) studied another post-collisional intrusion from the same region by performing anisotropy of magnetic susceptibility (AMS) measurements and microstructural analysis in the Venda Nova (VN) pluton. The VN pluton is an elliptical structure enveloped in its western side by a narrow ring of charnockitic rocks. The results reveal a concentric magnetic foliation/lineation pattern, similar to that observed for the Santa Angelica southwest lobe implying that buoyancy forces also controlled the magma emplacement of syenomonzonites and gabbros in the VN pluton, while a previous pulse of charnockitic was deformed by their intrusion. This study is another example of inversely zoned post-orogenic plutons located in the southern portion of the Araçuaí orogen which was emplaced through deep conduits at the colder forelands of the AO.

Santa Angélica, Venda Nova and other 'I-type' granitoid (e.g. De Campos et al., 2016) are located close to Araçuaí-Ribeira orogen connection, far from the warmer internal zone of the orogen at ~500 Ma. In this part of the orogen, deep structures (e.g. Guaçuí Shear zone) are an important channel to the ascent and emplacement of magma. They extend from the core of the orogen towards its toes, towards the Ribeira orogen, playing the role of a preferential channel for the lateral and vertical flow of mass. To better understand magma ascent and emplacement processes in this context it is important to simultaneously consider both the plutons and the crustal discontinuities that surround them.

1.2. Collapse mechanisms of orogens

The second part of the thesis was dedicated to assess the collapse mechanisms of the large and hot orogen itself. Temporim et al (submitted), performed a detailed mapping of magnetic

fabrics of coeval plutons at different sectors of the Araçuaí orogen (southern and northern portions), corresponding to different crustal levels of this ancient mountain belt. Besides, a compilation of geochronological and geochemical data from both sectors was also made.

The knowledge of the fabric pattern and the microstructural state of a pluton is essential for interpreting the pluton emplacement model in terms of magmatic versus tectonic processes (Cruden and Launeau, 1994; Bouchez, 1997; Sant'Ovaia et al., 2000). Granitic rocks are excellent recorders of deformation and suitable for interpretation of strain partition in different crustal levels in an orogenic system (Brown and Solar, 1999; Archanjo et al., 2002; Rey et al., 2009; Jamieson and Beaumont, 2011). Therefore, the study of the fabric pattern of plutons provides information on the tectonic scenario that prevailed at the moment of their emplacement. Variations of these modes can be envisioned depending on the partitioning of deformation in the crust, bearing in mind that deformation of the crust during gravitational collapse is complex being controlled by the evolution of its rheology, the mechanical behavior of the upper mantle, the coupling between crust and mantle and the evolution of boundary conditions (Rey et al., 2001, 2009).

At some stage of convergence in large and hot orogens, the erosion will outcompete the accretion, and a decrease in orogenic magnitude is expected, although temperatures in the orogenic core may persist high for tens of millions of years. In some cases, post-convergent exhumation of deepseated metamorphic rocks accompanies erosion at the orogenic flanks and extension and ductile thinning in the orogenic center (e.g., Rey et al., 2009; Jamieson and Beaumont, 2011; Vanderhaeghe, 2012). The end of tectonic convergence, and the consequent decrease of down-channel drag force, may also enhance the possibility of ultrahigh pressure (UHP) exhumation from the subduction conduit (e.g., Rey et al., 2009; Jamieson and Beaumont, 2011).

In the Araçuaí West Congo orogen, the collapse phase is marked by the contrasting rheological behavior of the crust at different depths. Such difference is well recorded by the internal structures of magmatic rocks from north to south of the belt. In the north, post-collisional magmatic rocks have ~NS-trending magnetic foliations following the collisional tectonic framework and marking a general along-strike magmatic flow from south to north. In turn, coeval deep-seated intrusions which crop out in the south, present a concentric distribution of foliations and lineations, in striking contrast with the general NE-SW trend of the host rocks. These contrasting magnetic fabric patterns coupled with the structural fabrics of host rocks and

geochemical signatures suggest magma flow from the orogen hot keel to a previously stretched flank, converted into post-collisional extensional zone during the gravitational collapse of the orogen edifice. These results show that during collapse mass flow took place in the deeper crust towards the southern flank of the orogen and was accompanied by deformation at the shallower crustal levels, as expressed by the plutons from the north (Peixoto et al., 2017), showing that the whole crust was involved in the orogen's collapse. This combination is achieved when the gravitational force overcomes the contractional strength of the surrounding lithosphere, thus triggering its bulk shortening.

Post-convergent exhumation of deep-seated metamorphic rocks accompanies the erosion at the orogenic flanks and the extension and ductile thinning in the orogenic core (Rey et al., 2009). Since in the Araçuaí fold belt these different lithotectonic domains were exhumed, we have a rare opportunity to actually see this rheological stratification from the root of the orogen, where large volumes of magma originated, up to the roof of the orogen, where large batholiths formed by the coalescence of magma batches emplaced close to the brittle-ductile transition. These magmas were likely entrained by the relatively steep shear zones that transect the metamorphic sequence and border the plutons in the southern sector, likely reaching the deep crust as predicted in numerical models (Jamieson et al and Beaumont., 2011). In this case, the emplacement of hot material over a cooler substrate is commonly interpreted as resulting in an "inverted" metamorphic sequence, with peak temperature at the partially molten mid-crustal section.

This work calls the attention to the need to consider markers with the same radiometric age at the orogen scale, providing snapshots of the deformation pattern and the thermobarometric conditions across the orogen. Since different lithotectonic domains from different paleodepths were exhumed in the Araçuaí belt, this approach additionally offers the opportunity to probe a crustal-scale profile, from the deeper crust in the south to the shallower brittle-ductile transition in the north. Other tools are needed to reveal the magma sources, and the involvement of the mantle in the late evolution of the Araçuaí orogen, including Nd and Hf isotopes on the magmatic supersuites and more refined barometric studies in the plutons from different sectors of the orogen.

2. Ediacaran-Cambrian Paleogeography of Gondwana

The last part of the thesis was dedicated to obtaining a high-quality paleomagnetic pole for the late Cambrian post-collisional plutons of the Araçuaí orogen. Together with the previously

existing data, this new result was used to better constrain the Furongian-Tremadocian drift of Gondwana. This topic had the partnership of a master's student who developed a paleomagnetic pole for the Venda Nova pluton. Also, a diffusion thermal model for the Santa Angélica and Venda Nova plutons that was considered in Temporim et al (2021) to replace the contact test and attest the primary nature of the magnetization in the bodies. The paleomagnetic work was developed at the CEED (University of Oslo), under the supervision of Dr. Mathew Domeier, where all data analysis and interpretation were performed, in addition to processing in the GPlates software.

In Temporim et al (2021) paleomagnetic analysis were conducted on the post-collisional Santa Angélica and Venda Nova plutons from the southern portion of the Araçuaí orogen. The results of this analysis isolated a characteristic magnetization likely carried by PSD/SD magnetite grains. This magnetic fraction is much less prominent than the coarse-grained MD magnetite which controls the AMS, but it is still enough to provide a stable magnetization. The population of magnetic directions from both plutons are coherent and associated with two groups which, for the Santa Angelica pluton, are demonstrated to be antipodal. An original methodological contribution of this work was the introduction of a thermal diffusion model to attest the primary nature of magnetization in the plutons. The age and the primary character of the characteristic remanent magnetization in plutonic bodies is known to be particularly difficult to assess (Torsvik et al., 1983; Watts and Briden, 1984; Gilder and McNulty, 1999). Given the distribution of positive and negative inclinations across the plutons, the thermal diffusivity model could be used to predict the zoning of magnetic directions during cooling. The pattern observed in both plutons is consistent with a primary thermoremanent magnetization, acquired during cooling of the intrusion in the midst of a field reversal. The combined SAVN pole computed from the pooled magnetic results (4.7° N, 332.2° E, N=35, A95=4.06 and K=68.82) completely satisfies all the stricter (updated) R-criteria of Meert et al. (2020). The SAVN pole closely corresponds to the late Cambrian Miaolingian-Furongian sector of the Gondwana APWP, and notably falls within the A95 of both the 500 and 510 Ma mean poles of that path. The new pole provides a critical new constraint from Congo-São Francisco block in the core of Western Gondwana in Terreneuvian-Tremadocian segment of the path, which is near-entirely dominated by results from Eastern Gondwana.

The global paleogeography is poorly known prior to Cambrian times. The latitudinal position of Gondwana in the Ediacaran and Cambrian periods is particularly problematic because there is little data available and results are mostly ambiguous (Abrajevitch and van der

Voo, 2010; McCausland et al., 2011). This uncertainty led to different paleogeographic and geodynamic models, with the continents distributed along the poles or close to the equator, depending on the arbitrary choice of the poles (e.g. McCausland et al., 2011). In addition, some sectors of the Gondwana APWP seem to show contrasting trends. The slightly older Cambrian poles (~520 Ma) from Western Gondwana appear to diverge from the trend of the East Gondwana APWP, implying that Western and Eastern Gondwana may have still been moving relative to one another immediately prior to the mid-Cambrian. For the Late Cambrian the database is near-entirely dominated by results from Eastern Gondwana. Therefore, obtention of new key poles for western Gondwana is essential to assent the coherence between Eastern and Western Gondwana through this time.

During the time interval between the Ediacaran and the Cambrian, drastic changes occurred on the planet, including a number of major changes in continental masses configuration and perhaps rotations involving the entire upper mantle (true polar wander events) (Meert and Liebermanb, 2008). Furthermore, the Neoproterozoic era is marked by periods of intense glaciation, with at least two events on a global scale (Hoffman et al., 1998). Also, in this period, the biosphere went through one of its most fundamental evolutionary processes (Popov, et al., 2014). What used to be a deep-water environment with microscopic life in dominantly anoxic conditions changed dramatically over the interval between 800 Ma and 500 Ma, generating profound environmental and biological changes, responsible for the emergence of complex life forms (Erwin et al., 2011; Xiao, 2014). In the Cambrian (and probably also in the Ediacaran), the prevailing paleonvironmental conditions were already those of the rest of the Phanerozoic. So, the paleoclimatic indicators recorded in sedimentary deposits laid down in the shallow shelf seas along the Gondwana margins can be used as an additional support to better constrain the paleogeography of that time (Álvaro et al., 2003).

Despite the scarcity of data, the latitudinal positions from Cambrian to Ordovician are well represented in the APWP for Gondwana, regardless of their divergences. However, in the ranges between Silurian and Devonian (more precisely 430-390 Ma) there is a massive scarcity of high quality paleomagnetic data. The few existing data are of low quality according to established criteria (Van der Voo, 1990; Meert et al., 2020) and come from sedimentary and metamorphic rocks, which are prone to secondary perturbations in their magnetic record. The search for new igneous rocks for this time interval is essential to improve the adjustment of the APWP of Gondwana.

Finally, most Brasiliano Neoproterozoic orogens have well-marked late to post-orogenic features. Both gabbroic bodies (Archanjo et al., 2009; Guimarães et al., 2012; McGee et al., 2012; Castro et al., 2013; Gorayeb et al., 2013; De Campos et al., 2016; Valeriano et al., 2016) and sedimentary basins (Almeida et al., 2010; Cordani et al., 2013) are excellent paleomagnetic targets for producing key poles for the West Gondwana and unravel divergences with East Gondwana or track if these two blocks were approximately coherent through this time.

References

Abrajevitch, A. and Van der Voo, R. (2010). Incompatible Ediacaran paleomagnetic directions suggest an equatorial geomagnetic dipole hypothesis. *Earth and Planetary Science Letters*, 293(1-2), pp.164-170.

Almeida, R.P., Janikian, L., Fragoso-Cesar, A.R.S., Fambrini, G.L. (2010). The Ediacaran to Cambrian Rift System of Southeastern South America: Tectonic Implications. *The Journal of Geology*, 118(2). https://doi.org/10.1086/649817.

Alvaro, J.J., Elicki, O., Rushton, A.W.A., Shergod, J.H. (2003). Paleogeographical controls on the Cambrian immigration and evolutionary patterns reported in the western Gondwana margin. *Paleogeography, Paleoclimatology, Paleoeoecology*, 195, 310-321.

Archanjo, C. J., Trindade, R. I., Bouchez, J. L., & Ernesto, M. (2002). Granite fabrics and regional-scale strain partitioning in the Seridó belt (Borborema Province, NE Brazil). *Tectonics*, 21(1), 1–14. https://doi.org/10.1029/2000TC001269

Archanjo, CJ, Launeau P, Hollanda M HBM, Macedo J WP, Liu D (2009). Scattering of magnetic fabrics in the Cambrian alkaline granite of Meruoca (Ceará state, northeastern Brazil). *International Journal of Earth Sciences*. 98 (8), p. 1793 – 1807. Doi: 10.1007/s00531-008-0342-z

Bouchez, J.L. (1997). Granite is never isotropic: an introduction to AMS studies of granitic rocks. In Bouchez, J.L., Hutton, D.H.W., Stephens, W.E. (Eds.), Granite: From Segregation of Melt to Emplacement Fabrics (Vol. 8., pp. 95–112). Kluwer Publishing Co., Dordrecht

Brown, M., Solar, G.S. (1999). The mechanism of ascent and emplacement of granite magma during transpression: a syntectonic granite paradigm. *Tectonophysics*, 312 (1), p. 1-33. https://doi.org/10.1016/S0040-1951(99)00169-9.

Castro, N.A., Ganade de Araujo, G.E., Basei, M.A.S., Osako, L.S., Nutman, A.A., Liu, D. (2012). Ordovician A-type granitoid magmatism on the Ceará Central Domain, Borborema Province, NE-Brazil. *Journal of South American Earth Sciences*, 36, p. 18-31. https://doi.org/10.1016/j.jsames.2011.11.007.

Cordani, G.U., Pimentel, M.M., Ganade De Araújo, C.E., Basei, M.A.S., Fuck, R.A., Girardi, V.A.V. (2013). Was there an Ediacaran Clymene Ocean in central South America?. *American Journal of Science*, 313 (6), p. 517-539. DOI: https://doi.org/10.2475/06.2013.01.

Cruden, A.R. and Launeau, P. (1994). Structure, magnetic fabric and emplacement of the Archean Lebel Stock, SW Abitibi Greenstone belt. *Journal of Structural Geology*, 16(5), 677-692. https://doi.org/10.1016/0191-8141(94)90118-X

De Campos C.M., Medeiros, S. R., Mendes J.C., Pedrosa-Soares, A. C., Dussin, I., Ludka, I. P., Dantas, E. L. (2016). Cambro-Ordovician magmatism in the Araçuaí Belt (SE Brazil): Snapshots from a post-collisional event. *Journal of South American Earth Sciences*, 68, 248-268. https://doi.org/10.1016/j.jsames.2015.11.016.

Erwin, D.H. et al. (2011). The Cambrian Conundrum: Early Divergence and Later Ecological Success in the Early History of Animals. *Science*, 334(6059), pp.1091–1097.

Gilder, S. and McNulty, B.A. (1999). Tectonic exhumation and tilting of the Mount Givens pluton, central Sierra Nevada, California. *Geology*, 27(10), pp.919-922.

Gorayeb, P.S.S., Chaves, C.L., Moura, C.A.V., Lobo, L.R.S. (2013). Neoproterozoic granites of the Lajeado intrusive suite, north-center Brazil: A late Ediacaran remelting of a Paleoproterozoic crust. *Journal of South American Earth Sciences*, 45, p. 278-292. https://doi.org/10.1016/j.jsames.2013.04.001.

Guimarães, S.B., Moura, M.A., Dantas, E.L. (2012). Petrology and geochronology of the Bom Jardim de Goiás copper deposit (GO). *Revista Brasileira de Geociências*. 42(4): 841-862. DOI: 10.25249/0375-7536.2012424841862

Hoffman, P.F. et al. (1998). A Neoproterozoic snowball earth. *Science*, 281(5381), pp.1342–1346. DOI: 10.1126/science.281.5381.1342

Jamieson, R.A., and Beaumont, C. (2011). Coeval thrusting and extension during post-convergent ductile flow— Implications for exhumation of high-grade metamorphic rocks. *Journal of Metamorphic Geology*, 29, 33–51. doi:10.1111/j.1525-1314.2010.00908.x

Jamieson, R. A., and Beaumont, C. (2013), On the origin of orogens. *GSA Bulletin*, v. 125, p. 1671-1702, https://doi.org/10.1130/B30855.1.

McCausland, P.J.A. et al. (2011). Ediacaran paleogeography of Laurentia: Paleomagnetism and Ar–Ar geochronology of the 583 Ma Baie des Moutons syenite, Quebec. *Precambrian Research*, 187(1-2), pp.58–78. Meert, J. G., & Voo, R. V. D.

McGee, B., Collins, A.S., Trindade, R.I.F. (2012). G'day Gondwana - the final accretion of a supercontinent: U–Pb ages from the post-orogenic São Vicente Granite, northern Paraguay Belt, Brazil. *Gondwana Research*. 21(2–3), p. 316-322. https://doi.org/10.1016/j.gr.2011.04.011

Meert, J.G. and Lieberman, B.C. (2008). The Neoproterozoic assembly of Gondwana and its relationship to the Ediacaran–Cambrian radiation. *Gondwana Research* 14, p. 5–21. doi:10.1016/j.gr.2007.06.007

Meert, J.G., Pivarunas, A.F., Evans, D.A.D., Pisarevsky, S.A., Pesonen, L.J., Li, Z.X., Elming, S.A., Miller, S.R., Zhang, S., Salminen, J.M. (2020). The magnificent seven: A proposal for modest revision of the Van der Voo (1990) quality index. *Tectonophysics*. 790, 228549. https://doi.org/10.1016/j.tecto.2020.228549.

Peixoto, E., Alkmim, F.F., Pedrosa-Soares, A., Lana, C., Chaves, A.O. (2017). Metamorphic record of collision and collapse in the Ediacaran-Cambrian Araçuaí orogen, SE-Brazil: Insights from P–T pseudosections and monazite dating. *J Metamorph Geol*., v. 36, p. 147–172. DOI: 10.1111/jmg.12287.

Popov, L.E. and Cocks, L.R.M. (2014). Late Ordovician brachiopods from the Chingiz Terrane, Kazakhstan, and their palaeogeography. *Journal of Systematic Palaeontology*. 12(6), p. 687-758. DOI 10.1080/14772019.2013.837844.

Rey, P., Vanderhaeghe, O., and Teyssier, C. (2001). Gravitational collapse of the continental crust: Defi nition, regimes and modes. *Tectonophysics*, v. 342, p. 435–449, doi:10.1016/S0040-1951(01)00174-3.

Rey, P.F., Teyssier, C., and Whitney, D.L. (2009). Extension rates, crustal melting, and core complex dynamics. *Geology*, v. 37, p. 391–394, doi:10.1130/G25460A.1.

Sant'Ovaia, H., Bouchez, J.L., Noronha, F., Leblanc, D., and Vigneresse, J.L. (2000). Composite-laccolith emplacement of the post-tectonic Vila Pouca de Aguiar granite pluton (northern Portugal): A combined AMS and gravity study: Transactions of the Royal Society of Edinburgh. Earth Sciences, Earth and Environmental Science Transactions of the Royal Society of Edinburgh, 91(1-2), 123-137, doi:10.1017/S026359330000732X

Temporim, F.A., Trindade, R.I.F., Tohver, E., Soares, C.C., Gouvêa, L.P., Egydio-Silva, M., Amaral, C.A.D., Souza Jr., G.F. (2020). Magnetic Fabric and Geochronology of a Cambrian "Isotropic" Pluton in the Neoproterozoic Araçuaí Orogen. *Tectonics*. 39(6), e2019TC005877. https://doi.org/10.1029/2019TC005877.

Temporim, F.A., Bellon, U.D., Domeier, M., Trindade, R.I.F., D'Agrella-Filho, M.S., Tohver, E. (2021). Constraining the Cambrian drift of Gondwana with new paleomagnetic data from post-collisional plutons of the Araçuaí orogen, SE Brazil. *Precambrian Research*, 359, p. 106212. https://doi.org/10.1016/j.precamres.2021.106212.

Torsvik, T.H., Løvlie, R. and Storetvedt, K.M. (1983). Multicomponent magnetization in the Helmsdale granite, North Scotland; geotectonic implication. *Tectonophysics*, 98(1-2), pp.111-129.

Valeriano, C.M., Mendes, J.C., Tupinambá, M., Bongiolo, E., Heilbron, M., Junho, M.C.B. (2016). Cambro-Ordovician post-collisional granites of the Ribeira Belt, SE-Brazil: a case of terminal magmatism of a hot orogen. *J. S. Am. Earth Sci*., 68, pp. 416-428.

Van der Voo, R. (1990). The reliability of paleomagnetic data. *Tectonophysics*. 184, 1–9. https://doi.org/10.1016/0040-1951(90)90116-P

Vanderhaeghe, O. (2012). The thermal-mechanical evolution of crustal orogenic belts at convergent plate boundaries: A reappraisal of the orogenic cycle. *Journal of Geodynamics*, v. 56–57, p. 124–145, doi:10.1016/j.jog.2011.10.004

Vigneresse, J.L., Bouchez, J.L. (1997). Successive Granitic Magma Batches During Pluton Emplacement: the Case of Cabeza de Araya (Spain). *Journal of Petrology*, 38 (12), p. 1767–1776, https://doi.org/10.1093/petroj/38.12.1767

Watts, D.R. and Briden, J.C. (1984). Palaeomagnetic signature of slow post-orogenic cooling of the north-east Highlands of Scotland recorded in the Newer Gabbros of Aberdeenshire. *Geophysical Journal International*, 77(3), pp.775-788.

Xiao, S. et al. (2014). The Weng'an biota and the Ediacaran radiation of multicellular eukaryotes. *National Science Review*, 1(4), pp.498–520.

Appendices

Appendix A

Supporting Information for chapter II

Magnetic fabric and geochronology of a Cambrian "isotropic" pluton in the Neoproterozoic Araçuaí hot orogen

Temporim, F. A., Trindade, R. I. F., Tohver, E., Soares, C. C., Gouvêa, L. P., Egydio-Silva, M., Amaral, C. A. D., Souza Jr., G. F.

Contents for Appendix A

Additional Supporting information

Data Set A1: AMS data of the Santa Angélica pluton in Mendeley repository.

Temporim, F.; Trindade, R.; Tohver, E.; Soares, C.; Gouvêa, L. P.; Egydio-Silva, M.s; Amaral, C.; Souza Jr., G. (2020), "AMS data of the Santa Angélica pluton", Mendeley Data, V2, doi: 10.17632/3xth2s5cp9.2

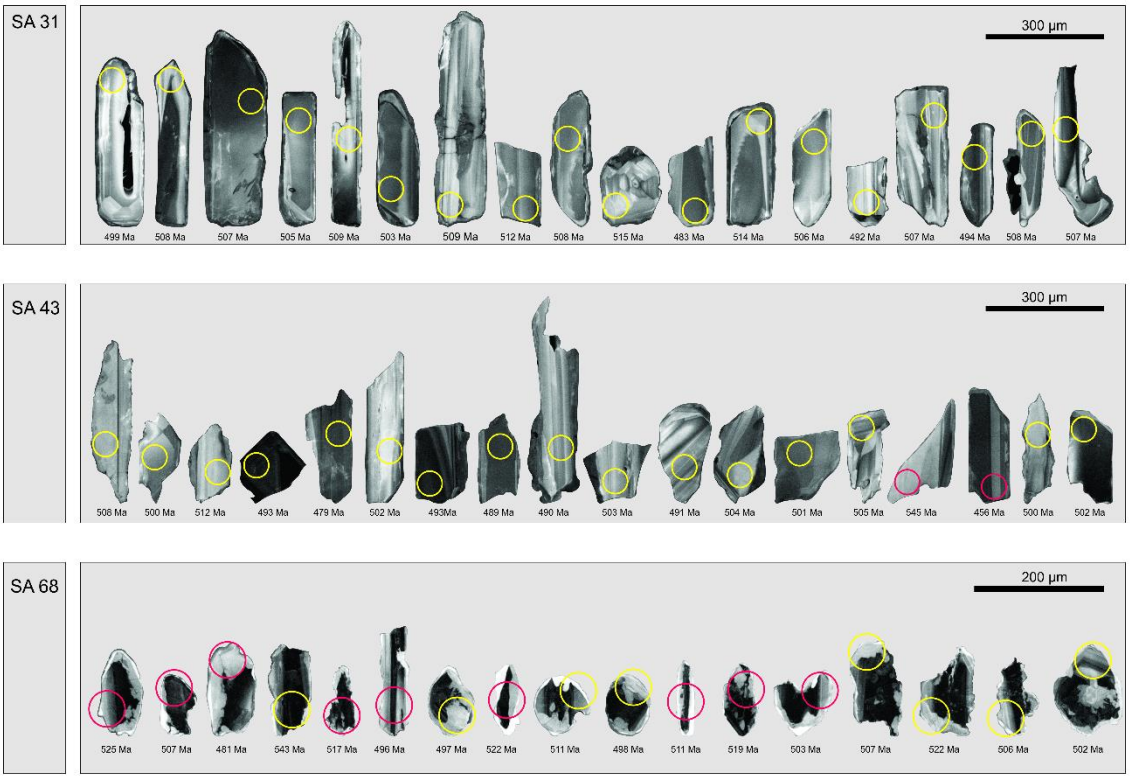

Figure A1: Cathodoluminescence images of representative zircons of the SA68 (dioritic dike), SA31 (foliated granite from edge of the pluton) and SA43 (gabbro from the core). Red circles represents results not used in concordia age calculations.

Spot	U (ppm)	Th (ppm)		$^{206}Pb^{*}$ (ppm)	$^{207}Pb^{*}/^{206}Pb^{*}$	±%	$^{207}Pb^{*}/^{235}U$	±%	$^{206}Pb^{*}/^{238}U$	±%	Err corr	$^{206}Pb/^{238}U$ Age		$^{207}Pb/^{206}Pb$ Age		% Discordant
SA31 - Foliated granite																
SA-31-11.1	159	284		11	0,0577	5,7	0,62	5,8	0,078	1,2	0,2	483	±6	518	±125	+7
SA-31-14.1	68	120		5	0,0573	20,0	0,63	20,1	0,079	2,0	0,1	492	±11	504	±441	+3
SA-31-1.1	60	127		4	0,0574	14,3	0,64	14,4	0,081	2,0	0,1	499	±10	508	±313	+2
SA-31-6.1	161	289		11	0,0573	5,1	0,64	5,2	0,081	0,9	0,2	503	±5	504	±113	+0
SA-31-4.1	88	161		6	0,0574	7,4	0,65	7,5	0,082	1,4	0,2	505	±7	508	±162	+1
SA-31-13.1	112	240		8	0,0577	19,5	0,65	19,6	0,082	1,7	0,1	506	±7	519	±429	+2
SA-31-3.1	256	334		18	0,0580	4,9	0,65	5,0	0,082	0,9	0,2	507	±4	529	±107	+4
SA-31-9.1	120	228		8	0,0571	11,2	0,65	11,3	0,082	1,3	0,1	508	±6	496	±247	-3
SA-31-5.1	56	88		4	0,0575	17,8	0,65	17,8	0,082	1,3	0,1	509	±7	510	±390	+0
SA-31-7.1	55	67		4	0,0572	16,8	0,65	16,8	0,082	1,3	0,1	509	±7	498	±369	-2
SA-31-2.1	125	66		9	0,0593	10,4	0,67	10,4	0,082	1,1	0,1	508	±5	579	±225	+13
SA-31-8.1	178	131		13	0,0582	6,3	0,66	6,4	0,083	0,9	0,1	512	±5	537	±138	+5
SA-31-12.1	73	101		5	0,0577	15,3	0,66	15,4	0,083	1,2	0,1	514	±7	518	±337	+1
SA-31-10.1	59	62		4	0,0583	15,1	0,67	15,2	0,083	1,2	0,1	515	±7	540	±331	+5
SA-31-16.1	223	494		15,2	0,0577	6,4	0,634	6,7	0,0797	2,2	0,3	494	±11	519	±140	+5
SA-31-18.1	180	496		12,6	0,0570	5,7	0,643	6,0	0,0818	2,0	0,3	507	±10	492	±126	-3
SA-31-17.1	133	278		9,4	0,0577	6,3	0,651	6,7	0,0819	2,1	0,3	508	±10	517	±139	+2
SA-31-15.1	72	133		5,0	0,0585	12,5	0,661	12,7	0,0820	2,2	0,2	507	±11	548	±274	+8
SA68 – Dioritic dike																
SA68-3.1	227	85		15	0,0573	6,9	0,61	7,0	0,078	1,2	0,2	481	±6	503	±152	+4
SA68-7.1	1115	440		77	0,0582	0,8	0,64	1,3	0,080	1,1	0,8	497	±5	539	±18	+8
SA68-9.1	296	53		20	0,0575	5,5	0,64	5,6	0,080	1,1	0,2	498	±5	511	±120	+3
SA68-12.1	449	752		31	0,0569	8,9	0,63	9,0	0,080	1,0	0,1	498	±5	487	±196	-2
SA68-22.1	798	1074		56	0,0584	4,7	0,65	4,8	0,081	0,9	0,2	503	±4	545	±103	+8
SA68-16.1	1322	2093		92	0,0570	2,4	0,64	2,5	0,081	0,8	0,3	503	±4	493	±53	-2

Spot	U (ppm)	Th (ppm)		$^{206}Pb^{*}$ (ppm)	$^{207}Pb^{*}/^{206}Pb^{*}$	±%	$^{207}Pb^{*}/^{235}U$	±%	$^{206}Pb^{*}/^{238}U$	±%	Err corr	$^{206}Pb/^{238}U$ Age		$^{207}Pb/^{206}Pb$ Age		% Discordant
SA68-19.1	701	1012		49	0,0573	2,3	0,65	2,5	0,082	0,9	0,4	506	±4	502	±51	-1
SA68-2.1	895	722		63	0,0578	2,7	0,65	2,8	0,082	0,9	0,3	507	±4	521	±59	+3
SA68-17.1	321	87		23	0,0587	4,5	0,66	4,6	0,082	0,9	0,2	508	±4	556	±98	+9
SA68-11.1	1123	745		80	0,0574	1,4	0,65	1,6	0,082	0,8	0,5	511	±4	506	±31	-1
SA68-13.1	712	1097		51	0,0631	7,4	0,72	7,5	0,083	0,9	0,1	514	±5	710	±158	+29
SA68-6.1	1396	702		100	0,0574	1,3	0,66	1,6	0,083	0,9	0,6	517	±5	505	±28	-2
SA68-15.1	1958	1632		141	0,0574	0,7	0,66	1,0	0,084	0,8	0,8	519	±4	506	±15	-3
SA68-18.1	943	1539		68	0,0575	2,3	0,67	2,4	0,084	0,8	0,3	521	±4	512	±51	-2
SA68-10.1	770	397		56	0,0576	2,3	0,67	2,4	0,084	0,8	0,3	522	±4	515	±50	-1
SA68-1.1	334	291		24	0,0574	5,1	0,67	5,2	0,085	0,9	0,2	525	±5	505	±113	-4
SA68-5.1	2730	2614		206	0,0574	0,7	0,69	1,1	0,088	0,9	0,8	542	±4	509	±15	-7
SA43 – Gabbro																
SA43-17.1	190	258		12,0	0,0553	4,7	0,558	5,3	0,0732	2,3	0,4	556	±10	423	±105	-8
SA43-5.1	205	371		13,6	0,0576	5,5	0,613	5,9	0,0772	2,0	0,3	479	±9	514	±121	+7
SA43-8.1	246	458		16,7	0,0579	3,9	0,630	4,4	0,0790	2,0	0,5	490	±9	526	±86	+7
SA43-9.1	104	157		7,1	0,0572	9,0	0,623	9,2	0,0790	2,2	0,2	490	±10	499	±197	+2
SA43-11.1	117	198		7,9	0,0575	5,2	0,627	5,6	0,0791	2,2	0,4	491	±10	511	±114	+4
SA43-7.1	393	531		26,8	0,0558	3,7	0,611	4,3	0,0794	2,1	0,5	493	±10	445	±83	-11
SA43-4.1	366	560		25,0	0,0568	2,2	0,623	2,9	0,0795	2,0	0,7	493	±9	485	±48	-2
SA43-18.1	118	123		8,2	0,0579	6,6	0,644	7,0	0,0807	2,3	0,3	500	±11	526	±146	+5
SA43-2.1	92	122		6,4	0,0584	6,4	0,650	6,8	0,0807	2,2	0,3	500	±11	546	±140	+9
SA43-13.1	181	227		12,6	0,0577	6,7	0,643	7,0	0,0808	2,0	0,3	501	±10	520	±147	+4
SA43-6.1	116	141		8,0	0,0579	5,2	0,647	5,6	0,0810	2,0	0,4	502	±10	527	±115	+5
SA43-19.1	243	465		16,9	0,0588	2,6	0,658	3,3	0,0812	2,1	0,6	503	±10	561	±56	+11
SA43-10.1	88	89		6,1	0,0577	5,5	0,646	5,9	0,0812	2,1	0,3	503	±10	520	±121	+3
SA43-12.1	89	89		6,2	0,0581	10,8	0,652	11,0	0,0815	2,1	0,2	505	±10	533	±236	+5

Spot	U (ppm)	Th (ppm)		$^{206}Pb^{*}$ (ppm)	$^{207}Pb^{*}/^{206}Pb^{*}$	±%	$^{207}Pb^{*}/^{235}U$	±%	$^{206}Pb^{*}/^{238}U$	±%	Err corr	$^{206}Pb/^{238}U$ Age		$^{207}Pb/^{206}Pb$ Age		% Discordant
SA43-14.1	181	293		12,7	0,0577	4,6	0,648	5,0	0,0816	2,0	0,4	505	±10	517	±100	+2
SA43-1.1	91	86		6,4	0,0576	3,8	0,650	4,3	0,0819	2,1	0,5	508	±10	514	±83	+1
SA43-3.1	113	98		8,0	0,0574	5,5	0,653	5,9	0,0826	2,0	0,3	512	±10	506	±121	-1
SA43-16.1	100	99		7,6	0,0587	5,9	0,714	6,2	0,0882	2,1	0,3	545	±11	558	±128	+2

Table A1: SHRIMP U–Pb data for zircons from the Cambrian Santa Angélica pluton. Errors are 2-sigma; Pb* indicate the common and radiogenic portions. Results in color were not used in concordia age calculations.

Appendix B

Supporting Information for chapter III

Magma ascent and storage across a collapsing large and hot orogen

Temporim, F.A., Trindade, R.I.F., Egydio-Silva, M., Angelo, T.V., Tohver, E., Soares, C.C., Gouvêa, L.P., Mendes, J.C., Medeiros, S.R., Pedrosa-Soares, A.C., Silva, G.G.,

Contents for Appendix B

Text B1: Analytical instrumentation and procedure

Oriented samples were extracted from 52 sites from the Vargem Grande and Caladão plutons at northern part of the Araçuaí orogen (AO) and Conceição de Muqui pluton at southern part of the AO. Between five and seven cores of approximately 8 cm in length and 2.5 cm in diameter were collected at each site using a portable gasoline powered drill. The cores were oriented in situ with both magnetic and solar compasses. Each core was cut into standard specimens that were 2.2 cm in length. All measurements were carried out in the Laboratório de Paleomagnetismo at the Universidade de São Paulo (USPmag).

The anisotropy of magnetic susceptibility (AMS) of individual samples was measured using an Agico Kappabridge MFK 1A. The AMS is second-rank symmetrical tensor, but it is commonly represented as an ellipsoid with three orthogonal axes (k1>k2>k3). P is defined as the degree of anisotropy, P=k1/k3 with P = 1 corresponding to a fully isotropic sample (0% anisotropy). T is defined as the shape factor, T=2ln(k2/k3)/ln (k1/k3)−1, reflecting the shape of the AMS ellipsoid and varying from −1 for prolate, purely linear magnetic fabric (i.e. k1>>k2=k3) through 0 (neutral) to +1 for oblate, purely planar magnetic fabric (i.e. k1=k2>>k3). Statistical evaluation of the magnetic anisotropy in individual sites was obtained using the methods of Jelínek (1978), implemented in the ANISOFT program package (Hrouda et al., 1990). Each station is characterized by the mean anisotropy parameters of a minimum of five specimens. The AMS directional data from individual sites were filtered to eliminate sites with high internal dispersion (ε12, ε 23), removing sites with uncertainty estimates >26.5° (Jelínek, 1978).

We investigated the contribution of specific minerals to the bulk rock magnetic susceptibility to better understand the results of the AMS measurements. Thermomagnetic experiments were acquired under argon flux to prevent excessive oxidation during heating using a CS-2 furnace attached to an Agico Kappabridge KLY 4 CS (Figure B1,B2). All thermomagnetic K-T curves (susceptibility K as function of temperature T) were performed at a temperature interval from -200 to 700°C. Hysteresis loops were obtained with a vibrating sample magnetometer (VSM) MicroMag 3900 (Princeton Measurements Corp) (Figure B3). Low values of coercivity can be seen in the hysteresis curves. This fact is also supported by the values of Mrs/Ms and Hcr/Hc in all samples, which are typical of multi-domain (MD) magnetite according to Day et al. (1977).

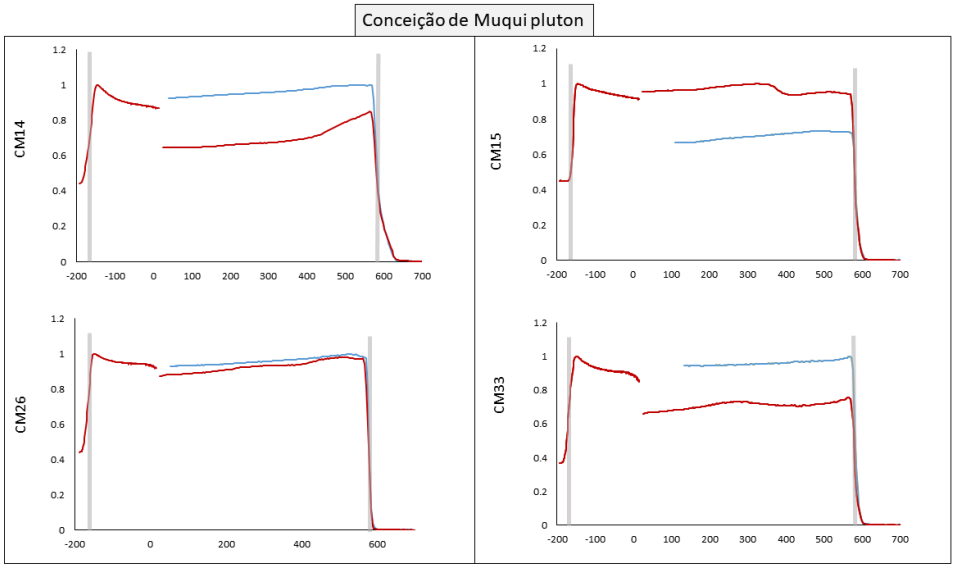

Fig. B1. Representative thermomagnetic curves for four samples of Conceição de Muqui pluton. The y-axis is the bulk of magnetic susceptibility and the x-axis is the temperature in degrees Celsius. The red lines represent the heating and blue lines represent the cooling.

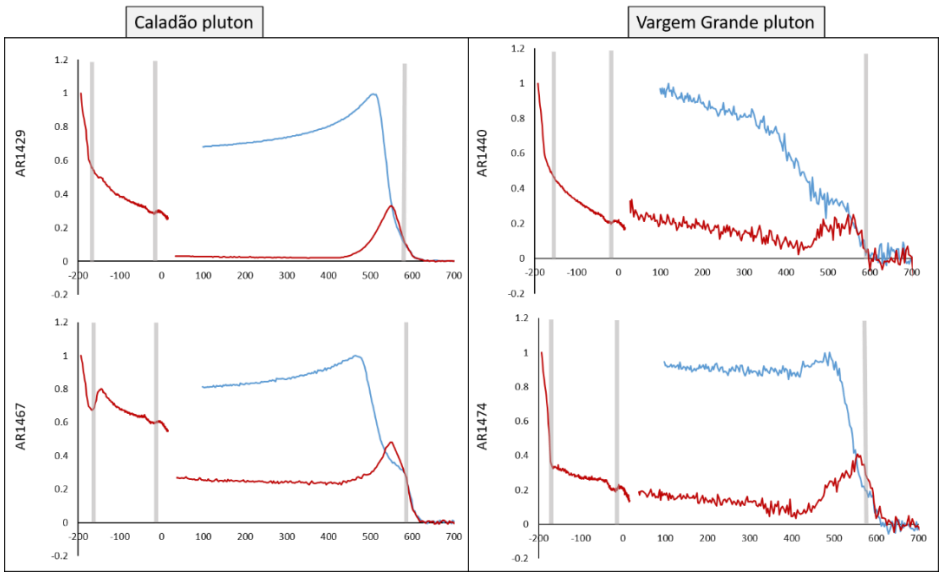

Fig. B2. Representative thermomagnetic curves for two samples of both Padre Paraíso charnockite and Caladão granite. The y-axis is the bulk of magnetic susceptibility and the x-axis is the temperature in degrees Celsius. The red lines represent the heating and blue lines represent the cooling.

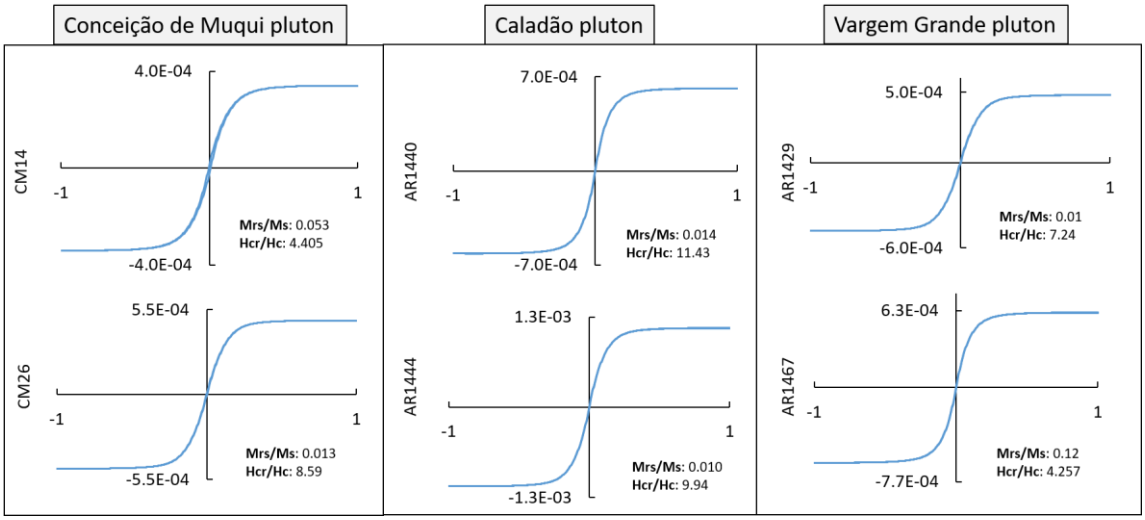

Fig. B3. Hysteresis loops for six samples which represents all the lithotypes present measured in this work. Mrs/Ms and Hcr/Hc rates (Day et al., 1977).

Supersuite	G1	G2	G3	G4	G5
U-Pb age (Ma)	630 – 580	585 – 540	545 – 500	530 – 490	525 – 480
Lithotypes	mostly tonalite to granodiorite, minor diorite to gabbronorite, with biotite, amphibole and/or pyroxenes	mostly biotite-garnet syenogranite to alkali feldspar granite, minor monzogranite to tonalite rich in garnet, and garnet-two-mica granite, locally with sillimanite	alkali feldspar granite to syenogranite with cordierite and/or garnet, poor to free of biotite	two-mica granite generally with garnet, pegmatoid granite	alkali feldspar granite to granodiorite, Opx-bearing charnockitic rocks, and gabbronorite; few mafic-only intrusions
Field relations	batholiths and stocks, generally rich in dioritic to mafic enclaves, generally showing solid-state deformation, metamorphism and migmatization, locally with well-preserved igneous fabrics, associated with the metavolcano-sedimentary Rio Doce Group	batholiths, stratoid bodies and stocks, showing solid-state deformation, metamorphism and migmatization, with common restites and xenoliths of metasedimentary rocks, and locally with well-preserved igneous fabrics	leucosomes in patches, veins, and lodes, minor stocks, free of regional deformation, mainly hosted by G2 metagranites	intrusive plutons, batholiths, stratoid bodies, free of regional deformation	intrusive balloon-shaped plutons, batholiths, irregular-shaped to roughly tabular bodies, free of regional solid-state deformation, rich in magma mingling-mixing features, with dioritic to mafic enclaves
Lithochemistry	metaluminous to slightly peraluminous (A/CNK < 1.1), magnesian, calcic to alkali-calcic, medium- to high-K, expanded calc-alkaline series	peraluminous, sub-alkaline to calc-alkaline	peraluminous, sub-alkaline to high-K alkaline	peraluminous sub-alkaline (K > Na) to alkaline (Na > K)	metaluminous to slightly peraluminous (A/CNK < 1.1), mostly ferroan, high-K calc-alkaline to alkaline; minor tholeiite
Isotopic signature	whole-rock: $\varepsilon Nd_{(t)}$: -3 to -13, Nd TDM: 1.2 to 1.8 Ga, $^{87}Sr/^{86}Sr_{(i)}$: 0.704 to 0.711; $\varepsilon Hf_{(t)}$ in zircon: +3 to -15, Hf TDM: 1.1 to 1.7 Ga	whole-rock $\varepsilon Nd_{(t)}$: -5 to -13 Nd TDM ages: 1.3 to 1.9 Ga whole-rock $^{87}Sr/^{86}Sr_{(i)}$: 0.707 to 0.713; $\varepsilon Hf_{(t)}$ in zircon: -2 to -8, Hf TDM: 1.3 to 1.9 Ga	$\varepsilon Hf_{(t)}$ in zircon: -4 to -10; Hf TDM: 1.3 to 1.7 Ga	$^{87}Sr/^{86}Sr_{(i)}$: 0.713	whole-rock $\varepsilon Nd_{(t)}$: -6 to -23; Nd TDM: 1.4 to 2.5 Ga; $^{87}Sr/^{86}Sr_{(t)}$: 0.702 to 0.716; $\varepsilon Hf_{(t)}$ in zircon: +13 to -44; Hf TDM: 0.6 to 3.7 Ga
Genetic type	mostly metaluminous I-type, minor peraluminous I-type	mostly S-type, minor peraluminous I-type	S-type	S-type	A-type and I-type
Tectonic stage and setting	pre-collisional to early collisional, continental margin magmatic arc (Rio Doce arc)	late pre-collisional to late collisional	late collisional to post-collisional	late collisional to post-collisional	post-collisional

Table B1. Main characteristics of the G1 to G5 supersuites of the Araçuaí orogen (after Pedrosa-Soares et al., 2011, 2020, Serrano et al., 2018, and Wisniowscky et al., 2021, updated with data from Gouvêa et al., 2020; Soares et al., 2020; Temporim et al., 2020; and the present paper).

Site (n)	Location - UTM		Scalar data			Direction of principal axes					
	X (w)	Y (s)	*Km (10^{-3}SI)*	*P*	*T*	k_1	ε_{12} (k_1)	k_2	ε_{23} (k_2)	k_3	ε_{31} (k_3)
Caladão Pluton											
[1]AR963	-	-	3.65	1.041	0.043	076/46	021/20	265/44	072/21	171/05	072/19
[1]AR962	-	-	2.29	1.047	0.103	009/13	068/11	277/11	068/32	148/73	032/11
[1]AR638	-	-	8.04	1.122	0.017	212/51	067/43	329/20	067/26	072/32	046/33
AR1441	258328	8021964	1.13	1.055	-0.034	84/49	18.5/11.5	215/28	43.9/15.9	320/25	44.3/11
AR1445	261298	8028849	0.395	1.032	-0.255	275/33	20.1/8.2	182/4	38.6/13.6	85.6/55	37.2/5
AR1449	266623	8040517	3.47	1.026	0.376	139/15	24.3/3.9	47/7	27.4/9.9	292/72	20.4/4
AR1453	269964	8046486	3.34	1.052	-0.482	58/33	20.1/9	226/56	47/17.6	325/6	46.7/6
AR1475	269625	8047012	2.086	1.043	0.734	180/5	47.6/8.3	87/26	47.6/18.6	281/62	19.4/6
AR1478	238809	8113506	1.59	1.069	-0.054	170/33	24.5/9.3	315/50	29.8/13.8	68/17	26/11.5
TM21	263148	7999926	1.53	1.056	0.72	255.8/1.1	29.3/8.7	165.4/22.2	28.8/7.8	348.5/67.8	10.9/7.3
TM22	265612	7998241	308	1.125	-0.291	292.5/19	20.2/7.4	174.6/53.2	22.2/14.5	34.2/30.0	18.6/8.3
TM31	269335	8014136	3.06	1.062	0.677	273.0/38	27.0/9.0	177.1/7.3	28.2/10.8	78.2/50.5	15.2/8.6
TM36	265512	8006815	4.44	1.039	0.149	245.3/14	28.1/18.2	344.2/31.7	27.9/27.5	134.7/54.7	29.2/16.1
TM40	265849	8006119	10.4	1.075	0.744	259.7/37	29.4/6.8	1.0/14.5	29.3/7.1	108.4/49.1	8.1/6.7
TM42	266091	8003275	3.18	1.095	0.104	273.1/52	30.0/15.1	115.6/35.4	30.0/11.1	17.7/11.0	15.6/11.6
AR1428	270135	8021238	6.196	1.04	-0.302	25/60	15.2/8	48/22	38.8/9.1	150/18	39.2/12
AR1429	270145	8021243	6.78	1.032	0.049	268/61	16.9/7.1	176/13	18.6/15.4	145/16	19.2/9
AR1430	270136	8021238	3.55	1.024	-0.491	276/35	24.4/24.2	174/51	50.9/13.5	69/51	49.3/26
AR1438	274032	8035791	3.07	1.038	-0.505	11.0/37	20.6/15.2	319/16	58.7/19.6	275/8	58.8/13
AR1439	273693	8038538	5.08	1.056	0.212	52/11	24.3/12.2	183/2	24.4/13.1	176/69	14.4/11
AR1451	268514	8044149	3.73	1.044	0.176	92/3	18.6/12	293/6	24/7.5	313/85	23.7/16
AR1456	276042	8056137	2.322	1.07	-0.25	24/10	8/6.1	337/7	43.2/7.8	172/77	43.2/6
AR1465	276681	8051149	5.35	1.037	0.425	246/9	34.2/9.7	346/44	34.5/15.5	103/77	18.2/7

AR1467	275481	8052149	6.401	1.076	0.383	224/28	14.2/12	11.0/24	20.1/8.8	114/32	17/11
AR1469	272273	8032846	3.893	1.045	0.097	258/41	21.2/14.7	207/37	30.1/19.8	122/38	29.8/15
AR1471	271528	8039285	2.497	1.037	-0.863	75/41	21.4/14.9	198/26	79/19	319/26	79/17.7
AR1472	274567	8041567	1.254	1.041	0.126	103/10	25.5/6.2	55.0/8	32.9/16.1	354/61	23.4/6
AR1473	276439	8056355	15	1.093	-0.049	253/16	19.5/18	21/56	34/17.4	154/29	34.8/15
AR1474	275170	8049123	5.017	1.155	-0.243	242/25	19.2/6.6	273/45	37.8/12.3	143/19	40.5/13
AR1476	236692	8111481	1.911	1.055	0.106	165/16	40.8/13.5	192/11	41.1/11.6	61/39	17.8/11
AR1477	237304	8112047	4.968	1.049	0.284	89/47	23.3/19.1	313/9	32.7/19.1	292/40	32.4/22
TM32	268359	8010619	7.96	1.033	0.187	213.0/47	29.2/15.0	313.1/9.2	29.3/20.5	51.3/41.2	23.5/9.2
TM37	264545	8006999	5.09	1.022	0.11	229.6/21	28.5/10.7	332.7/30.2	28.7/19.0	110.0/51.7	19.4/10.5
TM38	264294	8005048	22.1	1.057	0.019	246.8/34	20.3/17.3	339.8/4.3	30.0/19.3	76.0/54.9	30.4/17.6
TM39	262960	8004596	7.13	1.064	0.376	171.6/20	24.0/15.4	266.7/13.6	30.0/21.4	28.8/65.5	29.9/16.5
TM43	262350	8001471	73.5	1.11	0.527	235.9/13	18.3/7.5	326.9/4.1	17.8/4.8	73.4/75.9	9.0/4.5
Vargem Grande Pluton											
MSB10	273936	7956770	0.0769	1.039	0.030	015/21	14/11	281/10	16/14	167/66	16/10
MSB11	265654	7943125	0.665	1.054	-0.108	002/18	17/13	110/48	79/11	257/37	79/14
MSB13	266700	7939451	1.56	1.153	-0.173	246/34	17/10	359/31	47/16	120/41	47/9
MSB14	267014	7941065	2.04	1.113	-0.011	218/18	36/17	121/22	36/24	344/61	25/18
MSB16	270928	7943359	0.442	1.034	0.125	330/11	38/29	067/33	55/39	224/55	56/31
MSB18	271507	7945548	1.49	1.127	0.333	222/06	30/18	129/29	30/18	323/60	19/16
MSB20	273371	7946946	5.37	1.199	0.408	238/12	33/18	135/47	36/14	338/41	19/12
MSB21	276726	7946655	9.08	1.098	0.431	248/39	30/22	137/24	30/26	024/41	30/21
MSB28	279059	7948188	0.269	1.029	0.302	304/25	77/28	042/17	77/26	162/60	34/24
MSB29	272933	7949324	0.122	1.029	0.274	113/03	22/14	203/02	21/14	334/86	22/10
MSB30	270225	7948979	0.187	1.036	0.489	081/14	37/8	177/23	37/9	322/62	11.0/06
MSB32	271233	7930822	0.14	1.071	0.197	351/51	15/14	096/11	41/11	194/37	41/15
MSB34	269663	7933828	0.502	1.053	-0.365	045/37	16/08	142/09	16/12	243/51	12.0/8
MSB35	269305	7933195	0.507	1.039	0.004	055/33	37/10	312/19	37/26	198/51	28/12

MSB36	268818	7933647	0.359	1.057	-0.311	044/16	009/05	313/06	21/05	202/73	21/08
MSB37	267118	7933039	0.409	1.029	0.015	032/32	25/11	284/26	36/21	163/47	36/13
MSB38	263594	7932852	0.794	1.12	0.020	307/70	11.0/7	150/19	27/09	057/07	27/10
MSB44	276488	7935165	0.751	1.055	0.218	071/24	36/20	332/19	44/36	209/59	45/17
MSB45	273336	7932609	0.644	1.078	-0.330	005/46	12.0/07	222/37	20/08	116/20	20/11
MSB46	273394	7932314	0.177	1.032	0.117	357/37	67/30	250/22	67/28	136/45	41/25
MSB48	274429	7935173	3.71	1.048	-0.049	002/55	49/32	129/23	59/48	231/25	59/32
MSB04	285647	7954071	6.11	1.065	0.548	286/39	59/39	112/40	59/20	170/28	23/15
MSB05	283194	7952881	2.19	1.075	0.362	270/47	54/14	307/32	54/24	012/11	25/15
MSB06	281029	7952177	5.6	1.049	0.574	042/08	53/14	089/12	53/13	145/56	19/14
MSB07	281062	7952462	3.37	1.047	0.685	345/48	69/18	001/10	69/26	188/40	29/20
MSB08	277190	7955237	6.95	1.057	0.015	093/10	21/15	147/17	35/17	226/75	34/16
MSB09	275199	7956513	3.51	1.034	-0.219	048/27	40/32	049/10	49/40	266/57	50/27
MSB22	277454	7938418	1.63	1.033	0.413	315/23	30/14	177/13	35/31	161/65	35/13
MSB23	276065	7938227	8.81	1.042	0.88	082/21	79/22	304/02	79/11	296/65	27/11
MSB33	270578	7933830	7.01	1.062	-0.076	036/42	13/10	168/05	20/10	211/48	20/11
MSB02	285540	7953583	0.0209	1.032	0.001	299/57	14/06	182/17	26/08	083/27	24/07
MSB26	274932	7943068	4.31	1.045	0.584	189/37	80/43	033/51	80/54	288/12	60/50
MSB40	277996	7930636	0.185	1.031	0.057	189/09	24/15	289/48	44/19	092/41	44/18
MSB41	278760	7930745	0.0692	1.053	0.455	236/12	36/9	335/37	37/18	131/51	23/09
MSB42	280079	7932446	0.0781	1.022	-0.245	346/31	61/33	081/07	73/54	182/58	72/29
MSB43	280174	7933250	0.0573	1.057	-0.239	293/51	31/19	044/16	57/28	145/34	57/17
MSB49	277304	7930794	0.139	1.032	-0.605	272/53	22/19	119/34	59/18	020/13	59/21
MSB50	276176	7930953	0.239	1.075	0.67	060/04	55/10	326/44	55/17	154/46	18/10
MSB51	275539	7930278	0.387	1.077	0.741	238/05	25/12	333/45	25/09	143/44	13/08
MSB52	274526	7929441	0.17	1.082	0.731	035/09	61/17	296/46	61/16	133/43	23/11
Barra de São Francisco Pluton											
AR396	306242	7928462	1.55	1.09	0.098	74/21	41/23	168/05	37/26	264/49	32/27

AR394	302926	7924490	5.71	1.16	-0.335	171/04	33/13	081/09	33/19	286/80	21/11
AR399	294762	7923024	0.251	1.06	0.618	109/02	40/13	016/53	40/9	201/36	16/5
AR401	292599	7923912	0.014	1.12	0.198	175/61	26/12	329/27	62/22	064/11	62/11
AR403	287947	7923279	0.046	1.08	0.308	076/35	65/22	324/28	67/18	205/42	45/22
AR404	286790	7923155	0.021	1.17	0.632	055/25	4.0/3	321/10	5.0/3	211/63	4.0/3
AR408	282949	7923990	0.056	1.07	0.207	048/16	12.0/5	139/04	12.0/9	242/74	13/6
AR426	298929	7932258	0.177	1.68	0.53	072/18	44/7	168/20	44/43	303/63	43/8
AR428	298321	7934388	0.069	1.05	0.098	094/20	22/14	205/45	35/18	347/39	35/19
AR437	304084	7931473	0.167	1.11	0.626	257/12	10.0/5	348/04	49/8	095/78	49/4
AR439	305396	7933295	0.095	1.07	0.395	093/12	24/7	003/03	57/18	259/77	56/7
AR456	315606	7935724	0.098	1.07	0.567	102/05	13/6	195/34	50/3	005/56	50/6
AR457	316500	7935609	0.238	1.07	0.418	187/31	42/19	082/23	43/22	323/49	28/20
AR458	315650	7932401	0.082	1.07	0.407	142/19	19/11	254/47	27/10	037/37	31/8
AR526	313434	7936143	0.104	1.14	0.434	161/01	35/9	071/14	56/34	255/76	56/11
AR527	312791	7934451	0.109	1.08	0.235	252/15	26/12	342/01	70/11	075/74	70/25
AR528	316437	7934833	0.127	1.12	0.52	140/20	53/18	200/19	54/21	300/60	22/18
AR529	319114	7934804	0.079	1.13	0.327	260/02	45/28	354/59	45/35	169/31	49/35
AR530	320069	7938719	0.081	1.14	0.613	114/48	76/23	244/29	76/24	350/26	27/20
AR532	321438	7938195	0.124	1.08	0.147	149/11	13/08	279/73	37/7	056/13	37/13
AR533	322158	9403060	0.157	1.09	0.036	168/28	36/21	288/44	49/31	058/33	50/15
AR534	316256	7934809	0.085	1.08	0.347	197/17	42/17	103/13	45/22	339/69	31/14
AR536	317477	7924848	0.084	1.09	0.396	209/14	60/14	308/32	60/30	099/54	31/16
AR537	315352	7917123	0.133	1.14	0.211	74/12	5.0/2	331/47	22/3	175/40	22/2
AR538	307704	7940988	0.112	1.09	0.483	162/01	28/10	253/17	35/13	068/73	28/8
AR539	309552	7941027	0.168	1.05	0.336	119/03	30/16	210/25	30/22	023/64	23/17
AR540	310730	7942729	0.09	1.07	0.315	316/02	21/10	224/38	20/11	048/52	13/10
AR541	306089	7963656	0.107	1.08	0.155	318/16	71/25	224/14	71/13	094/69	41/15
AR542	306847	7958966	0.107	1.06	0.16	139/03	27/17	229/01	27/19	326/87	21/14

AR544	317051	7941359	0.115	1.04	0.17	239/18	43/21	115/61	67/29	337/23	67/30
AR543	303348	7933063	0.061	1.11	0.554	147/22	12.0/8	057/01	24/11	324/68	24/8
AR545	319412	7940559	0.082	1.1	0.193	118/04	57/29	208/03	72/42	336/85	71/30
AR547	323818	7943051	0.229	1.04	0.01	160/07	12.0/4	251/10	18/10	035/77	16/3
AR548	328379	7941325	0.155	1.07	-0.01	010/38	16/2	107/10	15/9	210/51	9.0/6
AR549	306146	7970047	0.118	1.06	0.09	296/07	66/21	029/19	66/22	186/70	25/17
AR550	306740	7972848	0.137	1.08	-0.059	127/06	10.0/7	218/06	44/7	349/82	44/8
AR551	304782	7974240	0.15	1.1	0.584	358/24	26/11	149/63	26/8	263/12	12.0/7
AR552	303683	7973838	0.107	1.08	0.275	320/07	36/16	052/16	37/16	207/72	22/14
AR553	302879	7976507	0.091	1.14	0.03	119/02	20/10	028/07	76/8	222/82	76/10
AR606	282425	7923991	0.087	1.07	0.08	213/02	31/5	303/06	48/10	107/84	47/5
AR607	273754	7927322	0.319	1.1	0.56	005/41	16/9	263/14	16/6	159/46	12.0/4
AR612	280096	7932408	0.097	1.05	0.48	269/28	26/5	015/28	27/8	142/50	10.0/3
AR626	275029	7925797	0.215	1.07	0.361	301/40	13/5	208/03	14/6	115/50	13/12
AR629	279180	7933327	0.044	1.11	0.746	252/16	28/15	345/11	28/26	109/70	31/6
AR630	278834	7934399	0.987	1.05	0.477	241/20	49/15	343/31	48/21	123/53	32/12
AR655	297902	7935712	0.099	1.09	0.401	154/34	42/14	046/26	57/22	287/45	55/19
AR658	292540	7938104	0.116	1.03	0.27	301/01	23/13	211/01	23/12	059/89	15/10
AR660	290417	7931372	0.127	1.12	0.531	091/33	39/13	294/55	46/38	188/11	47/9
AR661	291728	7908436	0.083	1.19	0.404	160/51	29/16	315/36	42/28	054/13	42/16
AR662	291533	7924815	0.12	1.03	0.105	218/54	21/09	036/36	22/13	127/01	23/18
AR664	288742	7942919	0.109	1.05	0.295	278/27	19/14	020/22	19/6	144/54	14/7
AR665	309583	7941961	0.208	1.08	0.201	252/18	45/13	147/40	56/23	001/45	51/14
AR668	308771	7960128	0.146	1.07	0.139	298/03	20/8	207/13	20/9	041/77	11.0/10
AR669	306246	7954229	0.2	1.1	0.336	117/05	33/16	025/20	37/26	219/70	32/16
AR699	307501	7946813	0.245	1.05	-0.093	203/24	64/18	309/32	62/21	083/48	41/18
AR1110	315562	7938938	0.085	1.05	0.252	135/05	62/18	225/00	62/10	316/85	20/7
AR1113	334707	7944455	0.121	1.08	0.256	235/57	25/15	014/26	35/22	114/19	34/13

AR1115	333317	7941693	0.12	1.05	0.053	008/18	18/14	099/04	44/14	201/71	44/17
AR1116	336262	7942870	0.272	1.07	0.225	197/07	18/04	292/34	29/6	096/55	31/8
AR1117	336503	7938051	0.197	1.06	0.131	330/04	78/33	061/14	78/47	224/75	60/39
AR1118	336050	7936714	0.118	1.04	0.382	222/06	22/12	317/40	22/21	125/50	22/10
AR1119	306872	7914395	0.065	1.07	-0.195	210/13	11.0/8	064/75	22/10	302/08	21/8
AR1120	308484	7906277	0.087	1.05	0.078	079/18	44/29	199/56	74/36	340/27	74/39
AR1122	311905	7906849	0.111	1.07	0.565	299/12	14/04	035/25	14/7	187/62	8.0/4
AR1123	309266	7971203	0.116	1.08	0.044	140/13	20/11	231/01	22/16	327/77	18/10
AR1129	310603	7972260	0.111	1.05	-0.047	138/16	12.0/7	036/36	16/9	248/50	15/7
AR1130	312164	7973902	0.062	1.07	0.203	137/20	25/18	043/11	20/17	285/67	25/17
AR1131	315881	7977029	0.107	1.07	-0.157	165/04	36/18	256/13	43/32	056/76	42/19
AR1133	317735	7984112	0.095	1.07	-0.006	341/01	14/6	071/19	34/10	248/71	34/12
AR1134	318761	7983812	0.081	1.07	0.1	329/06	13/10	239/01	27/7	135/84	26/11
AR1135	318017	7976713	0.062	1.13	-0.005	131/01	21/06	040/09	26/12	227/80	26/18
AR1136	305098	7980578	0.12	1.1	-0.117	338/05	18/14	244/40	35/15	074/50	35/15
AR1137	304386	7982248	0.071	1.06	-0.167	341/55	16/8	156/35	24/13	248/02	23/7
AR1138	303243	983094	0.147	1.11	-0.137	112/16	19/7	359/53	71/10	212/32	71/12
AR1139	303563	7984451	0.111	1.11	0.237	281/32	22/7	012/02	61/9	105/58	61/11
AR1140	313978	7977327	0.105	1.07	-0.254	303/01	22/18	209/71	67/19	033/19	67/16
AR1142	308572	7975054	0.095	1.05	-0.151	124/02	13/8	034/02	14/12	258/87	14/8
AR1143	310488	7979388	0.374	1.15	-0.225	116/16	18/9	323/73	53/17	209/07	53/8
AR1144	309050	7967261	0.106	1.04	-0.06	082/66	18/9	332/09	22/17	238/23	22/10
AR1145	311684	7969262	0.14	1.07	0.053	310/04	13/12	220/09	17/12	065/80	19/10
AR1254	290899	7959234	0.07	1.06	0.444	145/19	43/16	243/21	43/9	018/61	17/13
AR1255	288512	7954383	0.071	1.05	0.251	273/14	29/6	179/16	29/7	043/69	9.0/5
AR1257	311225	7957193	0.115	1.07	0.171	306/05	24/9	037/08	25/18	188/80	20/7
AR1258	312444	7958891	0.12	1.08	0.149	288/05	16/11	020/21	20/12	185/68	18/9
AR1259	316325	7959177	0.153	1.12	0.321	134/00	27/14	224/17	41/14	044/74	37/14

AR1260	321074	7958438	0.159	1.06	-0.023	316/03	14/7	225/17	19/14	057/73	19/7
AR1261	305074	7965928	0.113	1.06	0.089	113/06	35/7	022/09	35/7	235/79	8.0/7
AR1263	321030	7964843	0.172	1.08	-0.004	306/01	17/9	216/06	18/12	047/83	16/6
AR1265	335937	7967567	0.181	1.04	-0.243	284/35	40/21	048/38	50/38	167/33	51/24
AR1266	296637	7940201	0.135	1.05	0.484	076/41	14/9	175/11	16/14	277/48	16/8
AR1267	297694	7941186	0.106	1.06	0.417	064/03	47/9	154/04	47/14	298/85	15/10
AR1268	298716	7939788	0.127	1.05	0.55	253/14	27/7	163/01	27/14	068/76	16/8
AR1269	293740	7950714	0.097	1.05	0.38	099/03	53/28	008/25	54/36	194/65	38/28
AR1270	294388	7957824	0.145	1.06	0.249	230/09	79/26	137/17	79/37	348/71	52/25
AR1271	295338	7963036	0.169	1.05	0.342	082/14	14/30	172/01	29/12	262/76	18/6
AR1272	297387	7961829	0.134	1.06	0.274	098/11	32/10	006/10	32/12	234/75	12.0/11
AR1273	303096	7969239	0.171	1.12	0.337	340/60	12.0/10	224/15	12.0/11	126/26	15/5
AR1274	300387	7971506	0.168	1.09	0.374	305/06	30/7	038/32	32/10	206/58	18/7
AR1276	298091	7973031	0.149	1.7	0.473	307/01	40/7	037/10	40/13	210/80	13/8
AR1277	295158	7975351	0.142	1.08	0.233	278/01	19/14	009/24	20/12	185/66	14/13
AR1278	295108	7977721	0.08	1.08	0	096/04	38/8	005/10	38/11	209/79	13/8
AR1279	292797	7980301	0.102	1.13	0.45	229/06	28/13	326/52	34/23	135/38	33/7
AR1280	330878	7950433	0.114	1.07	0.344	263/73	32/18	108/16	67/23	016/07	67/17
AR1283	339464	7954938	0.088	1.39	0.513	068/68	40/23	193/13	61/33	287/17	61/11
AR1283	341490	7957499	0.359	1.04	0.255	336/57	17/8	082/10	16/13	178/31	13/9
AR1284	339082	7953571	0.1	1.05	0.556	101/21	51/16	335/56	50/8	201/25	17/9
AR1286	317712	7962155	0.174	1.08	0.126	295/28	18/12	202/05	18/7	103/62	18/7
AR1287	314224	7966588	0.102	1.06	-0.066	119/16	10.0/7	026/12	19/10	259/70	19/7
AR1288	322570	7920046	0.168	1.05	0.644	023/29	17/7	288/10	19/16	181/59	19/9
AR1290	325616	7922598	0.086	1.06	0.566	273/03	75/11	005/32	75/18	179/58	18/11
AR1291	322965	7924106	0.105	1.05	0.546	281/04	71/9	012/07	71/12	163/82	13/10
AR1294	312808	7985116	0.166	1.14	-0.156	327/40	16/13	204/56	61/12	067/26	61/12
AR1313	289349	7971441	0.535	1.12	0.357	114/22	20/6	017/17	21/17	253/62	18/6

AR1315	288429	7966723	0.068	1.06	0.546	288/15	24/9	026/26	24/11	172/59	11.0/10
AR1321	327674	7920325	0.141	1.09	0.31	008/37	19/13	270/11	19/10	167/51	14/9
AR1329	311856	7916955	0.066	1.09	0.655	291/43	14/4	048/27	15/12	159/36	13/5
AR1330	313282	7918038	0.058	1.05	0.45	328/24	73/9	063/12	73/7	177/63	16/7
AR1331	315297	7917231	0.152	1.08	0.774	310/18	55/4	043/10	55/4	160/70	6.0/3
AR1332	316651	7914124	0.219	1.05	0.506	272/01	28/10	003/34	28/11	180/56	14/8
AR1333	318833	7915657	0.137	1.06	0.583	005/19	51/12	266/13	51/11	145/67	12.0/11
AR1334	322477	7919803	0.205	1.07	0.695	311/16	28/6	050/27	28/6	194/58	8.0/6
AR1335	322986	7921870	0.162	1.08	0.645	026/26	31/9	282/26	31/14	154/51	15/10
AR1336	330117	7919091	0.174	1.09	0.364	345/37	13/8	086/13	10.0/9	192/50	13/9
AR1338	331821	7921356	0.228	1.07	-0.187	348/45	14/9	083/05	25/4	178/45	24/14
AR1339	333490	7924135	0.281	1.05	-0.012	035/50	21/10	257/32	21/15	153/21	17/9
AR1341	331424	7926159	0.243	1.08	0.489	038/29	24/4	129/02	25/6	222/61	10.0/5
AR1342	332316	7928750	0.196	1.03	-0.132	352/31	27/13	261/02	55/23	168/59	55/17
AR1343	334617	7931338	0.146	1.041	0.086	003/05	22/11	273/01	52/18	169/84	52/13
AR1345	319225	7946198	0.172	1.05	0.156	319/05	11.0/7	049/02	12.0/8	158/85	11.0/7
AR1348	323849	7950505	0.171	1.07	0.397	349/12	20/7	258/06	27/15	140/77	25/7
AR1349	317502	7953670	0.153	1.08	0.292	274/10	42/29	183/04	52/40	072/79	53/16
AR1352	319337	7957109	0.187	0.04	-0.223	119/14	5.0/4	210/02	18/3	318/75	18/4
AR1353	322337	7955852	0.186	1.09	0.282	293/10	24/11	185/59	21/14	029/29	18/11
AR1354	325308	7953493	0.138	1.08	0.13	095/36	12.0/7	187/03	14/8	281/54	12.0/7
AR1356	307891	7949260	0.161	1.04	0.118	275/01	21/13	005/09	26/13	181/82	25/18
AR1357	305170	7945934	0.16	1.1	0.26	286/18	18/12	190/19	19/13	057/64	15/10
AR1358	303833	7945282	0.126	1.05	0.035	300/01	7.0/5	210/10	16/4	032/80	15/6
AR1360	296653	7950264	0.147	1.07	0.423	074/09	24/12	167/21	21/14	322/67	18/15
AR1361	301245	7950983	0.094	1.05	0.116	122/09	27/8	031/03	27/18	280/81	19/6
AR1362	301134	7952442	0.09	1.08	0.209	102/16	24/7	011/03	25/13	271/74	15/7
AR1366	299336	7957774	0.126	1.03	0.401	187/25	21/6	297/36	38/10	071/43	39/9

AR1367	298581	7960675	0.109	1.06	0.225	099/16	7.0/1	000/27	9.0/3	217/58	8.0/1
AR1368	299117	7961730	0.128	1.04	0.123	149/21	45/14	053/14	50/16	293/64	37/15
Conceição de Muqui Pluton											
CM11	238323	7684301	37.32	1.275	0.094	109/44	12.0/4.3	322/40	10.0/1.9	217/17	11.0/3.8
CM10	234625	7684115	35.95	1.273	0.51	149/57	10.5/8.6	253/8	14.9/9.1	348/30	16.1/3.8
CM12	238508	7683019	1.167	1.134	0.288	139/64	62.1/13.8	16-Dec	62.1/15.5	276/19	19.6/6.7
CM29	237800	7684594	0.525	1.108	-0.118	142/38	15.2/5.9	Apr-43	24.9/10.7	252/22	23.1/6.4
CM14	236249	7680957	41.66	1.081	0.41	65/18	18.1/5.1	157/7	20.8/4.3	267/70	13.2/5.1
CM15	234872	7681433	43.65	1.215	-0.28	122/2	11.2/5.0	31/25	13.9/7.7	216/64	13.4/8.6
CM16	235695	7681022	44.29	1.178	0.704	14-Sep	56.8/4.9	100/2	56.8/3.5	199/75	5.3/3.3
CM17	231787	7681894	49.09	1.355	0.642	67/33	25.1/2.8	331/8	25.1/3.2	228/55	3.4/2.7
CM18	231649	7681698	34.13	1.323	0.528	15/14	18.9/11.9	118/41	19.1/4.7	270/44	12.1/5.3
CM23	234732	7679012	42.94	1.562	0.297	317/57	17.9/5.2	99/26	8.2/3.2	198/17	17.8/2.6
CM24	236492	7680247	58.55	1.152	0.555	257/29	32.9/3.7	348/1	32.9/8.8	80/60	8.9/4.1
CM27	233000	7680506	44.49	1.139	0.452	282/2	37.1/10.7	187/68	36.9/8.8	13/21	12.1/9.6
CM33	235422	7682433	17.62	1.169	0.607	203/18	21.1/7.9	101/30	22.0/9.4	319/53	11.9/7.6
CM34	235107	7682672	54.55	1.186	0.838	220/23	44.1/4.7	115/30	44.1/5.8	341/49	7.1/3.7
CM13	238209	7681858	21	1.054	-0.023	104/39	11.2/9.8	242/42	15.2/10.2	354/22	14.9/10.1
CM22	237289	7681944	49.87	1.06	-0.193	206/22	15.5/3.2	108/20	22.5/7.7	340/59	19.9/3.4
CM25	234485	7680470	31.81	1.243	-0.041	105/50	11.1/3.4	329/30	14.8/3.4	225/22	15.5/3.8
CM26	233666	7680736	68.72	1.339	0.459	55/43	7.2/3.6	325/0	7.9/4.6	235/46	6.2/3.6
CM28	234185	7681756	22.11	1.27	0.654	78/42	19.9/4.1	186/18	19.8/9.1	294/41	9.6/4.8
CM30	238155	7682301	124.1	1.206	-0.035	178/50	9.3/4.6	275/5	16.2/4.3	Sep-38	14.2/4.8
CM31	236500	7681770	6.105	1.1	0.447	168/10	37.8/6.2	76/11	37.9/9.3	300/74	11.0/4.4
CM32	236939	7682455	19.84	1.189	0.715	219/26	11.2/3.1	123/11	14.9/7.4	Nov-61	12.5/3.3
CM35	237367	7679394	44.47	1.414	0.159	47/61	15.5/4.2	253/26	15.2/6.8	158/11	15.1/8.6
CM02	234694	7684193	9.886	1.357	0.703	83/21	18.7/6.8	211/57	18.5/4.0	344/23	8.3/3.4
CM05	233343	7684388	0.141	1.173	0.914	72/31	17.6/2.8	202/47	17.6/3.2	324/26	4.1/1.8

CM08	235672	7678059	40.18	1.695	0.167	96/17	10.6/3.5	334/59	7.5/5.2	194/24	8.4/5.3
CM09	240290	7680034	0.2	1.1	0.589	57/35	16.8/4.9	167/25	15.6/6.8	285/43	10.5/5.8
CM19	237214	7678804	0.379	1.109	0.542	16/74	48.1/8.5	274/3	49.7/14.5	183/14	25.5/9.1
CM20	235520	7678202	37.61	1.843	0.365	64/16	22.6/7.1	316/46	14.6/5.3	168/38	20.0/3.5
CM21	239675	7681122	0.298	1.094	0.215	56/46	44.7/13.6	201/37	48.6/24.1	306/18	50.9/13.2
CM37	233292	7684379	0.242	1.184	0.78	68/40	10.7/3.9	175/19	10.9/3.4	284/43	5.4/2.5
CM38	231211	7683151	0.297	1.185	0.837	137/55	35.2/3.0	31/10	35.1/4.7	294/32	5.1/4.4
Santa Angélica Pluton											
	244958	7709191	98.2	1.355	0.21	67/ 27	8/2.8	158/2	8/3.9	252/63	4.1/2.8
SA40	246575	7708948	28.9	1.102	0.172	31/9	12.1/3.1	293/39	11.6/3.6	132/49	6.4/3.9
SA41	246903	7708934	89.1	1.175	0.49	327/30	15.1/2.8	230/12	15.2/3.1	121/57	5.2/2.0
SA42	245583	7709745	112.5	1.23	0.666	173/3	13.3/2.7	82/6	13.2/2.1	292/83	3.3/2.1
SA43	246858	7711680	61.4	1.266	0.252	17/6	9.4/1.7	107/3	9.7/2.5	221/83	3.6/1.8
SA44	243440	7712099	42.1	1.261	0.426	48/8	7.1/4.6	146/45	6.9/3.3	310/43	5.2/2.8
SA45	243954	7711183	102.7	1.464	0.774	144/16	2.1/5.2	236/5	20.6/3.1	341/73	7.5/2.2
SA49	253660	7713077	82	1.277	0.866	309/44	18.4/7.5	211/8	18/7.1	113/44	10.4/4.2
SA61	247656	7714550	36.9	1.201	0.047	66/55	8.3/7.6	171/10	10.0/5.6	268/33	9.3/6.8
SA26	246017	7710441	52.3	1.419	0.721	50/6	16.6/2.4	319/3	16.5/5.8	204/83	6.0/3.5
SA28	249426	7708184	56.1	1.34	0.399	68/41	19/7	159/1	20/85	250/49	14.5/10.4
SA29	249116	7711498	47.2	1.759	0.111	7.0/40	14.6/2.6	100/3	14.7/1.9	195/50	7.5/2.1
SA31	249263	7710468	68.3	2.049	-0.427	51/85	2.6/2	315/1	7.5/2.6	225/5	7.5/2.1
SA36	246834	7706839	46	1.245	0.384	315/46	9.9/5	222/3	11.3/2.8	130/44	6.7/5.4
SA37	247227	7707948	30.7	1.263	0.102	187/60	4.3/4	334/25	4.3/3.3	71/14	4.4/2.7
SA54	252488	7716289	42.5	1.553	-0.213	94/77	1.9/0.9	299/12	3.7/1.8	208/5	3.7/1.1
SA55	251419	7715998	39.1	1.274	-0.282	91/79	4.1/2.0	248/10	13.4/2.7	339/4	13.1/2.0
SA56	251594	7715430	42.6	1.26	-0.149	111/67	15.4/6.8	205/1	13.9/9.4	295/23	14.4/9.2
SA57	251818	7715567	37.3	1.291	0.044	133/65	9.0/6.4	230/3	11.1/8.0	321/25	10.5/6.7
SA58	250984	7716589	76.6	1.746	-0.243	135/57	7.9/2.6	274/26	9.0/4.0	14/18	9.2/2.6

SA59	248649	7715992	2.2	1.249	-0.008	54/34	5.2/1.8	169/32	3.2/2.1	290/39	5.0/2.4
SA66	247879	7715223	3.1	1.306	-0.711	123/61	13.7/3.4	228/8	42.0/5.8	322/27	42.4/5.2
SA24	243244	7708805	25.8	1.568	-0.701	103/46	6.1/4.1	256/41	18.4/4.1	358/14	18.4/6.0
SA25	244225	7710228	7.1	1.189	0.753	90/47	29.9/5.0	191/11	29.7/6.3	291/41	8.3/4.6
SA27	246017	7710441	21.2	1.581	0.114	170/79	9.7/3.7	32/8	15.2/6.3	300/7	14.4/5.3
SA32	243243	7706058	47.9	1.794	-0.322	113/72	6.8/4.8	273/17	9.4/6.7	4.0/6	9.4/4.9
SA33	243698	7705397	56.3	1.414	-0.158	15/68	8.3/4.1	273/5	9.3/4.3	181/21	10/7.3
SA34	245356	7706080	21	1.17	0.166	51/22	25/3.3	320/3	24.9/3.3	223/68	5.6/2.4
SA47	246834	7706839	66.3	1.581	-0.049	65/39	10.6/6.5	164/11	6.9/5.6	267/49	10.6/5.3
SA50	247227	7707948	52.5	1.041	0.453	20/82	26.0/9.0	200/7	26.0/8.5	110/0	10.7/7.1
SA51	245830	7708609	16.8	1.04	-0.267	241/11	29.8/22.7	142/40	62.8/27.0	343/48	62.8/21.9
SA52	246575	7708948	12.8	1.65	-0.145	196/90	7.2/4.5	322/0	12.9/4.4	52/0	13.6/5.0
SA53	246903	7708934	12.9	1.466	0.302	203/46	14.3/8.4	313/18	16.3/6.4	59/38	14.2/6.6
SA60	247879	7715223	60	1.802	0.104	54/35	7.9/3.0	197/49	7.8/3.0	310/19	9.1/3.0
SA62	247656	7714550	10.4	1.858	0.394	125/69	5.0/4.2	27/3	9.4/4.5	295/21	9.7/2.5
SA64	242108	7712185	11.6	1.636	0.197	123/43	5.5/4.7	22/11	5.5/3.5	281/44	6.4/2.6
SA65	242955	7711723	36.7	1.602	-0.498	159/59	4.6/3.2	395/30	10.1/3.2	257/5	9.5/3.2
SA22	241406	7705180	106.1	1.076	0.756	160/74	40.3/7.0	307/13	40.1/6.5	39/8	9.9/4.2
SA30	244958	7709191	4.6	1.214	-0.289	140/83	6.5/3.8	335/6	8.3/4.8	245/2	7.9/5.1
SA38	243244	7708805	77	1.155	-0.364	43/43	12/4.0	258/41	17/5.0	151/18	14.1/5
SA46	244225	7710228	9.3	1.347	0.169	53/61	3.2/2.3	173/15	3.4/1.5	270/24	2.4/1.6
SA48	246017	7710441	41	1.296	-0.058	82/75	7/5.0	273/15	11.7/6.3	182/3	11.7/4.8
SA67	249426	7708184	16.9	1.716	-0.332	160/77	10.7/2.6	289/8	9.7/5.1	20.0/10	8.3/4.3
SA68	249116	7711498	0.0697	1.17	0,675	64/69	13.6/3.5	165/4.3	4.7/3.0	257/20	5.5/1.4

Table B2 - Anisotropy of magnetic susceptibility parameters of the Caladão granite, Padre Paraíso charnockite, Conceição de Muqui pluton and Santa Angélica pluton. Site number; location (UTM) in meters; Km = mean magnetic susceptibility (10^{-4}SI); P = degree of anisotropy of the magnetic susceptibility ($P=k_1/k_3$);T= AMS ellipsoid shape parameter [$T=2\ln(k_2/k_3) / \ln(k_1/k_3)-1$]; K_1=trend and plunge of magnetic lineation (in

degrees); K_2=trend and plunge of the intermediate anisotropy axis; K_3=trend and plunge of the pole of the magnetic foliation; ε_{12}, ε_{23}, ε_{31} are the semi-angle (measured in degrees) of confidence ellipses of AMS axes from Jelínek's (1978) statistics. AR, CM - this work; [1]AR - Mondou et al. (2012); [2]AR - Cavalcante et al. (2013); MBS - Xavier et al. (2017); TM - Angelo et al. (2019); SA - Temporim et al. (2020).

Appendix C

Supporting Information for chapter IV

Reassessing the Cambrian drift of Gondwana with new paleomagnetic data from post-collisional plutons of the Araçuaí orogen, SE Brazil

Temporim, F. A., Bellon, U. D., Domeier, M., Trindade, R. I. F., D'Agrella-Filho, M.S., Tohver, E.

Contents for Appendix C

Text C1: Thermal diffusion model: numerical model implementation

To simulate the cooling process of the Santa Angélica (SA) and Venda Nova (VN) plutons, two-dimensional heat conservation equation was applied, which takes form as:

$$\left(\frac{dT}{dt}\right) = \kappa\left(\frac{\partial^2 T}{\partial x^2} + \frac{\partial^2 T}{\partial y^2}\right) + H \quad \text{Equation (1)}$$

Assuming the term κ (thermal diffusivity) = (k ρ-1Cp-1), where ρ is the density of the material (kg m-3), Cp is the thermal capacity at a constant pressure (J / Kg / K), k is the thermal conductivity (W/m/K) and H is the volumetric heat production (Wm-3) (Gerya, 2010). The terms accompanied by κ are the second derivative of the temperature of the medium, i.e., the temperature variation in the x and y directions. For most mantle and crustal rocks, radioactive heat only becomes relevant at temperatures above 1200 °C (Clauser, 2009), and as such, we ignored the heat production in Eq. (1). As Eq. (1) is a differential equation, it was solved numerically using a finite-difference method in a python script environment.

The initial grids were build as two-dimensional coordinates dots in a squared matrix equally spaced (dy=dx=100m) on x and y directions (which were coincident with geographic locations of SA and VN). For each position (x,y) in the grid, a temperature was assigned. Here, we assumed a simple geological model for each plutonic unit: the Venda Nova pluton was reduce to the gabbroic-core, a syenomonzonitic envelop and its wall rocks; For the Santa Angélica pluton, the units were reduced to the two gabbroic cores, a granitic envelop and its wall rocks.

Defining the initial temperature (T0) of each unit in both plutons was a segmented task. For the granitic and syenomonzonites units inside the plutons, a saturation of zircon geothermometers (Boehnke et al., 2013; Gervasoni et al., 2016; Shao et al., 2019) were calculated using whole geochemistry data published for the VN and SA plutons (De Campos et al., 2004; Horn & Weber-Diefenbach, 1987; Ludka et al., 1998; Wiedemann et al., 2002; Zanon et al., 2015). The current geothermometer calculations are attached as an excel-file together with the supplementary file of the published paper. Average temperature for the VN syenomonzonites and for the SA granites were 860±50°C and 840±61°C, respectively. These were adopted as initial temperature state for such units (not considering the standard deviation).

The wall rocks were signed with a temperature of 350°C. Vauchez et al. (2019) reported temperatures for the middle crust in the Araçuaí Orogen around 500°C for the age of 510-500Ma. and around 300°C for 480Ma. Geobarometric calculations for Al-contents in

amphibole in the SA granites (Wiedemann et al., 2002) and Al-contents in hornblende in the VN charnockites (Mendes & De Campos, 2012) point out pressures of 5.9-11.4kbar and 5.5 to 6.0kbar, respectively – both related to a middle crust emplacement depth. For such, we considered 350°C a good estimative of temperatures for the wall rocks of both plutons.

Once geothermometer for whole geochemistry in basic rocks is hardly available in literature, and no chemical mineral data of minerals is published for both gabbroic cores of SA and VN – calculation of initial temperatures of mineral geothermometers such as pyroxene on the Ca-MgO-Al2O3-SiO2 system (Herzberg, 1978), $f\Delta O_2$ of spinel composition in mantle rocks and mantle derived melts (Ballhaus et al., 1994), Al and Ti in calcic-amphibole (Ernst, 1998) and REE-in-plagioclase–clinopyroxene thermometer (Sun & Liang, 2017) could not be accomplished. Larsen (1929) had claimed the high variability of direct measures of basaltic magma temperature, going from 720°C to 1260°C in the Kilauea and Vesuvius, which have been more recently measured in the core surface of lavas as above 1050°C in Kilauea (Pinkerton et al., 2002) with peaks in 1230°C (Carling et al., 2015). MOR volcanism has worldly similar volcanic eruption temperatures around 1200°C-1250° (Green et al., 2001), with mantle potential temperature around 1280°C (McKenzie & Bickle, 1988). Studies of basalt melting based on its mineralogical composition have shown that the initial liquidus and melting temperatures in descending order is: andesite, andesitic basalt, tholeiite basalt and alkali basalt (Chen et al., 2017). The temperature of basaltic magma is rarely higher than its first crystallization process (Frost & Frost, 2014). Mineral chemistry and thermodynamic studies in pyroxene of olivine-gabbros and norites in the Swedish Caledonides where reported to a range of temperatures from 1240°C-1180°C and 1180°C-1050°C, respectively (Otten & Senior, 1985). Meanwhile, mineral chemistry of olivine-gabbros and hornblend-bearing-gabbros from the Sanandaj–Sirjan belt in W-Iran was reported as 1300°C and 950°C, respectively (Sepahi et al., 2013).

Due the variability and range of reports for basic magmas, we have choose the initial temperature of the gabbros of Venda Nova and Santa Angélica as an intermediate temperature, which was 1100°C.

Thermal conductivity in rocks can vary up to 50% and, as considered by Jaupart & Mareschal (2007), thermal diffusivity is about 1x10-6m²s-1 for intermediary crust. Whittington et al. (2009) have shown that (κ) decreases from 1.5x10-6 – 2.5x10-6m2s-1, in environment

conditions, down to 0.5x10-6m2s-1 in the middle crust. Therefore, in the Venda Nova and Santa Angélica plutons, we decided to apply (κ = 0.5x10-6m2s-1) for thermal modelling.

Ensuring numerical stability, the step in time for each calculation for the dots (dt) was equal to 100 years. For the VN, a direct approach was established, directly simulating the initial matrix of (T0) going through diffusion for 3 million years (from the initial state, i.e, its emplacement). As proposed by Temporim et al. (2020), the SA pluton consists of two plutonic features, a SW and a NE lobe, separated by an internal magmatic shear zone. Therefore, two different scenarios were proposed for SA: a) these two plutons intrude at the same time with the same T0 and undergo heat diffusion for 3 Ma; b) the shallowest pluton (the NE lobe) intrudes first, cools down and then the SW pluton intrudes the nearby wall rocks. In scenario (b), the cooling process of the earlier NE pluton and its host was alternatively simulated for 100 kyr and 1 Ma prior to intrusion of the SW pluton, to investigate the differences associated with an approximately coeval intrusion versus a late emplacement. After the intrusion of the SW body, heat diffusion was simulated for an additional 3 Ma.

References of the appendices

Angelo, T.V., Egydio-Silva, M., Temporim, F.A., Seraine, M. (2020). Midcrust deformation regime variations across the Neoproterozoic Araçuaí hot orogen (SE Brazil): Insights from structural and magnetic fabric analyses. Journal of Structural Geology, v. 134, 104007, https://doi.org/10.1016/j.jsg.2020.104007.

Ballhaus, C., Berry, R. F., & Green, D. H. (1994). High-pressure experimental calibration of the olivine-orthopyroxene-spinel oxygen geobarometer: implications for the oxidation state of the upper mantle. Contributions to Mineralogy and Petrology, 118(1), 109. https://doi.org/10.1007/BF00310615

Boehnke, P., Watson, E. B., Trail, D., Harrison, T. M., & Schmitt, A. K. (2013). Zircon saturation re-revisited. Chemical Geology, 351, 324–334. https://doi.org/10.1016/j.chemgeo.2013.05.028

Carling, G. T., Radebaugh, J., Saito, T., Lorenz, R., Dangerfield, A., Tingey, D. G., Keith, J. D., South, J. V., Lopes, R. M., & Diniega, S. (2015). Temperatures, thermal structure, and behavior of eruptions at Kilauea and Erta Ale volcanoes using a consumer digital camcorder. Geo Res J, 5, 47–56. https://doi.org/10.1016/j.grj.2015.01.001

Cavalcante, G. C. G., Egydio-Silva, M., Vauchez, A., Camps, P. (2013). Strain distribution across a partially molten middle crust: Insights from the AMS mapping of the Carlos Chagas Anatexite, Araçuaí belt (East Brazil). Journal of Structural Geology, v. 55, p. 79-100, https://doi.org/10.1016/j.jsg.2013.08.001.

Chen, X., Zhang, Y., Hui, D., Chen, M., & Wu, Z. (2017). Study of melting properties of basalt based on their mineral components. Composites Part B: Engineering, 116, 53–60. https://doi.org/10.1016/j.compositesb.2017.02.014

Clauser, C. (2009). Heat transport processes in the earth's crust. Surveys in Geophysics, 30(3), 163–191. https://doi.org/10.1007/s10712-009-9058-2

Day R., Fuller, M., Schmidt, V. A. (1977). Hysteresis properties of titanomagnetites: grain-size and compositional dependence. Phys. Earth Planet Interiors, 13(4), 260-267. https://doi.org/10.1016/0031-9201(77)90108-X.

De Campos, C. P., Mendes, J. C., Ludka, I. P., de Medeiros, S. R., de Moura, J. C., & Wallfass, C. (2004). A review of the Brasiliano magmatism in southern Espírito Santo, Brazil, with emphasis on post-collisional magmatism. Journal of the Virtual Explorer, 17, 1–44. https://doi.org/10.3809/jvirtex.2004.00106

rnst, W. G. (1998). Experimental phase-equilibrium study of Al- and Ti-contents of calcic amphibole in MORB-A semiquantitative thermobarometer. American Mineralogist, 83(9–10), 952–969. https://doi.org/10.2138/am-1998-9-1004

Frost, B. R., & Frost, C. D. (2014). Essentials of Igneous and Metamorphic Petrology. In Essentials of Igneous and Metamorphic Petrology (1st ed.). Cambridge University Press. https://doi.org/10.1017/9781108685047

Gervasoni, F., Klemme, S., Rocha-Júnior, E. R. V., & Berndt, J. (2016). Zircon saturation in silicate melts: a new and improved model for aluminous and alkaline melts. Contributions to Mineralogy and Petrology, 171(3), 1–12. https://doi.org/10.1007/s00410-016-1227-y

Gerya, T. (2010). Numerical Geodynamic Modelling (Issue 1). https://doi.org/10.16309/j.cnki.issn.1007-1776.2003.03.004

Gouvêa, L.P., Medeiros, S.R., Mendes, J.C., Soares, C., Marques, R., Melo, M. (2020). Magmatic activity period and estimation of P-T metamorphic conditions of pre-collisional opx-metatonalite from Araçuaí-Ribeira orogens boundary, SE Brazil. Journal of South American Earth Sciences, v. 99, 102506, https://doi.org/10.1016/j.jsames.2020.102506.

Green, D. H., Falloon, T. J., Eggins, S. M., & Yaxley, G. M. (2001). Primary magmas and mantle temperatures. European Journal of Mineralogy, 13(3), 437–451. https://doi.org/10.1127/0935-1221/2001/0013-0437

Herzberg, C. T. (1978). Pyroxene geothermometry and geobarometry: experimental and thermodynamic evaluation of some subsolidus phase relations involving pyroxenes in the system CaO-MgO-Al2O3-SiO2. Geochimica et Cosmochimica Acta, 42(7), 945–957. https://doi.org/10.1016/0016-7037(78)90284-3

Horn, H. A., & Weber-Diefenbach, W. (1987). Geochemical and genetic studies of three invers zoned intrusive bodies of both alkaline and calc-alkaline composition in the Ribeira Mobile Belt (Espírito Santo, Brazil). Revista Brasileira de Geociências, 17(4), 488–497. http://www.ppegeo.igc.usp.br/index.php/rbg/article/view/11961

Hrouda R.and Hruskova, I. (1990). On the detection of weak strain parallel to the bending by magnetic anisotropy: a mathematical study. Stud. Geoph. Geod, 34, 327-341.

Jaupart, C.; Mareschal, J.C. (2007). Heat Flow and Thermal Structure of the Lithosphere. In: Watts, A. B. Chapter 6: Crust and Lithosphere Dynamics. In: Schubert, G. Treatise on Geophysics. Elsevier, 1ed, 6054 pp.

Jelínek, V. (1978). Statistical processing of anisotropy of magnetic susceptibility measured on groups of specimen. Studia Geophysica et Geodaetica, 22, 50–62. 10.1007/BF01613632.

Larsen, E. (1924). The temperatures of magma. The Mineralogical Society of America, v. 14, p. 81-94.

Ludka, I. P., Wiedemann, C. M., & Töpfner, C. (1998). On the origin of incompatible element enrichment in the Venda Nova pluton, State of Espirito Santo, southeast Brazil. Journal of South American Earth Sciences, 11(5), 473–486. https://doi.org/10.1016/S0895-9811(98)00028-5

McKenzie, D., & Bickle, M. J. (1988). The volume and composition of melt generated by extension of the lithosphere. Journal of Petrology, 29(3), 625–679. https://doi.org/10.1093/petrology/29.3.625

Mendes, J. C., & De Campos, C. M. P. (2012). Norite and charnockites from the Venda Nova Pluton, SE Brazil: Intensive parameters and some petrogenetic constraints. Geoscience Frontiers, 3, 789–800. https://doi.org/http://dx.doi.org/10.1016/j.gsf.2012.05.009

Mondou, M., Egydio-Silva, M., Vauchez, A., Raposo, M. I. B., Bruguier, O., Oliveira, A. F. (2012). Complex, 3D strain patterns in a synkinematic tonalite batholith from the Araçuaí Neoproterozoic orogen (Eastern Brazil): evidence from combined magnetic and isotopic chronology studies. Journal of Structural Geology, v. 39, p. 158-179. https://doi.org/10.1016/j.jsg.2012.02.015.

Otten, M. T., & Senior, A. (1985). Mineral chemistry and crystallization conditions of the Artfjället gabbro and dolerites (Central Swedish Caledonides). Lithos, 18(C), 295–310. https://doi.org/10.1016/0024-4937(85)90033-7

Pedrosa-Soares, A.C., Campos, C., Noce, C., Silva, L.C., Novo, T., Roncato, J., Medeiros, S., Castañeda, C., Queiroga, G., Dantas, E., Dussin, I., Alkmim, F. (2011). Late Neoproterozoic-Cambrian granitic magmatism in the Araçuaí orogen (Brazil), the Eastern Brazilian Pegmatite Province and related mineral resources. In: A.N. Sial, J.S. Bettencourt, C.P. De Campos, V.P. Ferreira (Eds.), Granite-Related Ore Deposits, Geological Society, Special Publications, London, pp. 25-51.

Pedrosa-Soares, A.C., Deluca, C., Araujo, C.S., Gradim C., Lana, C., Dussin, I., Silva, L.C., Babinski, M. (2020). O Orógeno Araçuaí à luz da geocronologia: um tributo a Umberto Cordani. In: Geocronologia e evolução tectônica do Continente Sul-Americano: a contribuição de Umberto Giuseppe Cordani. São Paulo: Solaris Edições Culturais, p. 250-272.

Pinkerton, H., James, M., & Jones, A. (2002). Surface temperature measurements of active lava flows on Kilauea volcano, Hawai'i. Journal of Volcanology and Geothermal Research, 113(1–2), 159–176. https://doi.org/10.1016/S0377-0273(01)00257-8

Sepahi, A. A., Borzoei, K., & Salami, S. (2013). Mineral chemistry and thermobarometry of plutonic, metamorphic and anatectic rocks from the Tueyserkan area (Hamedan, Iran). Geological Quarterly, 57(3), 515–526. https://doi.org/10.7306/gq.1108

Serrano, P., Pedrosa-Soares, A., Medeiros-Junior, E., Fonte.Boa, T., Araujo, C., Dussin, I., Queiroga, G., Lana, G. (2018). A-type Medina batholith and post-collisional anatexis in the Araçuaí orogen (SE Brazil). Lithos, v. 320, p. 515-536. https://doi.org/10.1016/j.lithos.2018.09.009.

Shao, T., Xia, Y., Ding, X., Cai, Y., & Song, M. (2019). Zircon saturation in terrestrial basaltic melts and its geological implications. Solid Earth Sciences, 4(1), 27–42. https://doi.org/10.1016/j.sesci.2018.08.001

Soares, C., Queiroga, G., Pedrosa-Soares, A., Gouvêa, L., Valeriano, C., Melo, M.G., Marques, R., Delicio, R. (2020). The Ediacaran Rio Doce magmatic arc in the Araçuaí – Ribeira boundary sector, southeast Brazil: Lithochemistry and isotopic (Sm–Nd and Sr) signatures. Journal of South American Earth Sciences 104 102880. DOI: 10.1016/j.jsames.2020.102880

Sun, C., and Liang, Y. (2017). A REE-in-plagioclase–clinopyroxene thermometer for crustal rocks. Contributions to Mineralogy and Petrology, 172(24), 20. https://doi.org/10.1007/s00410-016-1326-9

Temporim, F.A., Trindade, R.I.F., Tohver, E., Soares, C.C., Gouvêa, L.P., Egydio-Silva, M., Amaral, C.A.D., Souza Jr., G.F. (2020). Magnetic fabric and geochronology of a Cambrian "isotropic" pluton in the Neoproterozoic Araçuaí orogeny. Tectonics, v. 39(5), e2019TC005877. https://doi.org/10.1029/2019TC005877.

Temporim, F.; Trindade, R.; Tohver, E.; Soares, C.; Gouvêa, L. P.; Egydio-Silva, M.s; Amaral, C.; Souza Jr., G. (2020), "AMS data of the Santa Angélica pluton", Mendeley Data, V2, doi: 10.17632/3xth2s5cp9.2

Vauchez, A., Hollanda, M. H. B. M., Monié, P., Mondou, M., and Egydio-Silva, M. (2019). Slow cooling and crystallization of the roots of the Neoproterozoic Araçuaí hot orogen (SE Brazil): Implications for rheology, strain distribution, and deformation analysis. Tectonophysics, 766, 500–518. https://doi.org/10.1016/j.tecto.2019.05.013

Whittington, A. G., Hofmeister, A. M., & Nabelek, P. I. (2009). Temperature-dependent thermal diffusivity of the Earth's crust and implications for magmatism. Nature, 458(7236), 319–321. https://doi.org/10.1038/nature07818

Wiedemann, C. M., De Medeiros, S. R., Ludka, I. P., Mendes, J. C., & Costa-de-Moura, J. (2002). Architecture of Late Orogenic Plutons in the Araçuaí-Ribeira Fold Belt, Southeast Brazil. Gondwana Research, 5(2), 381–399. https://doi.org/10.1016/S1342-937X(05)70730-9

Wisniowscky, L., Pedrosa-Soares, A., Medeiros-Junior, E., Belém, J., Dussin, I., Queiroga, G. (2021). Ultra-high temperature, mid-crustal level, contact metamorphism imprinted on granulite facies paragneisses by a norite intrusion (São Gabriel da Baunilha, Araçuaí orogen, southeast Brazil). J. Metamorph. Geol. DOI: 10.1111/jmg.12594

Xavier, B.C. (2017). Relações tectônicas no Central da Faixa Araçuaí: análise estrutural por AMS e geocronologia U/Pb e Lu/Rf [Msc Thesis]: São Paulo, Universidade de São Paulo 123p.

Zanon, M. L., Chaves, A. D., Rangel, C. V. G. T., Gaburo, L., & Pires, C. R. (2015). Os aspectos geológicos do maciço santa angélica (ES): Uma nova abordagem. Brazilian Journal of Geology, 45(4), 609–633. https://doi.org/10.1590/2317-4889201520150005